QCD UNDER EXTREME CONDITIONS: INHOMOGENEOUS CONDENSATION

Achim Heinz

Dissertation zur Erlangung des
Doktorgrades der Naturwissenschaften

vorgelegt beim Fachbereich Physik
der Goethe-Universität
in Frankfurt am Main

Frankfurt am Main, September 2014
(D 30)

vom Fachbereich Physik der Goethe-Universit
als Dissertation angenommen

Dekan: Prof. Dr. Joachim Stroth
1. Gutachter: Prof. Dr. Dirk-Hermann Rischke
2. Gutachter: PD. Dr. Francesco Giacosa

Datum der Disputation: Oktober 2014

Abstract

Almost 40 years after the first publication on the phase diagram of quantum chromodynamics (QCD) big progress has been made but many questions are still open. This work covers several aspects of low-energy QCD and introduces advanced methods to calculate selected parts of the QCD phase diagram.

Spontaneous chiral symmetry breaking as well as its restoration is a major aspect of QCD. Two effective models, the Nambu–Jona-Lasinio (NJL) model and the linear σ-model, are widely used to describe the QCD chiral phase transition. We study the large-N_c behavior of the critical temperature T_c for chiral symmetry restoration in the framework of both models. While in the NJL model T_c is independent of N_c (and in agreement with the expected QCD scaling), the scaling behavior in the linear σ-model reads $T_c \propto N_c^{1/2}$. However, this mismatch can be corrected: phenomenologically motivated temperature-dependent parameters or the extension with the Polyakov-loop renders the scaling in the linear σ-model compatible with the QCD scaling.

The requirement that the chiral condensate which is the order parameter of the chiral symmetry is constant in space is too restrictive. Recent studies on inhomogeneous chiral condensation in cold, dense quark matter suggest a rich crystalline structure. These studies feature models with quark degrees of freedom. In this thesis we investigate the formation of the chiral density wave (CDW) in the framework of the so-called extended linear sigma model (eLSM) at high densities and zero temperature. The eLSM is a modern development of the linear σ-model which contains scalar, pseudoscalar, vector, as well as axial-vector mesons, and in addition, a light tetraquark state. The nucleon and its chiral partner are introduced as parity doublets in the mirror assignment. The model describes successfully the vacuum phenomenology and nuclear matter ground-state properties. As a result we find that an inhomogeneous phase in the form of a CDW dominates the high density regime. The formation of a homogeneous nuclear matter ground state depends on the parameters determined in the vacuum. However, even in the case of a homogeneous nuclear matter ground state the onset of the CDW is not higher

than $5.04\rho_0$, a density at which the eLSM is still applicable.

Motivated by the rich structure that inhomogeneous condensation produces, and in order to study inhomogeneous condensation in a general framework we describe the finite-mode approach. Former limitations of the finite mode approach to $1+1$ dimensions and only one condensate are successively overcome. Different error sources are analyzed and strategies to minimize them are outlined. First, the well-known analytic results for 1+1 dimensional models are reproduced in this purely numerical approach. Second, the finite-mode approach shows to be capable to describe up to four inhomogeneous condensates. Finally, the method is applied to the $3+1$ dimensional NJL model. The famous inhomogeneous "island" as well as the inhomogeneous "continent" are reproduced. The continent persists for different constituent quark masses and different numbers of regulators. However, in contrast to previous findings the continent becomes thinner for increasing chemical potential.

Contents

Chapter 1

Introduction

1.1 The QCD Lagrangian and the QCD phase diagram

Among the four forces in nature, the strong interaction is responsible for most of the visible mass in the Universe. The proton and neutron, which are the basis for almost all matter surrounding us, have a mass of ~ 1 GeV that arises almost entirely from nonperturbative QCD effects.

The QCD Lagrangian is locally $SU(N_c)$ gauge invariant, and for N_f quarks and $N_c^2 - 1$ gluons it reads:

$$\mathscr{L}_{\mathrm{QCD}} = \sum_{i=1}^{N_f} \bar{q}_{a,i} \left(\imath \not{D} - m_i \right) q_{a,i} - \frac{1}{4} G^a_{\mu\nu} G^{a,\mu\nu} \ , \tag{1.1}$$

with the flavor index i, the covariant derivative $\not{D}$ and the field strength tensor $G^a_{\mu\nu}$:

$$\begin{aligned} \not{D} =& \gamma^\mu \left(\partial_\mu - \imath g_{QCD} A^a_\mu t^a \right) \ , \\ G^a_{\mu\nu} =& \partial_\mu A^a_\nu - \partial_\nu A^a_\mu + g_{QCD} f^{abc} A^b_\mu A^c_\nu \ , \quad a, b, c = 1, \ldots, N_c^2 - 1 \ . \end{aligned} \tag{1.2}$$

The gluon fields are denoted as A^a_μ and the quark fields as $q_{a,i}$. The fields are coupled via the QCD coupling constant g_{QCD}. For the physical case $N_c = 3$ the matrices t_a are $t^a = \lambda^a/2$, with λ^a being the Gell-Mann matrices. A remarkable feature is the self coupling of gluon degrees of freedom, which follows from the non-Abelian group structure. The constants f^{abc} are the structure constants of the group $SU(3)$. The charge of $SU(N_c)$ is referred to as color. The gluons carry adjoint, the quarks fundamental color charge.

The fundamental degrees of freedom of QCD are quarks and gluons. However, in the vacuum they are confined and the relevant degrees of freedom

are hadrons. Indeed, it is believed that at high temperature and/or density a phase transition to a deconfined gas of quarks and gluons is realized: the quark-gluon plasma. First pioneering works suggested this rather simple picture of the QCD phase diagram at nonzero temperature T and density μ [1]. In Fig. 1.1 such a phase diagram is displayed, where only two phases are present: the confined (I) and the deconfined (II) phase.

Almost 40 years later the understanding of the phase diagram has improved a lot, but many questions are still unsettled. Certainly the developments of lattice QCD gave an important contribution at zero density and nonzero temperature [2, 3], but at nonzero density one has still to rely on effective models [4]. In Fig. 1.2 we show a modern version of the QCD phase

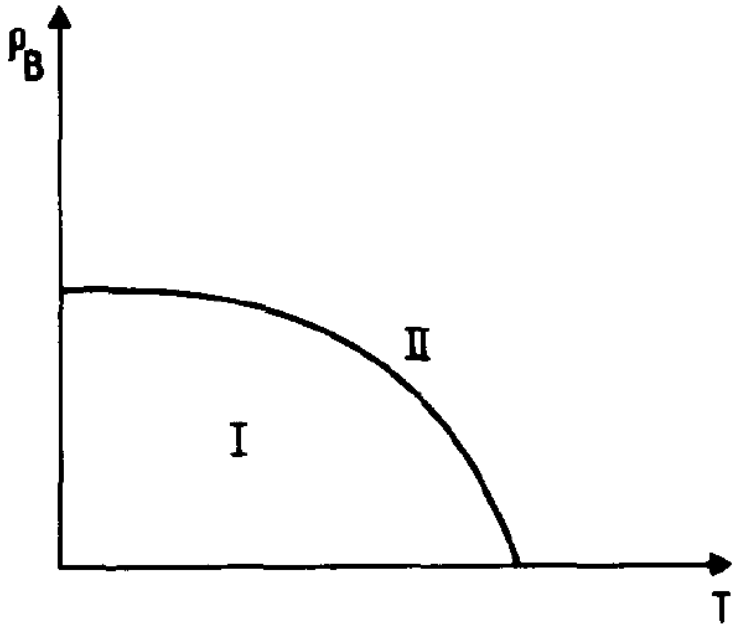

Figure 1.1: Phase diagram of QCD after Parisi and Cabibbo in 1975. For small temperature and density matter is confined (I), for high temperature and density deconfined (II) [1].

diagram. There are many different phases (especially along the μ axis) which are currently under investigation [5]. The main point here is not the description of the phases which have been proposed (for a detailed review see Ref. [6]), but to show the impressive theoretical development since 1975. The QCD phase diagram is still a very active topic of research.

Besides the invariance under $SU(N_c)$ symmetry transformations, the QCD Lagrangian contains several approximate symmetries. In the low-energy

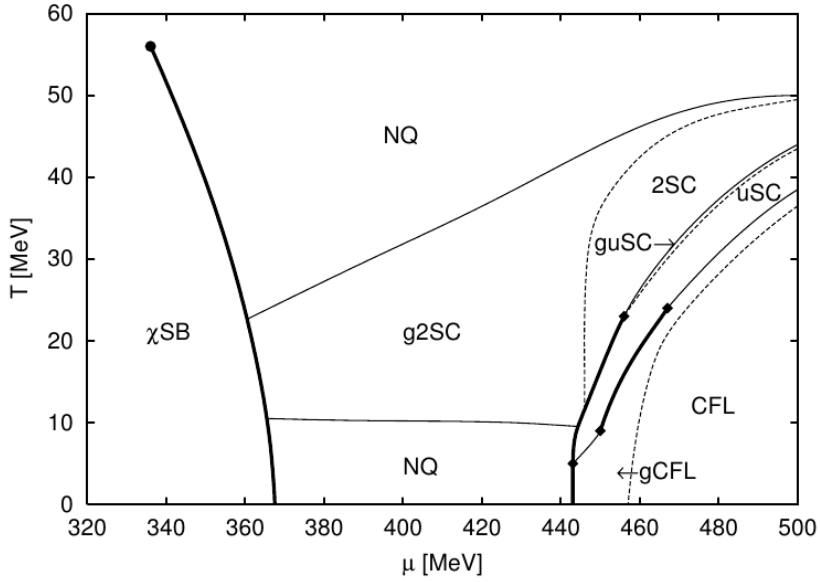

Figure 1.2: Modern view of the phase diagram of QCD from Ref. [5]. The high-chemical potential regime is covered with a rich structure of different phases.

regime of QCD, the most important one is the chiral symmetry. The spontaneous breaking of chiral symmetry in the vacuum is responsible for non-degenerate masses of so-called chiral partners [7, 8, 9] (hadrons with the same quantum numbers except for parity and G-parity). The order parameter of chiral symmetry breaking is the chiral condensate, denoted as $\langle \bar{q}q \rangle \sim \langle \sigma \rangle$.

Due to the complicated structure of the QCD Lagrangian different limits of QCD are studied. Two important limits are the so-called chiral limit and the pure gauge theory:

- **Chiral limit and chiral symmetry:** The chiral limit of QCD is obtained for $m_q \to 0$ (bare masses). In this limit, chiral symmetry is an exact symmetry of QCD. The QCD Lagrangian is then invariant under global chiral $SU(N_f)_L \times SU(N_f)_R$ transformations. An emerging quark condensate serves as an exact order parameter for chiral symmetry breaking. The mass spectrum of the light mesons and baryons shows that the assumption of the chiral limit is justified [10]: the masses of hadrons are much larger than the light bare quark masses. Their contribution give only small corrections to the hadron masses. Turning back to nonzero temperature and densities it is expected that at high enough temperature the so-called chiral phase transition takes place: a transition from the phase with spontaneously broken symmetry in

the vacuum to a restored phase at nonzero temperature and/ or density [11]. For zero density this behavior could be settled with lattice simulations [2, 3]. There, in the chiral limit the phase transition is of second order for $N_f = 2$ and of first order for $N_f > 2$. For nonzero quark masses it turns out to be a crossover phase transition, although the chiral condensate is not an exact order parameter anymore.

- **Pure gauge theory:** A stunning feature of QCD is confinement. Even if quarks and gluons carry color charge, no colored degree of freedom has been measured: only composite, color-neutral objects are observed. An approximate order parameter for confinement is the Polyakov loop [12]. It is an exact order parameter in the limit of infinitely heavy quarks ($m_q \to \infty$ and therefore opposite to the chiral limit). After sending all bare quark masses to infinity, they do not contribute anymore to the dynamics. In pure gauge theory only the gluon degrees of freedom are active. It follows that the Polyakov loop is an exact order parameter of the deconfinement transition [13]:

$$l(x) = N_c^{-1}\mathrm{Tr}\left[\mathcal{P}\exp\left(\imath g_{QCD}\int_0^{1/T} A_0(\tau,x)d\tau\right)\right] \ , \qquad (1.3)$$

  where the trace runs over all color degrees of freedom, $\mathcal{P}$ stands for path ordering, and $A_0(\tau, x)$ is the zeroth component of the gluon field A_μ. The expectation value of the Polyakov loop vanishes for confined matter at low temperature and density. However, it is expected that at sufficiently high temperature and/or density a phase transition to a deconfined gas of interacting quarks and gluons takes place [1, 4]. The Polyakov loop reproduces this deconfinement phase transition and the absolute value approaches unity in the deconfined phase at asymptotically high temperatures. The pure gauge theory is an important limit of QCD which can also be motivated using large-N_c arguments, explained in detail afterwards. The order of the deconfinement phase transition in pure gauge theory is of first order and can change to a crossover transition with nonzero quark masses [14].

In the previous paragraphs two different phase transitions where described, the chiral transition and the deconfinement transition. Both follow from limits of the QCD Lagrangian. The chiral limit requires massless quarks which is nearly given in the vacuum where low-energy hadrons are the relevant degrees of freedom. On the other hand, pure gauge theory is justified by considering only heavy quarks or by studying the large-N_c limit.

However, in QCD none of these limits is realized. Neither the chiral condensate nor the Polyakov loop are exact order parameters of the chiral and the deconfinement transition of QCD. Since none of these order parameters are exact order parameters in real nature the precise connection between the deconfinement and the chiral phase transition is in general not yet clear. Indeed, in the last decade lattice calculations were able to show that at zero density and nonzero temperature both, the chiral condensate and the Polyakov loop, are inter. These calculations which follow from first principles of QCD showed that both transitions take place simultaneously [2, 3, 15]. This behavior has been confirmed in effective models [16, 17]. The transition is realized as a crossover transition: close to a critical temperature T_c, both vacuum expectation values slowly change from a large to a small value and vice versa. However, at nonzero density lattice simulations suffer from technical problems, e.g. lattice methods cannot handle the complex fermion determinant at nonzero densities (sign problem) [18], different lattice realizations do not agree on basic features of the QCD phase diagram, like the critical point [19].

The QCD Lagrangian does not allow for straightforward calculations at all energy scales. Different aspects of QCD require different effective models. Besides the already mentioned lattice simulations which work for zero density, effective models based on different QCD degrees of freedom are used.

- The NJL model [20, 21, 22, 23, 24, 25] which originally dates back to a pre-QCD era, considers in its basic version only quarks. The quarks propagate freely at any temperature and the basic feature of confinement is missed. Therefore, a proper description of the deconfinement phase transition is not possible.

- The linear σ-model [8, 26, 27, 28, 29, 30], considers only hadronic degrees of freedom and thus is confined for all temperatures. On this account it fails to describe the deconfinement phase transition as well.

Both models are used to describe the chiral phase transition at nonzero temperature. However, for reasons outlined above both miss to describe the deconfinement phase transition. Nevertheless, the chiral phase transition in both models agrees with lattice studies. Along the density axis, where lattice-QCD calculations are not yet available, these models, in agreement with other phenomenological models [31, 32, 33, 34, 35], indicate that chiral symmetry restoration occurs through a first-order phase transition. The challenge is now to identify quantities that allow to judge the reliability of the two models.

Other important effective models have been developed in 1+1 dimensions. The Gross-Neveu (GN) model [36, 37, 38, 39] is a quark-based model that only considers one flavor (as a consequence chiral symmetry is realized in a discrete way). However, in the large-N_c limit it shares QCD-like features such as asymptotic freedom and dynamical chiral symmetry breaking. An extension of the GN model is the chiral Gross-Neveu (χGN) model [40, 41] which has a continuous chiral symmetry. Including a second flavor we turn to the NJL_2 model [42]. All these $1+1$ dimensional models play an important role in analyzing the QCD phase diagram. In fact, it can be shown that for moderate densities and low temperatures QCD effectively reduces from $3+1$ to $1+1$ dimensions [43, 44, 45].

1.2 The large-N_c limit and chiral symmetry restoration

The large N_c-limit is a well-defined approximation scheme of QCD [46, 47, 48]. It was developed because of the lack of reliable approximations of the low-energy regime of QCD. To study large-N_c scaling of QCD properties allows to judge the applicability of effective models. After identifying the large-N_c scaling of the QCD Lagrangian, it is straightforward to also implement a large-N_c scaling in effective models as well.

The large-N_c limit of QCD implies that we enlarge the color symmetry group from $SU(3)$ to $SU(N_c)$. With the requirement that enlarging the number of colors does not lead to a trivial theory, the large-N_c limit simplifies QCD. Still, mesons and baryons are present for $N_c \gg 3$ but QCD in the large-N_c limit is –although not solvable– substantially simpler [49]. Properties of QCD can now be expressed as a series in N_c^{-n}. This allows to separate QCD contributions which are large-N_c dominant from those which are large-N_c suppressed. For instance one can show that the large-N_c limit allows to understand the phenomenologically well-established Zweig rule [50].

The actual implementation of the large-N_c limit to the QCD Lagrangian can be motivated by looking at different aspects of QCD [47]. The starting point of the large-N_c analysis is the requirement that it has to be consistent with QCD and as a consequence the QCD coupling g_{QCD} scales with N_c as:

$$N_c \to \infty \ , \quad g_{QCD}^2 \ N_c \to \text{finite} \ . \tag{1.4}$$

As a result the masses of quark-antiquark constituents scale with N_c^0 and the masses of baryons with N_c. The large-N_c scaling also affects the interaction vertices. Multiple meson interactions are suppressed in the large-N_c

limit: a k-leg meson interaction vertex scales as $N_c^{-(k-2)/2}$. Taking the limit $N_c \to \infty$ the interaction among mesons goes to zero: decays and scattering processes are suppressed. At nonzero temperature and in the large-N_c limit mesons form a gas of free noninteracting stable particles (this is true for any temperature in the confined phase).

The scaling behavior can be easily included in the aforementioned effective models. For the NJL model, where the gluon interaction is replaced by an effective four-quark interaction the coupling constant scales with $1/N_c$. Also for the linear-σ model which only contains mesons the implementation is straightforward: the four-meson vertices adopt a scaling proportional to $1/N_c$. These simple modifications allow both models to follow the large-N_c scaling of QCD. It is then possible to test the applicability of both models for specific features of QCD.

The deconfinement phase transition and the chiral phase transition are important features of QCD at nonzero temperature. It is expected that the critical temperatures for both of them are independent of the number of colors, see Refs. [43, 51, 52, 53] and refs. therein. The relevant scale for the transition temperature should be the only existing QCD scale, $\Lambda_{QCD} \propto N_c^0$. The two effective models introduced above differ in the mechanism how chiral symmetry restoration is realized. Our investigation shows that the scaling of the critical temperature disagrees for the two models. In the NJL model which is based on quark interactions the chiral phase transition does not vanish in the large-N_c limit, and it is thus in agreement with the QCD scaling. However, in the linear σ-model where meson-interactions are responsible for the chiral symmetry restoration the critical temperature scales as $\sqrt{N_c}$ and as a consequence the transition does not take place for $N_c \to \infty$. Since the argument is based on general aspects of the two considered models, the result is also true for more complicated and realistic generalizations of the models, e.g. adding flavors and vector degrees of freedom to the models will not influence their scaling properties.

The problematic feature of σ-models at nonzero temperature in the large-N_c limit can be overcome. Namely, it is possible to modify the model in order to reproduce a consistent behavior. In a purely phenomenologically based modification, an explicit temperature dependence of at least one of the coupling constants is added. This extension ensures the correct scaling of the critical temperature. The correct scaling can also be achieved by introducing the Polyakov loop degree of freedom to the linear-σ model. The deconfinement phase transition modelled by the Polyakov-loop then triggers the chiral phase transition for the mesons and therefore ensures the correct scaling of the critical temperature. As a result chiral hadronic models are

consistent with the large-N_c limit, although the effect of the underlying color degrees of freedom has to be taken into account in an effective way.

1.3 Inhomogeneous phases at nonzero density

The physics of spontaneous symmetry breaking in QCD is enriched by the possibility of inhomogeneous condensation. In studies of effective theories of QCD at nonzero temperature and density the chiral condensate which is the order parameter of the spontaneous symmetry breaking is taken as a constant over space. However, there is the possibility that the effective potential is minimized by an order parameter which varies as a function of spatial coordinates.

Already in the pioneering works of Refs. [54, 55, 56, 57, 58, 59, 60, 61, 62, 63, 64, 65] the so-called chiral density wave (CDW) where not only the chiral condensate $\langle\sigma\rangle \neq 0$ but also the expectation value of the neutral pion field is a function of spatial coordinates ($\langle\pi^3\rangle \neq 0$), was used to minimize the effective potential. It has been suggested that such effects could be relevant for QCD. However, the aforementioned approaches needed to include nucleon-nucleon tensor forces. Without these additional forces the nuclear matter ground state was, in contradiction to experimental findings, no longer homogeneous.

In the last years new developments emphasized the relevance of inhomogeneous condensation. It was possible to find an analytic expression for the inhomogeneous phases of the $1+1$ dimensional GN model and extensions of it [38, 39, 66, 67, 68]. A detailed study of the phase diagram revealed that a spatially varying order parameter indeed minimizes the effective potential at high density. Furthermore, it was argued that in the large-N_c limit of QCD at high density an inhomogeneous phase, in the form of a chiral density wave, is realized. The state of matter realized in this regime was named "quarkyonic matter" [45, 69]. Inhomogeneous phases were also investigated in Refs. [70, 71, 72, 73, 74, 75, 76, 77, 78] in the framework of the NJL model as well as in the quark-meson model and the skyrmion model.

The question on the relevance of inhomogeneous condensation in nuclear matter is not yet fully settled. In this thesis we re-investigate the question whether inhomogeneous condensation at nonzero density occurs in a model based only on hadronic degrees of freedom.

- The hadronic model that we use to calculate inhomogeneous condensation in nuclear matter is based on symmetries of QCD and includes scalar, pseudoscalar, vector, and axial-vector mesons, as well as nucleons and their chiral partners. The underlying symmetries are chiral

symmetry and dilatation invariance. The resulting model, developed in Refs. [29, 79, 80] and denoted as the eLSM, successfully describes the hadron vacuum phenomenology, both in the meson [30, 81] and baryon [82] sectors. The nucleon and its chiral partner are treated in the mirror assignment [83, 84, 85], in which a chirally invariant mass term exists (see also Refs. [82, 86, 87, 88, 89, 90, 91] and refs. therein).

In the eLSM the σ field is not assigned to the lightest scalar resonance $f_0(500)$ (as proposed in older versions of the σ-model), but to the heavier state $f_0(1370)$. This is in agreement with a variety of studies of low-energy QCD, e.g. Refs. [92, 93, 94, 95, 96, 97, 98] and refs. therein. The description of the $f_0(500)$ state is not conclusive up to now. In the literature it is interpreted as a resonance in the pion-pion scattering continuum [99, 100, 101, 102, 103, 104, 105, 106] or as a tetraquark state [105, 106, 107, 108, 109, 110, 111, 112, 113]. It follows that both resonances $f_0(500)$ and $f_0(1370)$ are relevant for studies at nonzero density [80]. In the framework of the eLSM, the resonance $f_0(500)$ was coupled in a chirally invariant manner to nucleons and their chiral partners. In this way it was possible to successfully describe nuclear matter ground-state properties (i.e., density, binding energy, and compressibility). In the mean-field approximation, and assuming homogeneous condensates, Ref. [91] reports the onset of a first-order phase transition at a density of about $2.5\rho_0$. Moreover, in the nonzero temperature study of Ref. [114] it could be shown that in a simplified version of the eLSM both aforementioned scalar resonances affect the chiral phase transition. Furthermore, it was shown that in the Bonn nucleon-nucleon potential [115] it is necessary to include both scalar-isoscalar states $f_0(500)$ and $f_0(1370)$.

The main focus of this thesis is the question whether inhomogeneous condensation takes place within the eLSM. Following former works in hadronic models, we first restrict ourselves to a CDW-type modulation for the spatial dependence of the condensate:

$$\langle\sigma\rangle \sim \cos(2fx) \ , \text{ and } \quad \langle\pi^3\rangle \sim \sin(2fx) \ , \tag{1.5}$$

where x is the spatial direction and f the wave vector. Guided by the study of nuclear matter ground-state properties in Ref. [91], we investigated the formation of a CDW for different choices for the chiral partner of the nucleon. It follows that, without any additional free parameters left, nuclear matter in the ground state is still a (homogeneous) liquid. For the cases discussed in the literature [82] chiral condensation remains homogeneous up to a baryon chemical potential of 975 MeV for

a mass of the chiral partner of the nucleon of 1500 MeV and a chemical potential of 1184 MeV for a mass of 1650 MeV. These correspond to densities of $2.5\rho_0$ and $5.1\rho_0$, followed by an inhomogeneous phase with a chiral density wavelength π/f of approximately 1.5 fm or 1.6 fm.

- Analytic expressions for inhomogeneous modulations are only known for rare cases, e.g. CDW-like modulations [60] or soliton-like structures [38]. Both can be described by the generalized Jacobi elliptic functions [39]. Even with this knowledge it is challenging to calculate the phase structure in higher dimensions [73]. A solid method to calculate general higher-dimensional modulations does not exist at present. Exploratory studies relied on selected higher-dimensional structures [76, 116]. A major aspect of this thesis is the development of a robust method to calculate inhomogeneous modulations without dimensional limitations. To this end a method motivated by lattice QCD is used [66]. As a result it follows that the finite-mode approach introduced here is capable to reproduce CDW and soliton-like modulations. The explicit form of the modulation serves not as an input, but rather follows from the minimization of an arbitrary Ansatz for the modulation. The applicability reaches from $1+1$ to $3+1$ dimensional models as well as for several inhomogeneous fields. An extension to higher-dimensional modulations is also possible.

  In the framework of the finite-mode approach it was not only possible to reproduce well-known results, but also exploratory studies could be performed. The phase structure of the GN model and the χGN model in $1+1$ dimensions could be reproduced. A detailed study of the NJL_2 revealed that the phase diagram coincides with the GN model, but there are many equivalent ground states. In the $3+1$ dimensional NJL model the recent findings on one-dimensional modulations could be confirmed [73]. In addition a new estimate of the size of the so-called inhomogeneous continent is done [117, 118]. A surprising occurrence is the finite size of the continent and a shape similar to the GN phase diagram at high chemical potential μ. The physical relevance of the inhomogeneous continent is still not understood. A study on the number of regulators is inconclusive since some parts of the continent change and some do not change with the number of regulators. This is in contrast to the homogeneous regime and the inhomogeneous island which remain unchanged.

The thesis is organized in the following way:
In chapter 2 the large-N_c scaling of the critical temperature is discussed.

To this end we introduce the NJL model in section 2.1 and its nonzero temperature behavior in section 2.2. In section 2.3 the linear σ-model at nonzero temperature is presented and the scaling mismatch compared to the NJL model is outlined. The concluding section 2.4 of this chapter introduces two extensions of the linear σ-model that lead to a correct scaling behavior.

The third chapter introduces the CDW in the eLSM. Section 3.1 shows how mesons are integrated into the eLSM and section 3.2 treats the baryons. Section 3.3 is preparatory for the nonzero-density study of the CDW in the eLSM and discusses the implications of the CDW to mesons and baryons. In section 3.4 a simplified eLSM is studied at nonzero density. Finally in section 3.5 the full eLSM including also a tetraquark state is tested for CDW formation at high density.

Chapter 4 concerns the development of the finite-mode approach. After some introductory remarks in section 4.1, the chapter is segmented into the study of $1+1$ dimensional models in section 4.2 and $3+1$ dimensional ones in section 4.3. First, in section 4.2.1 the GN model and several extensions are outlined. The next section 4.2.2 describes how the model is reformulated to fit into a box. In section 4.2.3 methods to fix the additional box parameters are outlined. The implementation of arbitrary inhomogeneous phases is presented in section 4.2.4. At last in section 4.2.5 the phase diagrams for the different $1+1$ dimensional models are presented. The structure of the section about $3+1$ dimensional models follows the structure of the section for $1+1$ dimensional ones. In section 4.3.1 the NJL model is reformulated in order to be calculated in a box. Section 4.3.2 concerns the optimization of the box parameters. The treatment of one-dimensional modulations in $3+1$ dimensions is addressed in section 4.3.3. The phase diagram of the NJL model is presented in section 4.3.4.

Finally, conclusion, summary, and outlook are presented in chapter 5.

Chapter 2

Scaling in the large-N_C limit

This chapter is based on Refs. [119, 120].

2.1 NJL model

The NJL model is an effective theory of QCD in the low-energy regime [20, 22, 23, 24]. It was proposed in a pre-QCD era in terms of nucleon fields (quarks and gluons were unknown) in order to describe the interaction between nucleons. Later on it was rewritten in terms of quarks, whose interactions via gluons are effectively treated by a Fermi-like four-point interaction. This interaction shares some symmetries with QCD. For low energies and small bare quark masses, chiral symmetry is one of the most important symmetries of QCD. The NJL model considers dynamical chiral symmetry breaking and the ensuring generation of the constituent quark masses. Thus, it is suitable to describe light mesons and baryons. Nevertheless, there are some restrictions. Basic features of QCD, like confinement, are not realized. In the NJL model at low temperatures quarks propagate freely and do not necessarily manifest themselves in bound states. It is possible to mimic the confining potential of the gluons and map their thermodynamical behavior [16] but still there will be free quark states. Moreover, in contrast to QCD, the NJL model is not renormalizable and therefore a regularization scheme has to be applied. Besides the employed scheme, the energy scale (associated to a cutoff Λ) is an important input of the model since the resulting physics depends on this choice (it can be argued that the regularization is a crude approximation of a crucial feature of QCD: asymptotic freedom [24]).

Notice, however, that many important relations that hold for QCD also hold for the NJL model, e.g the Gell-Mann-Oakes-Renner relation [121] and the Goldberger-Treiman relation [122]. Despite all these restrictions the NJL

model is used to compute an approximate QCD phase diagram. The accuracy of this description can be assessed with large-N_c arguments. An important quantity is the temperature T_c for the chiral phase transition.

In order to study the large-N_c behavior of the chiral phase transition in the medium, we can restrict ourselves to two flavors, $N_f = 2$. Chiral symmetry is not an exact symmetry of QCD. However, since the current masses of u and d quarks are small compared to the resulting constituent quark masses, it is justified to treat them as massless fields (chiral limit). Since at this point no flavor-specific calculations are performed and both flavors are treated in the same way, the flavor index is suppressed and additional prefactors are absorbed in the coupling constant. The basic symmetry of the NJL model is $SU_V(2) \otimes SU_A(2) \otimes U_V(1)$ and is described by the Lagrangian:

$$\mathscr{L} = \sum_{i=1}^{N_c} \bar{\psi}_i \left(\imath \partial\!\!\!/ - m_q \right) \psi_i + \frac{3G}{N_c} \left[\left(\sum_{i=1}^{N_c} \bar{\psi}_i \psi_i \right)^2 + \left(\sum_{i=1}^{N_c} \bar{\psi}_i \imath \gamma_5 \vec{\tau} \psi_i \right)^2 \right] \ , \quad (2.1)$$

where ψ_i is the quark spinor, m_q is the bare quark mass and $\vec{\tau}$ are the Pauli matrices. The index $i = 1, \ldots, N_c$ labels the fundamental color of the state. G is the coupling constant with dimension $[G] = \text{energy}^{-2}$ the N_c-scaling is made explicit by the factor $3/N_c$ in front of G.

2.2 NJL model as a mean-field theory

The Lagrangian allows to pair left-handed and right-handed quarks in the vacuum to yield the chiral condensate:

$$\sum_{i=1}^{N_c} \left\langle \bar{\psi}_i \psi_i \right\rangle = \phi \ . \quad (2.2)$$

This leads to the mean-field part of the Lagrangian:

$$\begin{aligned} \mathscr{L}_{\text{mf}} &= \sum_{i=1}^{N_c} \bar{\psi}_i \left(\imath \partial\!\!\!/ - m_q \right) \psi_i + 2 \frac{3G}{N_c} \sum_{j=1}^{N_c} \left\langle \bar{\psi}_j \psi_j \right\rangle \sum_{i=1}^{N_c} \bar{\psi}_i \psi_i - \frac{3G}{N_c} \left(\sum_{i=1}^{N_c} \left\langle \bar{\psi}_i \psi_i \right\rangle \right)^2 \\ &= \sum_{i=1}^{N_c} \bar{\psi}_i \left(\imath \partial\!\!\!/ - m_q + 2 \frac{3G}{N_c} \phi \right) \psi_i - \frac{3G}{N_c} \phi^2 \\ &= \sum_{i=1}^{N_c} \bar{\psi}_i \left(\imath \partial\!\!\!/ - m^* \right) \psi_i - \frac{\lambda}{2} m_0^2 \ , \end{aligned} \quad (2.3)$$

with:

$$\lambda = \frac{N_c}{6G} \ , \ \text{and} \quad m^* = m_q + m_0 \ , \tag{2.4}$$

which are the coupling λ and the constituent quark mass m^*. In the chiral limit the constituent quark mass $m^* = m_0$ is defined to be directly proportional to the chiral condensate:

$$m_0 = -2\frac{3G}{N_c}\sum_{i=1}^{N_c}\left\langle\bar{\psi}_i\psi_i\right\rangle = -2\frac{3G}{N_c}\phi \ . \tag{2.5}$$

It is now possible to integrate out the quark degrees of freedom. The resulting partition function Z is:

$$\begin{aligned} Z &= N\int\prod_{i=1}^{N_c}\left(D\psi_i^\dagger D\psi_i\right)\exp\left[-\int_0^\beta d\tau\int d^3x\ \mathscr{L}_{\rm mf}\right] \\ &= N'\det Q\exp\left[-\int_0^\beta d\tau\int d^3x\ \frac{\lambda}{2}m_0^2\right] \ , \end{aligned} \tag{2.6}$$

with $\beta = 1/T$, the operator $Q = \gamma_0(\not{p} + \gamma_0\mu - m^*)$ and $m^* = m_q + m_0$.

The thermodynamic grand canonical potential Ω in the mean-field theory follows as:

$$\Omega = -\frac{1}{\beta}\ln Z = \frac{1}{\beta}N_c\ln\det Q - \frac{1}{\beta}\int_0^\beta d\tau\int d^3x\ \frac{\lambda}{2}m_0^2 \ , \tag{2.7}$$

which is equivalent to the grand canonical potential in the large-N_c limit. Using standard expressions [123, 124, 125] we evaluate $\ln\det Q$:

$$\begin{aligned} \Omega =& N_c 2V\int\frac{d^3p}{(2\pi)^2}\left[\omega + \frac{1}{\beta}\ln\left(1+e^{-\beta(\omega-\mu)}\right) + \frac{1}{\beta}\ln\left(1+e^{-\beta(\omega+\mu)}\right)\right] \\ & - V\frac{\lambda}{2}m_0^2 \ , \end{aligned} \tag{2.8}$$

where $\omega = \sqrt{p^2 + m^{*2}}$ is the energy and the spatial integral results in the volume V. At this point it is clear why in the large N_c-limit all further contributions from higher loop orders are neglected: they are suppressed due to factors of $1/N_c$. Also one should keep in mind that in eq. (2.8), since $\lambda \propto N_c$, the second part is proportional to N_c. This allows to reduce the role of N_c to be an overall factor of Ω and therefore it does not affect the thermodynamical behavior.

As already mentioned in the introduction, for zero temperature a quark condensate forms and the quarks obtain an additional mass contribution dependent on the value of the condensate. Similarly to QCD, it is expected that in the chiral limit, the condensate vanishes exactly for sufficient high temperature and chiral symmetry is restored. It has been shown that for QCD [52, 53] this transition is independent of the number of colors. In conclusion, the NJL model is a suitable approach to describe effectively the chiral phase transition of QCD.

Because of the divergent integral $\int d^3p\ \omega$ in eq. (2.8) the NJL model has to be regularized. The NJL model is not renormalizable and therefore the choice of the regularization scheme has an influence on the extracted thermodynamical quantities. Two different regularization methods will be introduced. One consists of a 3d cutoff in momentum space (which breaks Lorentz invariance) and the other is the so-called Pauli-Villars scheme (which preserves Lorentz invariance). In both cases a new parameter Λ is introduced, which has to be adjusted to physical quantities. The results presented in this chapter are general and do not depend on the choice of the regularization scheme. The two schemes lead only to slightly different critical temperatures, but they do not affect the large-N_c scaling. However, the choice of the proper regularization scheme is important for the considerations in chapter IV.

We now describe in more detail the regularization schemes:

- For the 3d momentum cutoff the upper integration limit is simply replaced according to:

$$\int_0^\infty \frac{dp\ p^2}{2\pi^2}\omega \to \int_0^{\Lambda_{3d}} \frac{dp\ p^2}{2\pi^2}\omega\ , \tag{2.9}$$

  then the integration is straightforward and leads to the expression:

$$\frac{1}{16\pi^2}\left[\Lambda_{3d}\sqrt{\Lambda_{3d}^2+m^{*2}}\left(2\Lambda_{3d}^2+m^{*2}\right)-m^{*4}\mathrm{Arsinh}\left(\frac{\Lambda_{3d}}{m^*}\right)\right]\ . \tag{2.10}$$

  The 3d momentum cutoff forces all allowed momenta to be smaller than a cutoff Λ_{3d}. For this kind of regularization Lorentz invariance is broken. In a thermodynamical context a preferred reference frame already exists: this is the reference frame of the medium.

- The Pauli-Villars regularization is more involved [22, 126]. An arbitrary number $N > 1$ of regulating masses M_a and coefficients C_a are introduced. These parameters are chosen in a way that the following difference is finite:

$$\sum_{a=0}^{N} C_a \int_0^\infty dk\ k^2 \left(\sqrt{k^2+M_a(m^*)^2}-\sqrt{k^2+M_a(0)^2}\right)\ , \tag{2.11}$$

with:

$$M_a(m^*)^2 = m^{*2} + \alpha_a \Lambda_{PV}^2 \ . \tag{2.12}$$

In order for the difference to be finite one must impose the conditions:

$$\sum_{a=0}^{N} C_a = 0 \ , \text{ and } \quad \sum_{a=0}^{N} C_a M_a^2 = 0 \ . \tag{2.13}$$

With the choice $\alpha_0 = 0$ and $C_0 = 1$ and for $N = 2$ this leads to:

$$\begin{aligned} C_1 + C_2 &= -1 \ , \\ \alpha_1 C_1 + \alpha_2 C_2 &= 0 \ . \end{aligned} \tag{2.14}$$

A solution to these equations is $\alpha_1 = 2$ and $\alpha_2 = 1$ with $C_1 = 1$ and $C_2 = -2$. The Pauli-Villars scheme preserves Lorentz invariance. Also the suppression increases with momentum but is smooth, since it allows for contributions larger than the cutoff Λ_{PV}.

Both regularization schemes result in an NJL model which has two parameters in the chiral limit: the coupling constant G and the cutoff Λ. These parameters have to adjusted to fit two physical quantities e.g. the pion decay constant and the constituent quark mass (alternatively it is possible to use the critical temperature T_c and the quark condensate). In any case, one sees that the extracted physical quantities can depend on the choice of the regularization scheme and its parameters.

The behavior at nonzero temperature and density is obtained by minimizing the pressure with respect to the chiral condensate or the constituent quark mass:

$$0 = \frac{\partial P}{\partial m^*} \ , \qquad \text{with} \qquad P = T \frac{\partial}{\partial V} \Omega \ . \tag{2.15}$$

Using eq. (2.8) and the 3d momentum cutoff the constituent quark mass m^* as a function of T [22] reads in the mean-field approximation:

$$1 = \frac{m_q}{m^*} + 6G \int_0^{\Lambda_{3d}} \frac{dk \ k^2}{\pi^2} \frac{2 \tanh\left(\frac{\sqrt{k^2+m^{*2}}}{2T}\right)}{\sqrt{k^2+m^{*2}}} \ , \tag{2.16}$$

where the cutoff Λ_{3d} regularizes the loop integral. In the chiral limit $m_q \to 0$ the critical temperature for chiral symmetry restoration T_c is obtained as the temperature at which the effective mass m^* (and therefore also the chiral

condensate $\langle\bar{\psi}_i\psi_i\rangle$) vanishes. To leading order in N_c and in the chiral limit ($m_q = 0$ and $m_0 = m^*$) the expression for T_c reads:

$$T_c(N_c) \simeq \Lambda_{3d}\sqrt{\frac{3}{\pi^2}}\sqrt{1-\frac{\pi^2}{6\Lambda_{3d}^2 G}} \propto N_c^0 \ . \tag{2.17}$$

The phase transition is of second order and is independent of N_c.

For $m_q > 0$, the order of the phase transition changes to a crossover transition. In this case we define the point at which the first derivative $|dm^*/dT|$ is maximized as the (pseudo-)critical temperature. However, the transition temperature is also N_c-independent. Including the s-quark and (axial-)vector degrees of freedom does not change the result, since T_c is determined by general scaling arguments. Moreover, adding the 't Hooft term which describes the $U_A(1)$ anomaly also does not modify the result, because at T_c the contributions from the 't Hooft term are suppressed in the large-N_c limit. We thus conclude that the critical temperature for chiral symmetry restoration (second order or crossover) is independent of the number of colors in all versions of the NJL model. The scaling is, as expected, the same as for the deconfinement phase transition as it is obtained from QCD.

2.3 Linear σ-model

The linear σ-model is a purely hadronic model constructed from the requirement of chiral symmetry and its spontaneous breaking [26, 29, 105], in which the pions emerge as Goldstone bosons in the chiral limit. Namely, the chiral symmetry is spontaneously broken in the vacuum and a non-vanishing chiral condensate emerges. This phenomenon leads to a mass splitting between the chiral partners. At sufficient high temperature chiral symmetry is restored and the chiral partners become degenerate in mass.

In order to study the large-N_c behavior of the chiral phase transition we consider, as in the NJL model, the two-flavor case $N_f = 2$. We restrict ourselves to the most simple version of the model, which includes only the chiral partners σ and $\vec{\pi}$. However, our conclusions are general for all hadronic σ-models.

The large-N_c scaling is obtained by using general large-N_c arguments: for large N_c the meson masses are independent of N_c, while the coupling of the meson interactions depends on N_c. Decays scale as $1/\sqrt{N_c}$ and four-point meson interactions scale as $1/N_c$. It is convenient to implement this scaling behavior via a rescaling of the four-point coupling $\lambda \to \frac{3}{N_c}\lambda$. The Lagrangian

for the standard $SU(2)$ linear σ-model reads [26]:

$$\mathcal{L}_\sigma(N_c) = \frac{1}{2}(\partial_\mu \Phi)^2 + \frac{1}{2}\mu^2\Phi^2 - \frac{\lambda}{4}\frac{3}{N_c}\Phi^4 \ , \tag{2.18}$$

where $\Phi^t = (\sigma, \vec{\pi})$ describes the scalar field σ and the pseudoscalar pion isospin triplet $\vec{\pi}$. For $\mu^2 > 0$ chiral symmetry is broken and a nonzero chiral condensate emerges as:

$$\varphi_0 = \varphi(T=0) = \mu\sqrt{\frac{N_c}{3\lambda}} \ . \tag{2.19}$$

The large-N_c scaling of the chiral condensate compensates the scaling in the four-point coupling and thus results in N_c-independent masses. The tree-level masses for the sigma and pions fields are:

$$\begin{aligned} m_\sigma^2 &= 3\frac{3\lambda}{N_c}\varphi_0^2 - \mu^2 = 3\lambda f_\pi^2 - \mu^2 \ , \\ m_\pi^2 &= 0 \ . \end{aligned} \tag{2.20}$$

It follows that the chiral condensate φ in the vacuum can be rewritten as:

$$\varphi_0 = \sqrt{\frac{N_c}{3}} f_\pi \ . \tag{2.21}$$

In order to study the behavior of the linear σ-model at nonzero temperature we apply the Cornwall-Jackiw-Tomboulis (CJT) formalism [127] in the so-called double-bubble approximation. Similar studies are common in literature and can be found in refs. [128, 129, 130] and Refs. therein. The thermodynamical behavior is found by minimizing the pressure with respect to the physical masses M_π, M_σ, and the chiral condensate φ:

$$\begin{aligned} 0 &= \frac{\partial P}{\partial \varphi} \ , \\ 0 &= \frac{\partial P}{\partial M_\sigma} \ , \\ 0 &= \frac{\partial P}{\partial M_\pi} \ . \end{aligned} \tag{2.22}$$

The gap equations read:

$$\begin{aligned} 0 &= \varphi(T)\left(\frac{3\lambda}{N_c}\varphi(T)^2 - \mu^2\right) + 3\frac{3\lambda}{N_c}\varphi(T)\left(\int G_\sigma + \int G_\pi\right) \ , \\ M_\sigma(T)^2 &= 3\frac{3\lambda}{N_c}\varphi(T)^2 - \mu^2 + 3\frac{3\lambda}{N_c}\left(\int G_\sigma + \int G_\pi\right) \ , \\ M_\pi(T)^2 &= \frac{3\lambda}{N_c}\varphi(T)^2 - \mu^2 + \frac{3\lambda}{N_c}\left(\int G_\sigma + 5\int G_\pi\right) \ . \end{aligned} \tag{2.23}$$

Neglecting the vacuum fluctuations, the tadpole integrals over the full meson propagators G_σ and G_π are:

$$\int G_i = \int_0^\infty \frac{dk\ k^2}{2\pi^2\sqrt{k^2+M_i^2}} \left[\exp\left(\frac{\sqrt{k^2+M_i^2}}{T}\right) - 1\right]^{-1} , \tag{2.24}$$

where M_i is the physical mass of either the σ meson or the pion π.

In the chiral limit and at the critical temperature only one of these equations is relevant since the chiral condensate and the masses vanish:

$$\begin{aligned} M_\pi(T_c) &= 0 \ , \\ M_\sigma(T_c) &= 0 \ , \\ \varphi(T_c) &= 0 \ . \end{aligned} \tag{2.25}$$

Dropping the trivial solution, the gap equation for the chiral condensate at the critical temperature reduces to:

$$0 = -\mu^2 + 18\frac{\lambda}{N_c}\int G \ , \tag{2.26}$$

with a tadpole contribution that can be calculated analytically:

$$\int G = \int_0^\infty \frac{dk\ k}{2\pi^2} \left[\exp\left(\frac{k}{T_c}\right) - 1\right]^{-1} = \frac{T_c^2}{12} \ . \tag{2.27}$$

The critical temperature as a function of N_c is then obtained as:

$$T_c(N_c) = \sqrt{2} f_\pi \sqrt{\frac{N_c}{3}} \propto N_c^{1/2} \ . \tag{2.28}$$

For $N_c = 3$ the known result $T_c = \sqrt{2} f_\pi$ from Ref. [129] is obtained. The critical temperature is N_c-dependent and increases for increasing N_c. As a consequence, for $N_c \to \infty$ the chiral phase transition will not take place at all. This is the case for all purely hadronic models. Namely, hadronic models in the large-N_c limit consist of a gas of non-interacting mesons: meson loops which are responsible for the restoration of chiral symmetry are suppressed. In the large-N_c limit the chiral restoration inevitably disappears.

In conclusion, purely hadronic models are not in agreement with the large-N_c limit of QCD at high temperature. This result changes if N_c-dependent degrees of freedom such as gluons and/ or quarks [131] are introduced or if parameters with an explicit temperature dependence are used.

2.4 Phenomenologically improved linear σ-model

The result of the previous section is puzzling. Both, the NJL model and the linear σ-model, are built from the same symmetries. Moreover, the linear σ-model can be obtained as the hadronized version of the NJL model. However, the hadronization procedure is only performed at a single temperature $T = 0$. A more convenient way would be to hadronize at each temperature T and, as a consequence, the coupling constants in the linear σ-model would become functions of T. In particular, the chiral condensate $\varphi(T)$ of the σ-model should not be larger than in the corresponding NJL model. In the following we will discuss two improvements of the linear σ-model in order to overcome the mismatch with QCD in the N_c-scaling of T_c.

Explicit temperature dependence: A hadronization scheme applied at every temperature should lead to temperature-dependent parameters. In Refs. [132, 133] it is argued that the T^2-scaling of the order parameter is general and should hold also in the large-N_c limit. Therefore, we choose the mass parameter μ to be temperature-dependent:

$$\mu^2 \to \mu(T)^2 = \mu^2 \left(1 - \frac{T^2}{T_d^2}\right) , \tag{2.29}$$

where a new temperature scale T_d (of the order of Λ_{QCD}) is introduced. This term modifies the gap equation (2.23) and leads to a modified critical temperature with a different large-N_c scaling:

$$T_c(N_c) = T_d \frac{1}{\sqrt{1 + \frac{T_d^2}{2f_\pi^2}\frac{3}{N_c}}} . \tag{2.30}$$

Thus, for a large number of colors the critical temperature is constant and coincides with the newly introduced scale $T_c = T_d$. It is also clear how the mesons affect the chiral phase transition. They are responsible for the term $\propto 3/(N_c f_\pi^2)$ in eq. (2.30) and thus lead to a decrease of T_c: $T_c < T_d$ for any finite value of N_c. Thus, mesonic fluctuations represent only a large-N_c subdominant contribution to the critical value T_c. In the case $N_c = 3$, using the numerical value $f_\pi = 92.4$ MeV and setting the temperature scale $T_d = \Lambda_{QCD} \simeq 225$ MeV, the critical temperature T_c is lowered to $T_c \simeq 113$ MeV. Interestingly, in the framework of sigma models with (axial-)vector mesons, one has to make the replacement $f_\pi \to Z f_\pi$ with $Z \simeq 1.67$ [29]. This leads to a critical temperature $T_c \simeq 157$ MeV, which is remarkably close to lattice

results [2, 3]. With the help of the modification in eq. (2.29) the linear σ-model respects the large-N_c limit and is compatible with the NJL model. Moreover these numerical results show that the role of mesons is stable for the case $N_c = 3$.

From eq. (2.26) it follows that our result for $T_c(N_c \gg 3)$ depends only on the ratio μ^2/λ. Thus, including a T-dependence of the parameter λ would not alter the results, as long as the ratio $\mu^2(T)/\lambda(T)$ scales quadratically as in eq. (2.29). In general, it is sufficient that the ratio $\mu^2(T)/\lambda(T)$ goes to zero for $T \to T_d$ in order to obtain the desired property:

$$\lim_{N_c \to \infty} T_c(N_c) = T_d \ . \tag{2.31}$$

Notice that the quadratic form of $\mu(T)$ in eq. (2.29) mimics well the qualitative behavior of quark-loop contributions to mesonic masses, see Ref. [22]. For this reason we expect that the quark-meson model of Ref. [17], which naturally implements these contributions, shows the correct large-N_c scaling of T_c.

The additional scale T_d does not only affect the critical temperature but also the order of the phase transition. To show this, we study the case where $N_c = 3$. The full Lagrangian including a second scale T_d reads:

$$\mathcal{L}_\sigma(T_d) = \frac{1}{2}(\partial_\mu \Phi)^2 + \frac{1}{2}\mu^2 \left(1 - \frac{T^2}{T_d^2}\right) \Phi^2 - \frac{\lambda}{4}\frac{3}{N_c}\Phi^4 + \epsilon\sigma \ , \tag{2.32}$$

with an explicit symmetry breaking term $\epsilon\sigma$. All parameters can be fixed by the masses and the pion decay constant:

$$\epsilon = f_\pi m_\pi^2 \ , \quad \lambda = \frac{m_\sigma^2 - m_\pi^2}{2 f_\pi^2} \ , \quad \mu^2 = \frac{m_\sigma^2 - 3m_\pi^2}{2} \ . \tag{2.33}$$

The quantity T_d is set to the value $T_d = 0.27$ GeV. The vacuum properties are chosen as follows: the mass of the σ-field is $m_\sigma = 1.2$ GeV (for the discussion of the value of the σ mass in the vacuum, see Refs. [30, 105] and refs. therein), the mass of the pion π is $m_\pi = 0.135$ GeV, and the pion decay constant is $f_\pi = 0.093$ GeV.

The nonzero-temperature behavior of the chiral condensate φ is strongly affected by the additional temperature scale T_d. It is remarkable that the order of the phase transition is changed from first order to a crossover transition. In addition, the interplay of the temperature scale T_d and the meson loops leads to a lower critical temperature $T_c \approx 200$ MeV. Both phenomena can be seen in Fig. 2.1, where the case $N_c \to \infty$ is also included: in this limit the chiral symmetry is restored because of the new temperature scale

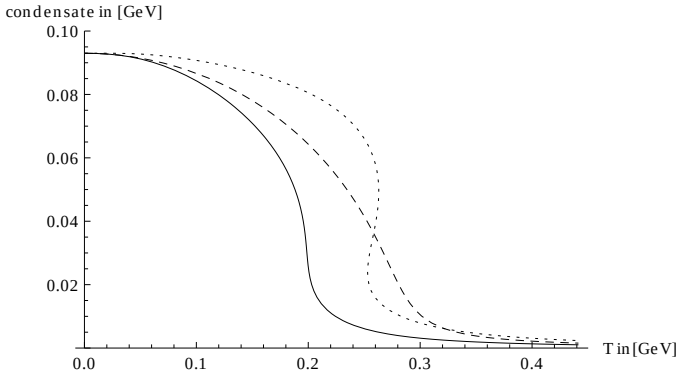

Figure 2.1: The chiral condensate for different number of colors and temperature scales T_d. Continuous line: $N_c = 3$ and $T_d = 270$ MeV. Dotted line: $N_c = 3$ and $T_d \to \infty$. Dashed line: $N_c \to \infty$ and $T_d = 270$ MeV (in this case $\varphi(T)$ is rescaled by a factor $1/N_c$).

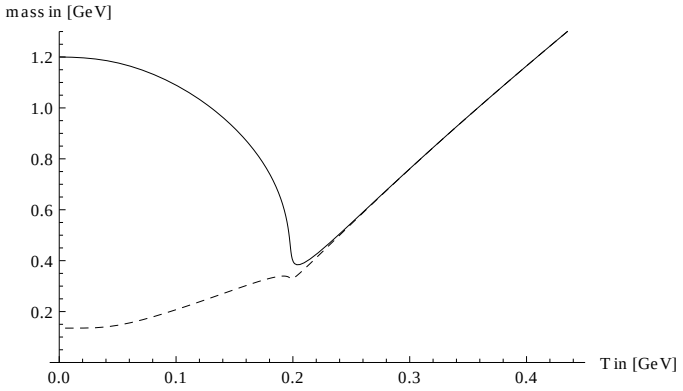

Figure 2.2: The masses M_π and M_σ as a function of the temperature. The dashed line represents the mass of the pions and the continuous line the mass of the σ. Above a critical temperature of $T_c \approx 200$ MeV the masses become degenerate.

T_d (and not via mesonic loops). The nonzero-temperature behavior for the masses is shown in Fig. 2.2. Until the critical temperature T_c is reached the temperature dependence of the pion mass and the σ mass varies only slowly. Close to T_c the mass of σ drops and slightly above T_c it becomes degenerate with the pion. At high temperature both masses rise linearly.

Inclusion of the Polyakov loop: Our second suggestion for improving the linear σ-model is to incorporate the coupling to the Polyakov loop [13]. In the pure gauge theory the expectation value of the Polyakov loop $l(T) = |\langle l(x) \rangle|$ is an order parameter for the deconfinement phase transition, where $l = 0$ in the confined phase and $l \to 1$ in the deconfined phase, see the review in Ref. [134] and refs. therein.

Following Ref. [135] (for a similar approach see also Ref. [136]) we couple the σ-model to the Polyakov loop:

$$\mathcal{L}_{\sigma\text{-Pol}}(N_c) = \mathcal{L}_\sigma(N_c) + \frac{\alpha N_c}{4\pi} |\partial_\mu l|^2 T^2 - \mathcal{V}(l) - \frac{h^2}{2} \Phi^2 |l|^2 T^2 \ , \tag{2.34}$$

where $\mathcal{L}_\sigma(N_c)$ is taken from eq. (2.18) and the Polyakov loop is coupled to the meson fields. Moreover, a kinetic term and a potential $\mathcal{V}(l)$ for the Polyakov field l have been introduced. Since we are only interested in the large-N_c behavior, the precise form of $\mathcal{V}(l)$ is irrelevant in the following. Terms of the kind $\sim l T^2 \Phi^2$ could also be included [136] but they would not affect the overall N_c-scaling, although they might change the order of the phase transition. Applying the CJT formalism in the double-bubble approximation the gap equation for the condensate $\varphi(T)$ reads:

$$0 = \varphi(T)^2 - \frac{N_c}{3\lambda} \left(\mu^2 - h^2 |l|^2 T^2 \right) + 3 \int (G_\sigma + G_\pi) \ , \tag{2.35}$$

from which the following expression for the critical temperature T_c is derived:

$$T_c = \frac{\mu}{\sqrt{h^2 |l(T_c)|^2 + \frac{6\lambda}{N_c}}} \ . \tag{2.36}$$

Assuming here that $l(T_c)$ is independent of N_c, we again obtain $T_c \propto N_c^0$ in the limit $N_c \to \infty$. While the independence of $l(T_c)$ has not been analytically proven, it is in agreement with recent lattice simulations of Yang Mills theories (e.g. Ref. [53]), in which $l(T)$ has been investigated for increasing N_c. The important point here is that it is natural to recover the desired large-N_c limit when the hadronic model is coupled to the Polyakov loop. The reason for this is that the chiral phase transition is triggered by the Polyakov loop

[137].

In conclusion, purely hadronic models fail to describe the chiral phase transition in the QCD in large-N_c limit. Nevertheless, it is possible to motivate and implement corrections that lead to the expected N_c dependence. Hadronic degrees of freedom play a sizable role close to T_c and lower the critical temperature substantially. However, they are not the driving force behind this transition. Quarks and gluons dominate the thermodynamics close to the phase transition and at higher temperatures.

Chapter 3

Chiral density wave in the eLSM

The chapter is based on Refs. [138, 139].

3.1 Mesons in the eLSM

The extended Linear Sigma Model (eSLM) is a generalization of the linear σ-model which has been developed in Refs. [29, 30, 80]. The eSLM is based on chiral symmetry and dilatation invariance. Moreover, vector and axial-vector mesons are taken into account. The mesonic Lagrangian is constructed in the following way: different quark-antiquark bilinear terms are identified with meson fields sharing the same quantum numbers:

$$\bar{\psi}_j \Gamma \psi_i \equiv \text{Mesons}_{ij} \ , \tag{3.1}$$

with $\psi = (u, d)$ and $\Gamma = \{\mathbb{1}_4,\ \gamma_5,\ \gamma^\mu,\ \gamma_5\gamma_\mu\}$, each leading to mesons with different quantum numbers. Here we present the eLSM for $N_f = 2$, but this Ansatz can be generalized to any number of flavors N_f, e.g. for the $N_f = 3$ case a detailed study can be found in Ref. [30]. The four resulting building blocks are the scalar/ pseudoscalar and the vector/ axial-vector fields. The (pseudo)scalars have the following structure:

$$\begin{aligned} \Phi &= \sum_{a=0}^{3} \phi_a t_a = (\sigma + \imath\eta_N)\, t^0 + (\vec{a}_0 + \imath\vec{\pi}) \cdot \vec{t}\ , \\ \Phi^\dagger &= \sum_{a=0}^{3} \phi_a t_a = (\sigma - \imath\eta_N)\, t^0 + (\vec{a}_0 - \imath\vec{\pi}) \cdot \vec{t}\ , \end{aligned} \tag{3.2}$$

where $\vec{t} = \vec{\tau}/2$, with the vector of Pauli matrices $\vec{\tau}$, and $t_0 = \mathbb{1}_2/2$ (In the case of $N_f = 3$ the Pauli matrices are replaced by the Gell-Mann matrices). The

vector mesons V^μ and the axial-vector mesons A^μ have a similar structure:

$$V^\mu = \sum_{a=0}^{3} V_a^\mu t_a = \omega^\mu t^0 + \vec{\rho}^\mu \cdot \vec{t}\,,$$
$$A^\mu = \sum_{a=0}^{3} A_a^\mu t_a = f_1^\mu t^0 + \vec{a}_1^\mu \cdot \vec{t}\,. \tag{3.3}$$

It is useful to introduce right-handed and left-handed fields R^μ and L^μ:

$$R^\mu \equiv V^\mu - A^\mu = (\omega^\mu - f_1^\mu)\, t_0 + (\vec{\rho}^\mu - \vec{a}_1^\mu) \cdot \vec{t}\,,$$
$$L^\mu \equiv V^\mu + A^\mu = (\omega^\mu + f_1^\mu)\, t_0 + (\vec{\rho}^\mu + \vec{a}_1^\mu) \cdot \vec{t}\,. \tag{3.4}$$

The transformation rules under a chiral $U(2)_L \times U(2)_R$ transformation for the fields are given by:

$$\Phi \to U_L \Phi U_R^\dagger\,,$$
$$\Phi^\dagger \to U_R \Phi^\dagger U_L^\dagger\,,$$
$$R^\mu \to U_R R^\mu U_R^\dagger\,,$$
$$L^\mu \to U_L L^\mu U_L^\dagger\,, \tag{3.5}$$

where U_L and U_R are independent $U(2)$ unitary matrices. Using these transformation rules, one can construct chirally invariant terms. Later it will be argued that, in order to simultaneously keep analyticity in the dilaton field and dilatation invariance [79], only terms up to fourth order need to be considered. The final result is summarized by the following Lagrangian:

$$\begin{aligned}
\mathscr{L}_M = {} & \mathrm{Tr}\left[(D_\mu\Phi)^\dagger (D^\mu\Phi) - m^2\Phi^\dagger\Phi - \lambda_2\left(\Phi^\dagger\Phi\right)^2\right] - \lambda_1\left(\mathrm{Tr}\left[\Phi^\dagger\Phi\right]\right)^2 \\
& + c\left(\det\Phi^\dagger - \det\Phi\right)^2 + h_0\mathrm{Tr}\left[\Phi^\dagger + \Phi\right] \\
& - \frac{1}{4}\mathrm{Tr}\left[L_{\mu\nu}L^{\mu\nu} + R_{\mu\nu}R^{\mu\nu}\right] + \frac{1}{2}m_1^2\mathrm{Tr}\left[L_\mu L^\mu + R_\mu R^\mu\right] \\
& + \frac{1}{2}h_1\mathrm{Tr}\left[\Phi^\dagger\Phi\right]\mathrm{Tr}\left[L_\mu L^\mu + R_\mu R^\mu\right] + h_2\mathrm{Tr}\left[\Phi^\dagger L^\mu L_\mu\Phi + \Phi R^\mu R_\mu\Phi^\dagger\right] \\
& + 2h_3\mathrm{Tr}\left[\Phi R_\mu\Phi^\dagger L^\mu\right] - 2\imath g_2\left(\mathrm{Tr}\{L_{\mu\nu}[L^\mu, L^\nu]\} + \mathrm{Tr}\{R_{\mu\nu}[R^\mu, R^\nu]\}\right) \\
& - 2g_3\{\mathrm{Tr}[(\partial_\mu R_\nu + \partial_\nu R_\mu)\{R^\mu, R^\nu\}] + \mathrm{Tr}[(\partial_\mu L_\nu + \partial_\nu L_\mu)\{L^\mu, L^\nu\}]\} \\
& + g_4\{\mathrm{Tr}[L^\mu L^\nu L_\mu L_\nu] + \mathrm{Tr}[R^\mu R^\nu R_\mu R_\nu]\} \\
& + g_5\{\mathrm{Tr}[L^\mu L_\mu L^\nu L_\nu] + \mathrm{Tr}[R^\mu R_\mu R^\nu R_\nu]\} \\
& + g_6\mathrm{Tr}[R^\mu R_\mu]\mathrm{Tr}[L^\nu L_\nu] + g_7\{\mathrm{Tr}[R^\mu R_\mu]\mathrm{Tr}[R^\nu R_\nu] + \mathrm{Tr}[L^\mu L_\mu]\mathrm{Tr}[L^\nu L_\nu]\}\,,
\end{aligned} \tag{3.6}$$

with the short notation for the covariant derivative:

$$D^\mu\Phi = \partial^\mu\Phi - \imath g_1(\Phi R^\mu - L^\mu\Phi) \ , \tag{3.7}$$

and the field-strength tensors of the left- and right-handed fields:

$$\begin{aligned} L^{\mu\nu} &= \partial^\mu L^\nu - \partial^\nu L^\mu \ , \\ R^{\mu\nu} &= \partial^\mu R^\nu - \partial^\nu R^\mu \ . \end{aligned} \tag{3.8}$$

Spontaneous symmetry breaking is realized for $m^2 < 0$ (Mexican-hat form of the potential). The term proportional to c represents the axial anomaly. The nonzero bare quark masses lead to explicit chiral symmetry breaking: this is modelled by the term proportional to h_0.

Besides the terms proportional to c (axial anomaly) and h_0 (bare quark masses), dilatation invariance of $\mathscr{L}_M$ is broken by the dimensionful coupling constants m^2 and m_1^2. The breaking of dilatation invariance is a general feature of models with dimensionful coupling constants. However, in a model where these emerge only as the vacuum expectation value of other fields, dilatation invariance in preserved [79]. In order to render the eLSM dilatation invariant these dimensionful coupling constants are replaced with the condensate of the dilaton field, $\bar{G}$:

$$\begin{aligned} \alpha G^2 \mathrm{Tr}\left[\Phi^\dagger\Phi\right] &\to \alpha\bar{G}^2\mathrm{Tr}\left[\Phi^\dagger\Phi\right] \equiv m^2\mathrm{Tr}\left[\Phi^\dagger\Phi\right] \ , \\ \beta G^2 \mathrm{Tr}\left[L_\mu L^\mu + R_\mu R^\mu\right] &\to \beta\bar{G}^2\mathrm{Tr}\left[L_\mu L^\mu + R_\mu R^\mu\right] \equiv m_1^2\mathrm{Tr}\left[L_\mu L^\mu + R_\mu R^\mu\right] \ , \end{aligned} \tag{3.9}$$

with the dimensionless coupling constants α and β.

The condensation ($\sigma \to \sigma + \phi$) leads to mixing terms between η_N-f_μ^1 and $\vec{\pi}$-$\vec{a}_1^\mu$. These terms arise from the covariant derivatives:

$$\begin{aligned} \mathrm{Tr}\left[\left(D_\mu\Phi\right)^\dagger\left(D^\mu\Phi\right)\right] &\overset{\sigma\to\sigma+\phi}{=} \frac{1}{2}\left(\partial_\mu\sigma + g_1\vec{\pi}\cdot\vec{a}_{1\mu} + g_1\eta_N f_{1\mu}\right)^2 \\ &\quad + \frac{1}{2}\left(\partial_\mu\eta_N - g_1\sigma f_{1\mu} - g_1\phi f_{1\mu} - g_1\vec{a}_0\cdot\vec{a}_{1\mu}\right)^2 \\ &\quad + \frac{1}{2}\left(\partial_\mu\vec{a}_0 + g_1\vec{\rho}_\mu\times\vec{a}_0 + g_1\eta_N\vec{a}_{1\mu} + g_1\vec{\pi}f_{1\mu}\right)^2 \\ &\quad + \frac{1}{2}\left(\partial_\mu\vec{\pi} - g_1\vec{\pi}\times\vec{\rho}_\mu - g_1\sigma\vec{a}_{1\mu} - g_1\phi\vec{a}_{1\mu} - g_1\vec{a}_0 f_{1\mu}\right)^2 \\ &= \quad \cdots - g_1\phi\partial_\mu\eta_N f^{1\mu} - g_1\phi\partial_\mu\vec{\pi}\cdot\vec{a}_1^\mu + \ldots \ . \end{aligned} \tag{3.10}$$

In order to determine vacuum quantities like masses and decays, these mixing terms have to be removed [29]. The bilinear mixing terms can be canceled

by a shift of the fields $f_{1\mu}$ and $\vec{a}_{1\mu}$:

$$\begin{aligned} f_{1\mu} &\to f_{1\mu} + w\partial_\mu \eta_N \ , \\ \vec{a}_{1\mu} &\to \vec{a}_{1\mu} + w\partial_\mu \vec{\pi} \ . \end{aligned} \tag{3.11}$$

The parameter w is to chosen in such a way that all mixing terms vanish.

$$\begin{aligned} &\mathscr{L}_{\text{mix}} \\ &= \left[-g_1\phi + w\left(\phi^2 g_1^2 + m_1^2 + \frac{1}{2}\phi^2 h_1 + \frac{1}{2}\phi^2 h_2 - \frac{1}{2}\phi^2 h_3 \right) \right] \partial_\mu \vec{\pi} \cdot \vec{a}_1^\mu + \dots \ . \end{aligned} \tag{3.12}$$

From the shifted Lagrangian one can read off the condition for which all the mixing terms cancel:

$$w = \frac{g_1\phi}{m_1^2 + g_1^2\phi^2 + \frac{1}{2}\phi^2(h_1 + h_2 + h_3)} \ . \tag{3.13}$$

Care is needed because also the kinetic terms of the pions and η_N are affected by this shift. For example, in the case of the pions it reads:

$$\begin{aligned} &\mathscr{L}_\pi \\ &= \frac{1}{2}\left\{ 1 - 2g_1\phi - w^2\left[g_1^2\phi^2 + m_1^2 + \phi^2(h_1 + h_2 - h_3) \right] \right\} (\partial_\mu \vec{\pi})^2 + \dots \ . \end{aligned} \tag{3.14}$$

The term for η_N looks the same. Both fields have to be renormalized in such a way that for the new fields $\vec{\pi}^{\text{phys}}$ and η^{phys} the canonical form holds:

$$\mathscr{L}_\pi = \frac{1}{2}\left(\partial_\mu \vec{\pi}^{\text{phys}} \right)^2 + \dots \ . \tag{3.15}$$

This leads to a rescaling of the two fields:

$$\vec{\pi} \to Z\vec{\pi}^{\text{phys}} \ , \qquad \eta_N \to Z\eta_N^{\text{phys}} \ . \tag{3.16}$$

The numerical value of the parameter Z can be found in the literature and is $Z = 1.67 \pm 0.2$ [29].

Besides the mesonic quark-antiquark ((pseudo)scalar and (axial-)vector) contributions, also the tetraquark fields are included. This is especially important for a study at nonzero density. In the $N_f = 2$ case there is only one scalar tetraquark state which we denote as χ [114]. The tetraquark is then a scalar field that couples to chirally invariant terms of second order:

$$\mathscr{L}_\chi = \frac{1}{2}\partial_\mu \chi \partial^\mu \chi - \frac{1}{2}m_\chi^2 \chi^2 + g\chi \text{Tr}\left(\Phi^\dagger \Phi \right) \ . \tag{3.17}$$

The last two terms violate dilatation invariance. However, using the same argument as before the dimensionful couplings g and m_χ can be replaced with dimensionless couplings γ and ζ and the dilaton condensate:

$$\begin{aligned} \gamma G\ \chi \mathrm{Tr}\left(\Phi^\dagger\Phi\right) \to \gamma\bar{G}\ \chi \mathrm{Tr}\left(\Phi^\dagger\Phi\right) \equiv g\ \chi \mathrm{Tr}\left(\Phi^\dagger\Phi\right)\ , \\ \zeta G^2\ \chi^2 \to \zeta\bar{G}^2\ \chi^2 \equiv m_\chi^2\ \chi^2\ . \end{aligned} \tag{3.18}$$

Chiral symmetry would also allow a term $\propto \chi^2 \mathrm{Tr}\left(\Phi^\dagger\Phi\right)$, but such a term is suppressed in the large-N_c limit [105]. The spontaneous breaking of chiral symmetry also induces a tetraquark condensate $\bar{\chi}$. Moreover, also a mixing between the scalar states σ and χ arises:

$$\mathscr{L}_{\mathrm{mix}} = -2g\phi\sigma\chi\ . \tag{3.19}$$

The mixing can be removed by an $O(2)$ rotation into two physical states $(\sigma,\chi) = O(H,S)$ [114]. The relation for the masses of H and S read:

$$\begin{aligned} m_H^2 &= m_\chi^2\cos^2\theta + m_\sigma^2\sin^2\theta - 4g\phi\cos\theta\sin\theta \\ &= \frac{1}{2}\left[m_\chi^2 + m_\sigma^2 - \mathrm{sign}(m_\sigma^2 - m_\chi^2)\sqrt{(m_\sigma^2 - m_\chi^2)^2 + (4g\phi)^2}\right]\ , \\ m_S^2 &= m_\chi^2\sin^2\theta + m_\sigma^2\cos^2\theta + 4g\phi\cos\theta\sin\theta \\ &= \frac{1}{2}\left[m_\chi^2 + m_\sigma^2 + \mathrm{sign}(m_\sigma^2 - m_\chi^2)\sqrt{(m_\sigma^2 - m_\chi^2)^2 + (4g\phi)^2}\right]\ , \end{aligned} \tag{3.20}$$

with the mixing angle θ:

$$\theta = \frac{1}{2}\arctan\frac{4g\phi}{m_\sigma^2 - m_\chi^2}\ ; \quad -\frac{\pi}{4} < \theta < \frac{\pi}{4}\ . \tag{3.21}$$

After these steps it is possible to identify the mesons listed in Ref. [10]. The fields $\vec{\pi}$ and η_N correspond to the pion and the nonstrange part of the η meson. The fields ω^μ and $\vec{\rho}^\mu$ represent the vector states $\omega(782)$ and $\rho(770)$, and the fields f_1^μ and $\vec{a}_1^\mu$ the axial-vector mesons $f_1(1285)$ and $a_1(1260)$. The three scalar fields are assigned as: $S \sim f_0(1370)$, $H \sim f_0(500)$ and $\vec{a}_0 \sim a_0(1450)$. The chiral condensate reads $\phi = \langle\sigma\rangle = Zf_\pi = 154.4$ MeV.

3.2 Baryons in the eLSM

A novel aspect of the eLSM is the chiral invariance of the Lagrangian, which is also preserved in the baryon sector at any density and temperature. This is a crucial difference to other hadronic models, as for example the Walecka model which is already not chirally invariant in the vacuum [140]. Two

possible ways to implement chiral symmetry for the baryons are presented: the naive assignment and the mirror assignment. The nucleon and its chiral partner are included into the eLSM by using two baryon doublets.

In both cases the fields are separated into left-handed and right-handed ones by the projection operators P_L and P_R:

$$\psi_{i,R} = P_R\ \psi_i\ , \qquad \psi_{i,L} = P_L\ \psi_i\ , \tag{3.22}$$
$$\bar{\psi}_{i,R} = \bar{\psi}_i\ P_L\ , \qquad \bar{\psi}_{i,L} = \bar{\psi}_i\ P_R\ . \tag{3.23}$$

- **Naive assignment:** In the naive assignment the doublets transform independently under chiral symmetry transformation. In the Lagrangian the (pseudo)scalar as well as the (axial-)vector mesons are coupled independently to the nucleons ψ_1 and ψ_2. Both baryon fields have the same chiral transformation, and the Lagrangian has the form:

$$\begin{aligned}\mathscr{L}_B = &\bar{\psi}_{1,L}\imath\not{D}_{1,L}\psi_{1,L} + \bar{\psi}_{1,R}\imath\not{D}_{1,R}\psi_{1,R} - \hat{g}_1\left(\bar{\psi}_{1,L}\Phi^\dagger\psi_{1,R} + \bar{\psi}_{1,R}\Phi\psi_{1,L}\right)\\ &+ \bar{\psi}_{2,L}\imath\not{D}_{2,L}\psi_{2,L} + \bar{\psi}_{2,R}\imath\not{D}_{2,R}\psi_{2,R} - \hat{g}_2\left(\bar{\psi}_{2,L}\Phi^\dagger\psi_{2,R} + \bar{\psi}_{2,R}\Phi\psi_{2,L}\right)\\ &+ \dots\ ,\end{aligned} \tag{3.24}$$

with the notations for the covariant derivatives:

$$\begin{aligned} D^\mu_{1,R} &= \partial^\mu - \imath c_1 R^\mu\ , \qquad D^\mu_{1,L} = \partial^\mu - \imath c_1 L^\mu\ ,\\ D^\mu_{2,R} &= \partial^\mu - \imath c_2 R^\mu\ , \qquad D^\mu_{2,L} = \partial^\mu - \imath c_2 L^\mu\ . \end{aligned} \tag{3.25}$$

Additional mixing terms of the kind $\bar{\psi}_{1,R}\Phi^\dagger\psi_{2,L} - \bar{\psi}_{1,L}\Phi\psi_{2,R}\dots$ could be introduced but they can be removed [82].

After condensation ($\sigma \to \phi$, $\omega_0 \to \bar{\omega}_0$, all other fields e.g. π and a_1 do not condense) the Lagrangian for the baryons reads:

$$\begin{aligned}\mathscr{L}_B = &\bar{\psi}_1\imath\not{\partial}\psi_1 - g^{(1)}_\omega\bar{\psi}_1\imath\gamma_0\bar{\omega}_0\psi_1 - \frac{1}{2}\hat{g}_1\bar{\psi}_1\phi\psi_1\\ &+ \bar{\psi}_2\imath\not{\partial}\psi_2 - g^{(2)}_\omega\bar{\psi}_2\imath\gamma_0\bar{\omega}_0\psi_2 - \frac{1}{2}\hat{g}_2\bar{\psi}_2\phi\psi_2 + \dots\ .\end{aligned} \tag{3.26}$$

The masses of the baryon fields ψ_1 and ψ_2 correspond to the masses of the nucleon resonances N and N^*, which can be read off directly:

$$\begin{aligned} m_{\psi_1} &= m_N = \frac{1}{2}\hat{g}_1\phi\ ,\\ m_{\psi_2} &= m_{N^*} = \frac{1}{2}\hat{g}_2\phi\ . \end{aligned} \tag{3.27}$$

In the case of restored chiral symmetry ($\phi \to 0$) the masses of N and N^* vanish exactly: $m_N = m_{N^*} = 0$.

- **Mirror assignment:** In contrast to the naive assignment, in the mirror assignment the baryons ψ_1 and ψ_2 are introduced as chiral partners. Under chiral transformation the baryon ψ_2 transforms in a mirror way w.r.t. ψ_1:

$$\begin{aligned} \psi_{1,R} &\to U_R\ \psi_{1,R}\ , & \psi_{1,L} &\to U_L\ \psi_{1,L}\ , \\ \psi_{2,R} &\to U_L\ \psi_{2,R}\ , & \psi_{2,L} &\to U_R\ \psi_{2,L}\ , \\ \bar{\psi}_{1,R} &\to \bar{\psi}_{1,R}\ U_R^\dagger\ , & \bar{\psi}_{1,L} &\to \bar{\psi}_{1,L}\ U_L^\dagger\ , \\ \bar{\psi}_{2,R} &\to \bar{\psi}_{2,R}\ U_L^\dagger\ , & \bar{\psi}_{2,L} &\to \bar{\psi}_{2,L}\ U_R^\dagger\ . \end{aligned} \tag{3.28}$$

Besides the usual terms, the mirror assignment allows for a further chirally invariant term:

$$\begin{aligned} & m_0(\bar{\psi}_2\gamma_5\psi_1 - \bar{\psi}_1\gamma_5\psi_2) \\ = \ & m_0(\bar{\psi}_{2,L}\psi_{1,R} - \bar{\psi}_{2,R}\psi_{1,L} - \bar{\psi}_{1,L}\psi_{2,R} + \bar{\psi}_{1,R}\psi_{2,L})\ , \end{aligned} \tag{3.29}$$

which introduces a chirally invariant mass contribution m_0. The full Lagrangian reads:

$$\begin{aligned} \mathscr{L}_B = & \bar{\psi}_{1,L}\imath\not{D}_{1,L}\psi_{1,L} + \bar{\psi}_{1,R}\imath\not{D}_{1,R}\psi_{1,R} + \bar{\psi}_{2,L}\imath\not{D}_{2,L}\psi_{2,L} + \bar{\psi}_{2,R}\imath\not{D}_{2,R}\psi_{2,R} \\ & - \hat{g}_1\left(\bar{\psi}_{1,L}\Phi\psi_{1,R} + \bar{\psi}_{1,R}\Phi^\dagger\psi_{1,L}\right) - \hat{g}_2\left(\bar{\psi}_{2,L}\Phi^\dagger\psi_{2,R} + \bar{\psi}_{2,R}\Phi\psi_{2,L}\right) \\ & + m_0\left(\bar{\psi}_{2,L}\psi_{1,R} - \bar{\psi}_{2,R}\psi_{1,L} - \bar{\psi}_{1,L}\psi_{2,R} + \bar{\psi}_{1,R}\psi_{2,L}\right)\ . \end{aligned} \tag{3.30}$$

It is evident that the fields ψ_1 and ψ_2 mix and that the chiral eigenstates do not correspond to the mass eigenstates. In order to obtain the physical masses the mass matrix has to be diagonalized:

$$\begin{aligned} & \left(\bar{\psi}_1,\ \bar{\psi}_2\gamma_5\right) M \begin{pmatrix} \psi_1 \\ -\gamma_5\psi_2 \end{pmatrix} \\ = & \left(\bar{\psi}_1,\ \bar{\psi}_2\gamma_5\right) \begin{pmatrix} \frac{1}{2}\hat{g}_1\phi & m_0 \\ m_0 & -\frac{1}{2}\hat{g}_2\phi \end{pmatrix} \begin{pmatrix} \psi_1 \\ -\gamma_5\psi_2 \end{pmatrix}\ . \end{aligned} \tag{3.31}$$

The physical masses of the baryon resonances N and N^* follow from zeros of the polynomial:

$$\det(\lambda\cdot\mathbb{1}_2 - M) = \left(\lambda - \frac{1}{2}\hat{g}_1\phi\right)\left(\lambda + \frac{1}{2}\hat{g}_2\phi\right) - m_0^2 = 0\ , \tag{3.32}$$

and read explicitly:

$$\lambda_1 = m_N = \sqrt{\left(\frac{\hat{g}_1 + \hat{g}_2}{4}\right)^2\phi^2 + m_0^2} + \frac{1}{4}\left(\hat{g}_1 - \hat{g}_2\right)\phi\ , \tag{3.33}$$

$$-\lambda_2 = m_{N^*} = \sqrt{\left(\frac{\hat{g}_1 + \hat{g}_2}{4}\right)^2\phi^2 + m_0^2} - \frac{1}{4}\left(\hat{g}_1 - \hat{g}_2\right)\phi\ . \tag{3.34}$$

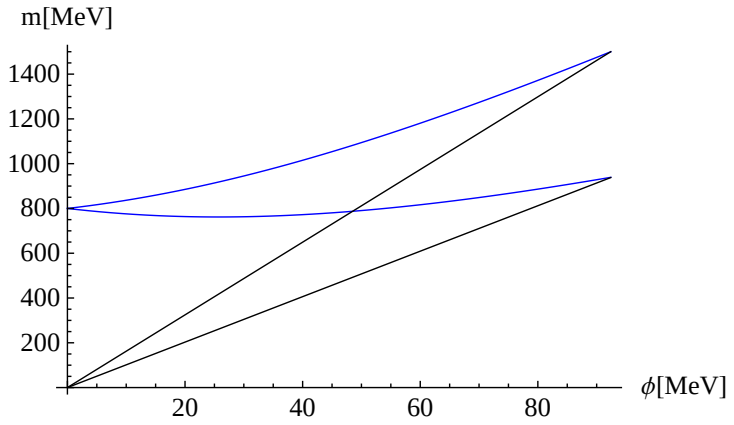

Figure 3.1: Masses of N and N^* as a function of ϕ. Black lines: in the naive assignment the chiral condensate ϕ generates the masses. Blue lines: in the mirror assignment the chiral condensate ϕ is responsible for a mass splitting. For both cases the vacuum masses read $m_N = 0.939$ GeV and $m_{N^*} = 1.5$ GeV. For simplicity the physical point is for $Z = 1$: $\phi = f_\pi$.

The masses in the mirror assignment compared to the masses in the naive assignment as function of ϕ are depicted in Fig. 3.1. The behavior of the masses in the mirror assignment allows for a different interpretation of the origin of the nucleon mass. In the naive assignment (black lines) the chiral condensate ϕ is solely responsible for the mass generation of the nucleon N and its chiral partner N^*. In the case of chiral symmetry restoration, both masses become degenerate and vanish. The masses increase in both cases linearly with ϕ. On the contrary, in the mirror assignment (blue lines) there is a remnant mass m_0. The chiral condensate is not solely responsible for the complete mass generation of the nucleons, but for a mass splitting of N and N^*:

$$m_N - m_{N^*} = \frac{1}{2}(\hat{g}_1 - \hat{g}_2)\phi \ . \tag{3.35}$$

For vanishing ϕ the mass of the nucleon N becomes degenerate with the mass of N^*:

$$m_N = m_{N^*} = m_0 \ . \tag{3.36}$$

Also, the dependence of the mass on the condensate ϕ is not linear.

In order to preserve chiral symmetry and dilatation invariance, the constant m_0 is identified with scalar fields such as the tetraquark field χ and/

or the dilaton field G:

$$m_0 = a < \chi > + b < G >= a\bar{\chi} + b\bar{G} \ . \tag{3.37}$$

For the sake of simplicity the dilaton is neglected here and only the tetraquark state is retained (to be identified with the light scalar state $f_0(500)$). The full dilatation invariant baryonic Lagrangian is given by:

$$\begin{aligned}\mathscr{L}_B = & \bar{\psi}_{1,L} i \not{D}_{1,L} \psi_{1,L} + \bar{\psi}_{1,R} i \not{D}_{1,R} \psi_{1,R} + \bar{\psi}_{2,L} i \not{D}_{2,L} \psi_{2,L} + \bar{\psi}_{2,R} i \not{D}_{2,R} \psi_{2,R} \\ & - \hat{g}_1 \left(\bar{\psi}_{1,L} \Phi \psi_{1,R} + \bar{\psi}_{1,R} \Phi^\dagger \psi_{1,L} \right) - \hat{g}_2 \left(\bar{\psi}_{2,L} \Phi^\dagger \psi_{2,R} + \bar{\psi}_{2,R} \Phi \psi_{2,L} \right) \\ & + a\chi \left(\bar{\psi}_{2,L} \psi_{1,R} - \bar{\psi}_{2,R} \psi_{1,L} - \bar{\psi}_{1,L} \psi_{2,R} + \bar{\psi}_{1,R} \psi_{2,L} \right) \ . \end{aligned} \tag{3.38}$$

Notice that by setting the coupling a to zero the Lagrangian in the naive assignment is obtained (but the fields ψ_1 and ψ_2 still transform in a mirror way).

3.3 CDW in the eLSM with m_0 = const. and without axial-vector mesons

The first nonzero-density study is performed in a simplified version of the eLSM. Chiral symmetry is reduced to an $O(4)$ symmetry and in the (axial-)vector-sector only the ω-meson is included. In this case there is no shift of the axial-vector mesons (the wave-function renormalization results in $Z = 1$). In addition, m_0 is treated as a constant and therefore the scalar resonances do not mix. Although the eLSM is simplified, it is still possible to describe nuclear matter ground-state properties in the mean-field approximation [86, 138].

The remaining mesonic Lagrangian contains only those fields that will eventually condense in a mean-field study (σ, ω^μ, π_3):

$$\begin{aligned}\mathcal{L}_{\text{mes}} = & \frac{1}{2} \partial_\mu \sigma \partial^\mu \sigma + \frac{1}{2} \partial_\mu \pi_3 \partial^\mu \pi_3 - \frac{1}{4} (\partial_\mu \omega_\nu - \partial_\nu \omega_\mu)^2 \\ & + \frac{1}{2} m^2 (\sigma^2 + \pi_3^2) + \frac{1}{2} m_\omega^2 \omega_\mu \omega^\mu - \frac{\lambda}{4} (\sigma^2 + \pi_3^2)^2 + \varepsilon \sigma \ . \end{aligned} \tag{3.39}$$

The baryon Lagrangian reduces to:

$$\begin{aligned}\mathcal{L}_{\text{bar}} = & \overline{\Psi}_1 i \gamma_\mu \partial^\mu \Psi_1 + \overline{\Psi}_2 i \gamma_\mu \partial^\mu \Psi_2 \\ & - \frac{\widehat{g}_1}{2} \overline{\Psi}_1 (\sigma + i \gamma_5 \tau^3 \pi_3) \Psi_1 - \frac{\widehat{g}_2}{2} \overline{\Psi}_2 (\sigma - i \gamma_5 \tau^3 \pi_3) \Psi_2 \\ & - g_\omega \overline{\Psi}_1 i \gamma_\mu \omega^\mu \Psi_1 - g_\omega \overline{\Psi}_2 i \gamma_\mu \omega^\mu \Psi_2 - m_0 (\overline{\Psi}_2 \gamma_5 \Psi_1 - \overline{\Psi}_1 \gamma_5 \Psi_2) \ . \end{aligned}$$

Since ω_0 is proportional to the γ_0 matrix, it forms a condensate at nonzero baryon chemical potential μ, which we denote as $\langle\omega_0\rangle = \bar{\omega}_0$.

The Ansatz of a chiral density wave (CDW) assumes a periodic structure for σ as well as for the neutral pion π_3:

$$\langle\sigma(z)\rangle = \phi\cos(2fz)\ , \qquad \langle\pi_3(z)\rangle = \phi\sin(2fz)\ , \tag{3.40}$$

where ϕ is the amplitude and f the wave vector of the CDW. This Ansatz has many consequences. In the mesonic part, two additional contributions arise: one contribution stems from the kinetic term of the fields σ and π_3. This contribution is positive and does not favor the formation of a CDW. Another contribution comes from the explicit symmetry breaking term, which also suppresses the formation of an inhomogeneous condensation. All other mesonic contributions remain the same as in the case with homogeneous condensation, since only chirally invariant bilinear terms of the kind $\sigma^2+\pi_3^2$ are present. The contributions can be summarized as:

$$\begin{aligned}(\partial_\mu\sigma)^2 + (\partial_\mu\pi_3)^2 &\longrightarrow (2f\phi\sin(2fz))^2 + (2f\phi\cos(2fz))^2 = 4f^2\phi^2\ ,\\ \sigma^2+\pi_3^2 &\longrightarrow (\phi\cos(2fz))^2 + (\phi\sin(2fz))^2 = \phi^2\ ,\\ \varepsilon\sigma &\longrightarrow \varepsilon\phi\cos(2fz)\ .\end{aligned} \tag{3.41}$$

Notice that, in a spatial volume $V > (\pi/f)^3$, the spatially dependent term $\sim\cos(2fz)$ averages to zero for any nonzero value of f. Finally the resulting mean-field potential reads:

$$U_{\text{mes}}^{\text{mean-field}} = 2f^2\phi^2 - \frac{1}{2}m_\omega^2\bar{\omega}_0^2 + \frac{\lambda}{4}\phi^4 - \frac{1}{2}m^2\phi^2 - \varepsilon\phi\cos(2fz)\ . \tag{3.42}$$

The CDW leads also to space-dependent baryonic terms:

$$\begin{aligned}&\hat{g}_1\phi\bar{\psi}_1\left[\cos(2fz) + \imath\gamma_5\tau_3\sin(2fz)\right]\psi_1 + \hat{g}_2\phi\bar{\psi}_2\left[\cos(2fz) - \imath\gamma_5\tau_3\sin(2fz)\right]\psi_2\\ =&\hat{g}_1\phi\bar{\psi}_1\exp\left(+\imath2\gamma_5\tau_3 fz\right)\psi_1 + \hat{g}_2\phi\bar{\psi}_2\exp\left(-\imath2\gamma_5\tau_3 fz\right)\psi_2\ .\end{aligned} \tag{3.43}$$

However, there is a neat transformation which changes the space dependence into a momentum dependence:

$$\begin{aligned}\psi_1 &\to \exp[-\imath\gamma_5\tau_3 fz]\psi_1\ , \qquad & \bar{\psi}_1 &\to \bar{\psi}_1\exp[-\imath\gamma_5\tau_3 fz]\ ,\\ \psi_2 &\to \exp[+\imath\gamma_5\tau_3 fz]\psi_2\ , \qquad & \bar{\psi}_2 &\to \bar{\psi}_2\exp[+\imath\gamma_5\tau_3 fz]\ .\end{aligned} \tag{3.44}$$

This transformation is applied to all bilinear terms and leads to the following changes. The interaction between (pseudo-)scalar mesons and baryons reads:

$$\begin{aligned}\bar{\psi}_1\exp[+\imath\gamma_5\tau_3 2fz]\psi_1 &\to \bar{\psi}_1\psi_1\ ,\\ \bar{\psi}_2\exp[-\imath\gamma_5\tau_3 2fz]\psi_2 &\to \bar{\psi}_2\psi_2\ .\end{aligned} \tag{3.45}$$

For the bilinear terms that include γ_μ we use the relation $\gamma_\mu \exp(+\imath\gamma_5 a) = \exp(-\imath\gamma_5 a)\gamma_\mu$. The transformations in eq. (3.44) leave the terms invariant:

$$\begin{aligned}
\bar{\psi}_1\gamma_\mu\psi_1 &\to \bar{\psi}_1 \exp[-\imath\gamma_5\tau_3 f z]\gamma_\mu \exp[-\imath\gamma_5\tau_3 f z]\psi_1 = \bar{\psi}_1\gamma_\mu\psi_1 \ , \\
\bar{\psi}_2\gamma_\mu\psi_2 &\to \bar{\psi}_2 \exp[+\imath\gamma_5\tau_3 f z]\gamma_\mu \exp[+\imath\gamma_5\tau_3 f z]\psi_2 = \bar{\psi}_2\gamma_\mu\psi_2 \ . \qquad (3.46)
\end{aligned}$$

The additional baryon mass contribution (m_0-term) is invariant as well:

$$\begin{aligned}
\bar{\psi}_2\gamma_5\psi_1 &\to \bar{\psi}_2 \exp[+\imath\gamma_5\tau_3 f z]\gamma_5 \exp[-\imath\gamma_5\tau_3 f z]\psi_1 = \bar{\psi}_2\gamma_5\psi_1 \ , \\
\bar{\psi}_1\gamma_5\psi_2 &\to \bar{\psi}_1 \exp[-\imath\gamma_5\tau_3 f z]\gamma_5 \exp[+\imath\gamma_5\tau_3 f z]\psi_2 = \bar{\psi}_1\gamma_5\psi_2 \ . \qquad (3.47)
\end{aligned}$$

For all the terms shown above the transformation of eq. (3.44) is a great simplification. However, it is the kinetic term that gives rise to the aforementioned momentum-dependent structure:

$$\begin{aligned}
\bar{\psi}_1\imath\partial\!\!\!/\psi_1 \to& \bar{\psi}_1 \exp[-\imath\gamma_5\tau_3 f z]\imath \left(\partial\!\!\!/ \exp[-\imath\gamma_5\tau_3 f z]\psi_1\right) \\
=& \bar{\psi}_1 \exp[-\imath\gamma_5\tau_3 f z]\imath\gamma_\mu \exp[-\imath\gamma_5\tau_3 f z] \left(\partial^\mu\psi_1\right) \\
&+ \bar{\psi}_1 \exp[-\imath\gamma_5\tau_3 f z]\imath\gamma_\mu \left(\partial^\mu \exp[-\imath\gamma_5\tau_3 f z]\right)\psi_1 \\
=& \bar{\psi}_1\imath\partial\!\!\!/\psi_1 + \bar{\psi}_1\gamma_1\gamma_5\tau_3 f\psi_1 \ , \\
\bar{\psi}_2\imath\partial\!\!\!/\psi_2 \to& \bar{\psi}_2 \exp[+\imath\gamma_5\tau_3 f z]\imath \left(\partial\!\!\!/ \exp[+\imath\gamma_5\tau_3 f z]\psi_2\right) \\
=& \bar{\psi}_2 \exp[+\imath\gamma_5\tau_3 f z]\imath\gamma_\mu \exp[+\imath\gamma_5\tau_3 f z] \left(\partial^\mu\psi_2\right) \\
&+ \bar{\psi}_2 \exp[+\imath\gamma_5\tau_3 f z]\imath\gamma_\mu \left(\partial^\mu \exp[+\imath\gamma_5\tau_3 f z]\right)\psi_2 \\
=& \bar{\psi}_2\imath\partial\!\!\!/\psi_2 - \bar{\psi}_2\gamma_1\gamma_5\tau_3 f\psi_2 \ . \qquad (3.48)
\end{aligned}$$

The additional terms still allow to calculate the energy eigenvalues in an analytic way but for our study a numerical treatment is used. The quadratic form of the Lagrangian in a matrix form is:

$$\begin{aligned}
&\mathscr{L}_B \\
&= \left(\bar{\psi}_1, \bar{\psi}_2\gamma_5\right) \begin{pmatrix} \imath\partial\!\!\!/ + \gamma_1\gamma_5\tau_3 f - \frac{1}{2}\hat{g}_1\phi & m_0 \\ m_0 & \imath\partial\!\!\!/ - \gamma_1\gamma_5\tau_3 f + \frac{1}{2}\hat{g}_2\phi \end{pmatrix} \begin{pmatrix} \psi_1 \\ -\gamma_5\psi_2 \end{pmatrix} \\
&= \left(\bar{\psi}_1, \bar{\psi}_2\gamma_5\right) Q \begin{pmatrix} \psi_1 \\ -\gamma_5\psi_2 \end{pmatrix} \ , \qquad (3.49)
\end{aligned}$$

where the contribution $-\imath g_\omega\bar{\omega}_0$ is not displayed since it is absorbed in a shift of the baryon chemical potential $\mu^* = \mu - g_\omega\bar{\omega}_0$. The condensation of ω_0 takes place at nonzero chemical potential μ. The energy eigenvalues are calculated as numerical solutions of the characteristic polynomial (see Appendix A for details). As a first result a level splitting in the inhomogeneous regime is observed. The energy levels have the form:

$$E_k(p_x, p_y, p_z) = \sqrt{p_x^2 + p_y^2 + p_z^2 + m_k(p_z)^2} \equiv E_k(p_z) \ , \qquad (3.50)$$

with $k = 1, 2, 3, 4$. In the absence of the CDW the energy eigenvalues reduce to:

$$E_1 = E_2 = E_N = \sqrt{p_x^2 + p_y^2 + p_z^2 + m_N^2} \ ,$$
$$E_3 = E_4 = E_{N^*} = \sqrt{p_x^2 + p_y^2 + p_z^2 + m_{N^*}^2} \ . \tag{3.51}$$

In order to calculate the grand canonical potential, the mean-field approximation is applied [138, 141]:

$$\begin{aligned} U_{\text{eff}}(\phi, \bar{\omega}_0, f) &= U_{\text{mes}}^{\text{mean-field}} + \sum_{k=1}^{4} \int \frac{2d^3p}{(2\pi)^3} [E_k(p_z) - \mu^*] \Theta[\mu^* - E_k(p_z)] \\ &= 2f^2\phi^2 + \frac{1}{4}\lambda\phi^4 - \frac{1}{2}m^2\phi^2 - \varepsilon\phi\Theta(f) - \frac{1}{2}m_\omega^2\bar{\omega}_0^2 \\ &+ \sum_{k=1}^{4} \int_{-\infty}^{\infty} \frac{dp_z}{(2\pi)^2} \left[\mu^* \sqrt{p_z^2 + m_k(p_z)^2}^2 - \frac{(\mu^*)^3}{3} \right. \\ &\left. - \frac{2}{3}\sqrt{p_z^2 + m_k(p_z)^2}^3 \right] \Theta\left(\mu^* - \sqrt{p_z^2 + m_k(p_z)^2}\right) \ , \end{aligned} \tag{3.52}$$

where $\mu^* = \mu - g_\omega\bar{\omega}_0$ is the shifted baryon chemical potential. The thermodynamical behavior follows from the extrema in $\bar{\omega}_0$ and the absolute minimum in ϕ and f:

$$\begin{aligned} 0 &\stackrel{!}{=} \frac{\partial U_{\text{eff}}}{\partial \phi} \ , \\ 0 &\stackrel{!}{=} \frac{\partial U_{\text{eff}}}{\partial \bar{\omega}_0} \ , \\ 0 &\stackrel{!}{=} \frac{\partial U_{\text{eff}}}{\partial f} \ . \end{aligned} \tag{3.53}$$

The numerical solution of these equations will be discussed in the next section.

As a concluding part of this section we discuss a rather subtle issue. The transformation of the fermions could (at least in certain models) leads to an additional contribution in the potential $\propto f^2$ [142]. Such a term is unphysical and has to be subtracted. However, in our approach this is not the case. Following studies of the NJL model such a term is independent of ϕ [142]. For that reason we consider the case $\phi = 0$. The meson potential $U_{\text{meson}}^{\text{mean-field}}$ reduces to:

$$U_{\text{mes}}^{\text{mean-field}} = -\frac{1}{2}m_\omega^2\bar{\omega}_0^2 \ , \tag{3.54}$$

thus leading to the effective potential:

$$U_{\text{eff}}(\phi=0,\bar{\omega}_0,f)=\sum_{k=1}^{4}\int\frac{2d^3p}{(2\pi)^3}[E_k(p_z)-\mu^*]\Theta[\mu^*-E_k(p_z)]+U_{\text{mes}}^{\text{mean-field}}\ . \tag{3.55}$$

In the case $\phi=0$ the four energy levels can be calculated analytically even for finite f. As a result only two degenerate energy levels emerge:

$$\begin{aligned}E_1=&E_2=\sqrt{(p_x-f)^2+p_y^2+p_z^2+m_0^2}\ ,\\ E_3=&E_4=\sqrt{(p_x+f)^2+p_y^2+p_z^2+m_0^2}\ .\end{aligned} \tag{3.56}$$

The remaining f-dependence can be removed by two shifts: $p_z\to p_z'+f$ and $p_z\to p_z'-f$. Thus, only one energy level, which is independent of f, remains:

$$E_1=E_2=E_3=E_4=\sqrt{p_x^2+p_y^2+p_z^2+m_0^2}\ . \tag{3.57}$$

As a result the effective potential U_{eff} is independent of f for the case $\phi=0$ at any μ^*. In the mean-field theory no unphysical potential $\propto f^2$ arises for $\phi=0$ and for nonzero ϕ a numerical study shows that U_{eff} is bounded from below in the variable f.

3.4 Nonzero-density study of the eLSM with $m_0=$ const.

In order to understand the behavior at nonzero chemical potential μ two distinct choices for the mass of the chiral partner of the nucleon are considered: $m_{N^*}=1200$ MeV and $m_{N^*}=1500$ MeV. In addition the parameter m_0 is varied following the discussion of Ref. [86]. The parameters λ, m and ε are:

$$\begin{aligned}\lambda&=\frac{1}{2f_\pi}\left(m_\sigma^2-m_\pi^2\right)\ ,\\ m&=\sqrt{\frac{1}{2}\left(m_\sigma^2-3m_\pi^2\right)}\ ,\\ \varepsilon&=m_\pi^2 f\pi\ .\end{aligned} \tag{3.58}$$

The numerical values read $f_\pi=\phi_0=92.4$ MeV, $m_\pi=134.9$ MeV ($\varepsilon=(118.9\text{ MeV})^3$), $m_N=939$ MeV and $m_\omega=783$ MeV. The chirally invariant mass contribution to the nucleon is tuned between $m_0=600$ MeV and $m_0=$

800 MeV. These six values determine the parameters (m_σ, λ, $\hat{g}_1$, $\hat{g}_2$, g_ω, and m) in order to obtain nuclear saturation at $\mu = 923$ MeV ($\rho = \rho_0$, binding energy -16 MeV):

m_{N^*}	1200 MeV		
m_0	600.0 MeV	700.0 MeV	800.0 MeV
m_σ	423.6 MeV	375.6 MeV	303.0 MeV
λ	9.393	7.146	4.263
$\hat{g}_1$	16.30	14.68	12.54
$\hat{g}_2$	21.80	20.33	18.19
g_ω	11.23	8.811	5.989
m	247.3 MeV	204.9 MeV	131.7 MeV
ϕ	33.68 MeV	42.25 MeV	49.19 MeV
$\bar{\omega}_0$	21.26 MeV	16.67 MeV	11.33 MeV

m_{N^*}	1500 MeV		
m_0	600.0 MeV	700.0 MeV	800.0 MeV
m_σ	447.5 MeV	410.4 MeV	356.4 MeV
m	266.8 MeV	235.0 MeV	185.8 MeV
λ	10.60	8.733	6.306
g_ω	11.54	9.277	6.766
$\hat{g}_1$	16.90	15.54	13.85
$\hat{g}_2$	29.10	27.69	25.99
ϕ	36.02 MeV	44.77 MeV	52.17 MeV
$\bar{\omega}_0$	21.83 MeV	17.55 MeV	12.80 MeV

At $\mu = 923$ MeV the values for the condensates of the fields σ and ω_0 are ϕ and $\bar{\omega}_0$.

These parameters lead to the nonzero-density behavior displayed in Fig. 3.2. For all cases a phase transition to homogeneous nuclear matter at $\mu = 923$ MeV is found. All six cases share a small regime of homogeneous nuclear matter. The transition to the CDW phase depends on an interplay of m_0 and m_{N^*}. In general, a large m_0 leads to a transition at high μ. The CDW state shows only a small dependence on μ: ϕ remains almost flat and starts to increase only for high μ. Conversely, in the homogeneous phase the chiral condensate shows a strong dependence on μ and reduces significantly with increasing μ. With inhomogeneous condensation the transition to a restored chirally symmetric phase does not take place [86]. Instead, the inhomogeneous phase is realized. The intermediate homogeneous phase is not present in the chiral limit as it will be discussed in the next paragraph. For a reasonable choice of parameters no homogeneous nuclear matter ground state is found.

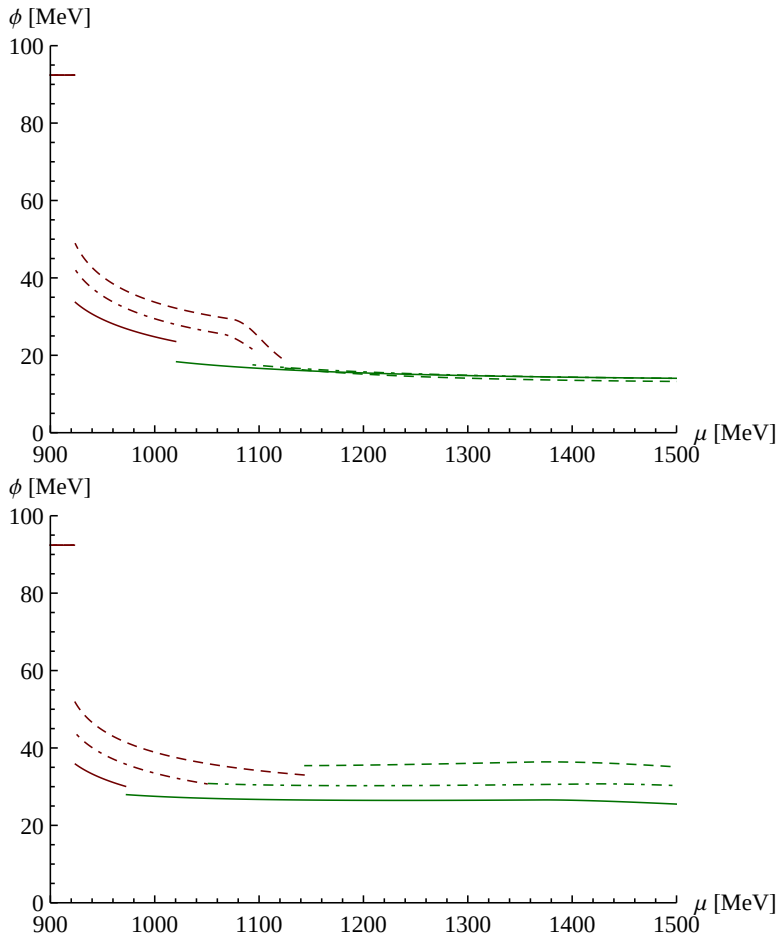

Figure 3.2: The condensate ϕ as a function of the baryon chemical potential μ. Red color indicates a homogeneous phase and green color an inhomogeneous (CDW) phase. The mass of the chiral partner of the nucleon is $m_{N^*} = 1.2$ GeV for the upper and $m_{N^*} = 1.5$ GeV for the lower plot. Dashed curves correspond to $m_0 = 0.8$ GeV, dash-dotted to $m_0 = 0.7$ GeV, and straight to $m_0 = 0.6$ GeV.

The effect of explicit chiral symmetry breaking can easily be understood when looking at the effective potential U_{eff} in the chiral limit at different baryon chemical potentials μ. In the chiral limit there is a 1st order transition from the vacuum to a CDW state. In Fig. 3.3 and Fig. 3.4 the potentials at four different values of μ are shown. The potential is plotted as a function of ϕ at the extrema of $\bar{\omega}_0$ and f. The left-hand side of Fig. 3.3 shows the case in the vacuum, with $\mu = 800$ MeV. The solution for homogeneous condensation coincides with the solution based on the CDW because $f = 0$ for all ϕ. The absolute minimum at $\phi = f_\pi$ corresponds to the vacuum. On the right-hand side, $\mu = 900$ MeV, the system is still in the vacuum but the effect of the CDW is visible. There are local minimum at $\phi \sim 40$ MeV that correspond to homogeneous condensation and to the CDW.

In Fig. 3.4 two cases for $\mu > 923$ MeV are shown. In the left panel $\mu = 950$ MeV and the homogeneous absolute minimum (that would allow for a homogeneous ground state) is replaced by the CDW absolute minimum. In the right panel $\mu = 1500$ MeV and chiral symmetry would be restored if only homogeneous condensation were taken into account. However, the CDW prevents chiral symmetry restoration and even for higher μ the CDW remains the ground state. The four plots also show that the CDW, as expected, does not modify the potential at $\phi = 0$. Also, the overall behavior does not depend on the precise choice of the parameters.

In the chiral limit the CDW replaces the homogeneous minimum that is not associated with the vacuum. Comparing this result with the aforementioned findings it is clear that the explicit symmetry breaking is important in order to obtain homogeneous nuclear matter. The explicit symmetry breaking term tilts the potential and lowers the local homogeneous minimum to an absolute minimum. Notice that, as we will see in the next section, this is not the case in the eLSM where the explicit symmetry breaking only plays a minor role and homogeneous nuclear matter is also found in the chiral limit.

3.5 CDW in the eLSM with a light tetraquark

The eLSM is studied at nonzero density including a light tetraquark field. This allows us to connect results of vacuum physics with properties of dense nuclear matter. The results of the previous section allow for a straightforward calculation. Considering the relevant degrees of freedom of the eLSM and keeping only terms involving fields which will eventually condense, i.e., σ, π_3, ω_μ, and χ, leads to the effective potential of the mesonic Lagrangian in the

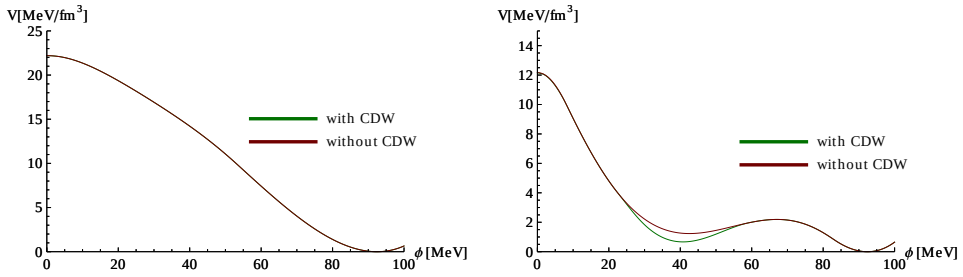

Figure 3.3: The potential U_{eff} as function of ϕ at the extrema of the other dynamical variables. Left-hand side $\mu = 800$ MeV, right-hand side $\mu = 900$ MeV. On the right-hand side there is a further local minimum that corresponds to the CDW.

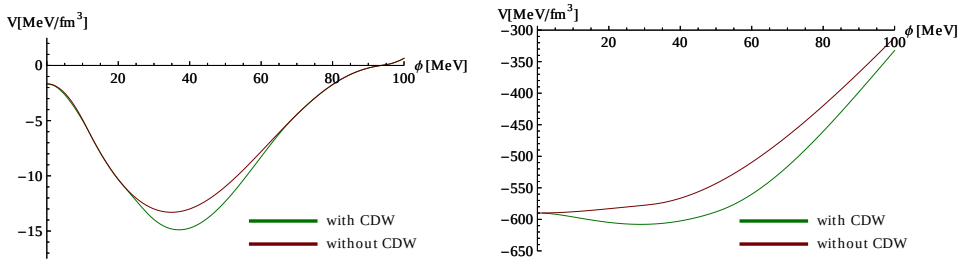

Figure 3.4: The potential U_{eff} as function of ϕ at the extrema of the other dynamical variables. Left-hand side $\mu = 950$ MeV, right-hand side $\mu = 1500$ MeV. The CDW is the new ground state. A homogeneous phase is not possible for intermediate and high μ.

mean-field approximation [139, 141]:

$$\begin{aligned} U_{\text{mes}}^{\text{mean-field}} &= 2f^2\phi^2 + \frac{\lambda}{4}\phi^4 - \frac{1}{2}m^2\phi^2 - \varepsilon\phi\cos(2fz) \\ &\quad - \frac{1}{2}m_\omega^2\bar{\omega}_0^2 + \frac{1}{2}m_\chi^2\bar{\chi}^2 - g\bar{\chi}\phi^2 \ . \end{aligned} \tag{3.59}$$

The relevant baryon Lagrangian in which only the mesons σ, π_3, ω_μ, and χ are retained reads:

$$\begin{aligned} \mathcal{L}_{\text{bar}} =& \overline{\Psi}_1 \imath\gamma_\mu\partial^\mu\Psi_1 + \overline{\Psi}_2\imath\gamma_\mu\partial^\mu\Psi_2 - g_\omega\overline{\Psi}_1\imath\gamma_\mu\omega^\mu\Psi_1 - g_\omega\overline{\Psi}_2\imath\gamma_\mu\omega^\mu\Psi_2 \\ &- \frac{\widehat{g}_1}{2}\overline{\Psi}_1(\sigma + \imath\gamma_5\tau^3\pi_3)\Psi_1 - \frac{\widehat{g}_2}{2}\overline{\Psi}_2(\sigma - \imath\gamma_5\tau^3\pi_3)\Psi_2 \\ &- a\chi(\overline{\Psi}_2\gamma_5\Psi_1 - \overline{\Psi}_1\gamma_5\Psi_2) \ . \end{aligned} \tag{3.60}$$

Following the steps of the previous section leads to the full effective potential:

$$U_{\text{eff}}(\phi, \bar{\chi}, \bar{\omega}_0, f) = \sum_{k=1}^{4}\int\frac{2d^3p}{(2\pi)^3}[E_k(p) - \mu^*]\Theta[\mu^* - E_k(p)] + U_{\text{mes}}^{\text{mean-field}} \ , \tag{3.61}$$

where $\mu^* = \mu - g_\omega\bar{\omega}_0$ and $E_k(p) = \sqrt{p^2 + m_k(p_z)^2}$. Again, in the case of homogeneous condensation there are only two (two-fold degenerate) energy eigenstates, corresponding to the nucleon and its chiral partner, while for inhomogeneous condensation the degeneracy is lifted and four different energy eigenstates emerge. The values for $E_k(p)$ are calculated numerically as solutions of a characteristic polynomial (Appendix [A]). In order to obtain the dynamical behavior at nonzero μ four gap equations (instead of three as in the previous section) have to be solved simultaneously:

$$\begin{aligned} 0 &\stackrel{!}{=} \frac{\partial U_{\text{eff}}}{\partial\phi} \ , \\ 0 &\stackrel{!}{=} \frac{\partial U_{\text{eff}}}{\partial\bar{\omega}_0} \ , \\ 0 &\stackrel{!}{=} \frac{\partial U_{\text{eff}}}{\partial\bar{\chi}} \ , \\ 0 &\stackrel{!}{=} \frac{\partial U_{\text{eff}}}{\partial f} \ . \end{aligned} \tag{3.62}$$

The Tables 3.1-3.3 display the parameter sets used to calculate nuclear matter properties. The parameters are fitted following the procedure in the previous section. In addition the tetraquark state is included and, as a consequence a mixing in the scalar sector arises. The predominantly quarkonium

resonance $f_0(1300)$ is assigned to the heavy scalar state $m_S = 1300$ MeV and $f_0(500)$ with the light predominately tetraquark state $m_H = 600$ MeV [80, 114].

For the mass of the chiral partner of the nucleon, there are now three candidates that will be considered $m_{N^*} = 1200, 1500$, and 1650 MeV. A state with the mass $m_{N^*} = 1200$ MeV has not been seen experimentally yet, but has been suggested in Ref. [86]. The other two states are the well established resonances $N^*(1535)$ and $N^*(1650)$. For each case the parameter m_0 is varied in steps of 50 MeV from $m_0 = 400$ MeV to $m_0 = 700$ MeV, a range which is in agreement with Ref. [82]. The rest of the parameters are determined by vacuum masses, the pion decay constant and matched to nuclear matter conditions [91].

To fix the parameters a system of seven coupled equations has to be solved: eqs. (3.62), eqs. (3.20), and the nuclear matter ground-state conditions ($E/n_B = 923$ MeV and $n_B = 0.16$ fm^{-3}). These equations are used to fix the parameters m_σ, m_χ, g_ω, and g, as well as to determine ϕ_n, $\bar{\omega}_0$, and $\bar{\chi}$ in the nuclear matter ground state. Subsequently the other parameters follow directly from vacuum considerations. As a last step the compressibility K is calculated:

$$K = 9\frac{\partial P}{\partial \rho}|_{\rho=\rho_0} \ . \tag{3.63}$$

It follows that for a broad range of parameters the value for K is consistent with the range $200 - 300$ MeV given in Ref. [143, 144, 145]. For increasing m_0 also K increases; in addition a light m_{N^*} implies a smaller K than a large m_{N^*}. The parameters in Tables 3.1-3.3 can be divided into two groups: one type remains almost unaffected by changing m_0 and another type varies strongly with m_0. Within 10% the values m_σ, m_χ, m, and λ as well as ϕ_n are unchanged when changing m_0 from 400 MeV to 700 MeV. The other parameters g, g_ω, and a, as well as $\bar{\chi}$, $\bar{\omega}_0$, and K change in the same order that m_0 changes.

We turn our attention to a detailed study of the case in which the chiral partner of the nucleon has the mass $m_{N^*} = 1500$ MeV and the chirally invariant nucleon mass parameter is $m_0 = 500$ MeV (Table 3.2, column 3). In Fig. 3.5 we show the effective potential as a function of ϕ for the chemical potential $\mu = 923$ MeV, which corresponds to the nuclear matter ground state. The effective potential is numerically minimized with respect to $\bar{\chi}$ and f and maximized with respect to $\bar{\omega}_0$, respectively. There are two degenerate global minima, one for $\phi = Zf_\pi = 154.3$ MeV, corresponding to the vacuum, and one for $\phi = 149.5$ MeV, corresponding to the nuclear matter ground state. The difference in the chiral condensate compared to the vac-

m_{N^*}	1200.0						
m_0	400.00	450.00	500.00	550.00	600.00	650.00	700.00
m_σ	1297.2	1295.3	1292.7	1289.1	1284.3	1277.6	1268.3
m_χ	606.04	610.04	615.56	623.00	632.93	646.23	664.39
m	904.43	898.43	890.27	879.50	865.51	847.46	823.96
g	318.12	409.99	510.21	620.05	741.40	877.27	1033.1
g_ω	4.2002	4.8782	5.5031	6.0981	6.6794	7.2607	7.8561
λ	35.192	35.089	34.947	34.754	34.492	34.135	33.635
a	19.395	17.155	15.595	14.459	13.616	12.995	12.561
$\hat{g}_1$	11.165	10.884	10.563	10.197	9.7836	9.3166	8.7889
$\hat{g}_2$	14.547	14.267	13.945	13.580	13.166	12.699	12.172
ϕ_n	149.77	149.56	149.30	148.97	148.56	148.03	147.33
$\bar{\chi}$	8.9000	12.806	17.055	21.532	26.116	30.663	34.996
$\bar{\omega}_0$	7.9472	9.2301	10.412	11.538	12.638	13.738	14.864
K	158.05	189.15	215.63	239.02	260.39	280.60	300.46

Table 3.1: The quantities m_{N^*}, m_0, m_σ, m_χ, m, and g have dimension MeV. The couplings g_ω, λ, a, $\hat{g}_1$, and $\hat{g}_2$ are dimensionless. The resulting ϕ_n, $\bar{\chi}$, $\bar{\omega}_0$, and K again have dimension MeV.

m_{N^*}	1500.0						
m_0	400.00	450.00	500.00	550.00	600.00	650.00	700.00
m_σ	1297.9	1296.5	1294.5	1291.8	1288.1	1283.2	1276.6
m_χ	604.47	607.56	611.82	617.54	625.11	635.08	648.32
m	906.81	902.15	895.79	887.38	876.49	862.55	844.69
g	273.61	355.73	444.75	541.67	647.78	765.06	896.70
g_ω	3.8088	4.4789	5.0831	5.6472	6.1871	6.7149	7.2410
λ	35.231	35.153	35.044	34.896	34.699	34.435	34.078
a	22.434	19.611	17.673	16.262	15.201	14.391	13.780
$\hat{g}_1$	11.296	11.055	10.781	10.472	10.125	9.7381	9.3072
$\hat{g}_2$	18.567	18.326	18.052	17.743	17.396	17.009	16.578
ϕ_n	149.86	149.69	149.48	149.22	149.89	148.48	147.97
$\bar{\chi}$	7.0733	10.525	14.345	18.446	22.739	27.127	31.495
$\bar{\omega}_0$	7.2067	8.4746	9.6178	10.685	11.707	12.705	13.701
K	138.66	170.44	197.02	220.00	240.45	259.18	276.85

Table 3.2: The quantities m_{N^*}, m_0, m_σ, m_χ, m, and g have dimension MeV. The couplings g_ω, λ, a, $\hat{g}_1$, and $\hat{g}_2$ are dimensionless. The resulting ϕ_n, $\bar{\chi}$, $\bar{\omega}_0$, and K again have dimension MeV.

m_{N^*}	1650.0						
m_0	400.00	450.00	500.00	550.00	600.00	650.00	700.00
m_σ	1298.2	1296.9	1295.1	1292.7	1289.5	1285.3	1279.5
m_χ	603.88	606.63	610.41	615.49	622.19	630.96	642.48
m	907.71	903.55	897.88	890.37	880.66	868.26	852.47
g	254.92	333.05	417.48	509.12	609.07	718.96	841.31
g_ω	3.6316	4.3019	4.9003	5.4543	5.9804	6.4904	6.9939
λ	35.246	35.177	35.080	34.950	34.775	34.544	34.236
a	24.032	20.882	18.741	17.188	16.016	15.116	14.424
$\hat{g}_1$	11.350	11.124	10.868	10.581	10.259	9.9020	9.5058
$\hat{g}_2$	20.565	20.339	20.084	19.796	19.475	19.117	18.721
ϕ_n	149.89	149.74	149.55	149.31	149.02	148.65	148.20
$\bar{\chi}$	6.3208	9.5705	13.194	17.112	21.246	25.512	29.816
$\bar{\omega}_0$	6.8713	8.1396	9.2719	10.320	11.316	12.281	13.233
K	129.77	162.01	188.82	211.80	232.08	250.45	267.53

Table 3.3: The quantities m_{N^*}, m_0, m_σ, m_χ, m, and g have dimension MeV. The couplings g_ω, λ, a, $\hat{g}_1$, and $\hat{g}_2$ are dimensionless. The resulting ϕ_n, $\bar{\chi}$, $\bar{\omega}_0$, and K again have dimension MeV.

uum is very small, which is a consequence of the pseudoscalar wave-function renormalization $Z = 1.67 > 1$ (and thus, indirectly, of the presence of (axial-)vector mesons; for the results where (axial-)vector mesons were not taken into account, see the previous section and Ref. [138]). Moreover, we also notice the presence of a local minimum at $\phi = 38.3$ MeV, which corresponds to inhomogeneous condensation. For increasing μ the position of this minimum changes only slightly with ϕ, but it eventually becomes the global minimum and thus the thermodynamically realized ground state.

In Fig. 3.6 the behavior of the other dynamical quantities $\bar{\omega}_0$, $\bar{\chi}$, and f is displayed. For small ϕ the tetraquark condensate $\bar{\chi}$ almost vanishes and N and N^* decouple, the nucleons behave just as in the naive assignment. In this regime the CDW is present: $f \neq 0$. The suppression of $\bar{\chi}$ correlates strongly with a large $\bar{\omega}_0$. However, close to the vacuum at $\phi = 154.4$ MeV it vanishes for $\bar{\omega} = 0$ and the tetraquark condensate is $\bar{\chi} \propto \phi^2$. In the transition range when $\bar{\omega}_0$ decreases and $\bar{\chi}$ increases, nuclear matter properties can be reproduced.

In Fig. 3.7 the condensates ϕ and $\bar{\chi}$ are shown as functions of μ. For $\mu = 923$ MeV a first-order phase transition to the nuclear matter ground state takes place. Both condensates drop and then further decrease slowly

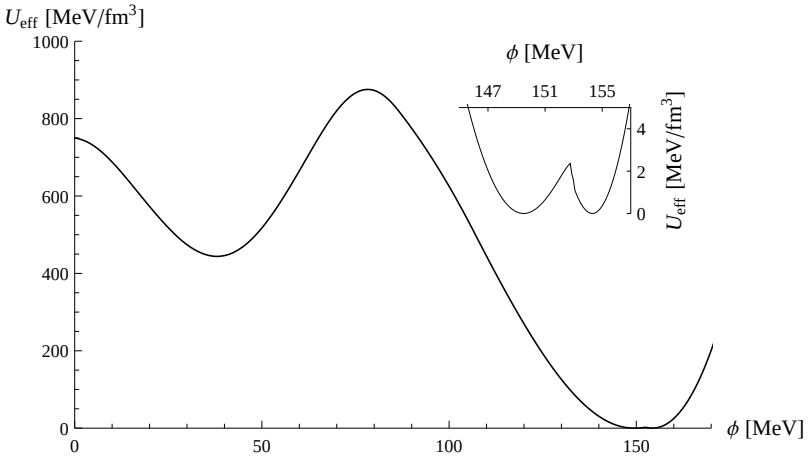

Figure 3.5: The potential U_{eff} as a function of ϕ at $\mu = 923$ MeV for $m_{N^*} = 1500$ MeV and $m_0 = 500$ MeV at the extrema of $\bar{\chi}$, $\bar{\omega}_0$, and f. In the upper right corner a zoom of the region close to the vacuum state $\phi_0 = 154.4$ MeV and nuclear matter ground-state $\phi_n = 149.5$ MeV is shown. In addition, there is a further minimum corresponding to a CDW state at $\phi = 38.3$ MeV.

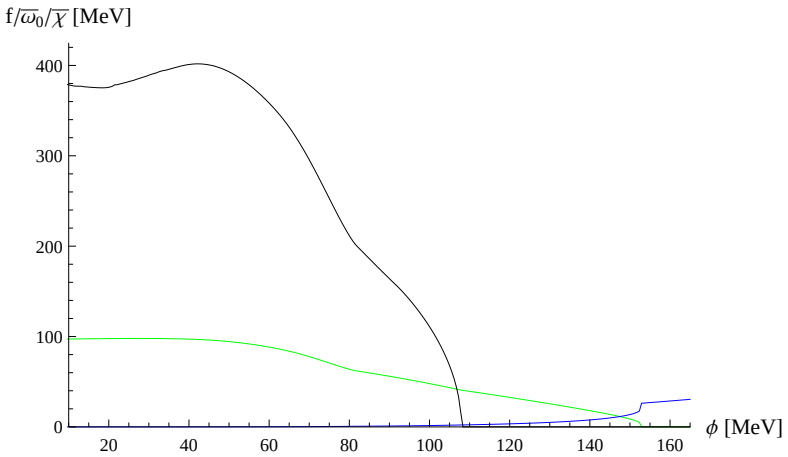

Figure 3.6: The values of the dynamical quantities f (black line), $\bar{\omega}_0$ (green line) and $\bar{\chi}$ (blue line) as a function of ϕ at $\mu = 923$ MeV for $m_{N^*} = 1500$ MeV and $m_0 = 500$ MeV which extremize the effective potential. The inhomogeneous regime is confined to $\phi < 110$ MeV. Note that only values for $\phi > 10$ MeV are displayed. $\bar{\omega}_0$ decreases with increasing ϕ and vanishes close to the vacuum state. $\bar{\chi}$ is strongly suppressed for small ϕ.

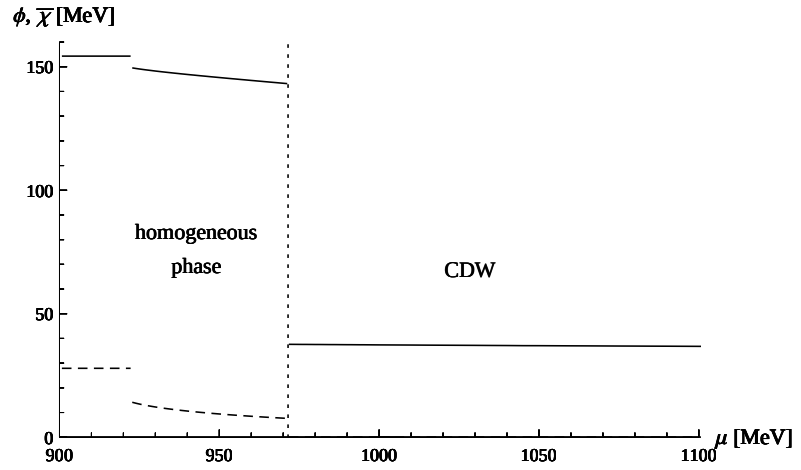

Figure 3.7: The condensates ϕ (solid line) and $\bar{\chi}$ (dashed line) are plotted as functions of μ. At $\mu = 923$ MeV a first-order phase transition to the nuclear matter ground-state takes place. Above $\mu > 975$ MeV the CDW becomes the thermodynamically realized state. In this regime the condensate $\bar{\chi}$ is very small (but nonzero).

for increasing μ. At $\mu = 973$ MeV a transition to the inhomogeneous phase occurs. The condensate $\bar{\chi}$ drops to (almost) zero and the chiral condensate ϕ to the value $\phi = 37.6$ MeV. For larger μ the condensates $\bar{\chi}$ and ϕ change very slowly. Notice that ϕ does not vanish, thus chiral symmetry is not restored. In terms of density, the onset of inhomogeneous condensation takes place at $2.5\rho_0$; this density is still small enough such that a hadronic description of the system can be applied. Then, a mixed phase is realized between $2.5\rho_0$ to $10.8\rho_0$. The latter value is too large to be trusted in a hadronic description, thus we are led to believe that somewhere in the mixed phase the deconfinement phase transition occurs.

The onset of the CDW phase can be at best shown by plotting the behavior of the parameter f, see Fig. 3.8: f vanishes for small μ, but jumps to a nonzero value ($f = 389.5$ MeV) at the critical value $\mu = 973$ MeV and then slightly increases for increasing μ. This is the CDW, with a one-dimensional harmonic modulation with a wavelength of about 1.5 fm.

After analyzing the systematics for a selected case, we turn our attention to a study of the influence of different values of the parameters m_{N^*} and m_0. In Figs. 3.9-3.11 the mass of the chiral partner of the nucleon m_{N^*} is raised from 1200 MeV to 1500 MeV and finally to 1650 MeV. The parameters are found in Tables 3.1-3.3 (including the compressibility K obtained for these

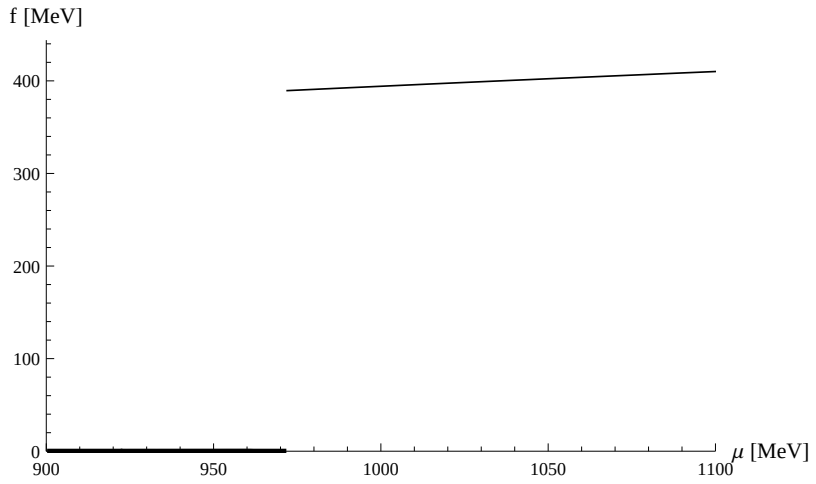

Figure 3.8: The parameter f as a function of μ.

values).

For all aforementioned cases nuclear matter ground-state properties are reproduced, if no inhomogeneous condensation occurs. As a result the nuclear matter ground state is always near $\phi_n \sim 149$ MeV close to the vacuum at $\phi = Zf_\pi = 154.3$ MeV. Around these minima the shape of the potential depends only slightly on the two input parameters. In this regime also $f = 0$ holds, in contrast to $\phi \lesssim 110$ MeV where $f \neq 0$ and the CDW dominates the potential. The CDW leads to a minimum at $\phi \sim 45$ MeV for small m_0 and lowers the potential for large m_0. This effect is more pronounced for large m_{N^*}. The interplay of these effects determines a possible homogeneous nuclear matter ground state. The chirally invariant mass contribution $\propto a\bar{\chi}$ plays a crucial role in the onset of the CDW. However, taking other quantities into account, one notices that it affects the properties of the CDW phases only indirectly. Since the tetraquark condensate vanishes for small ϕ, the values of g_ω and $\hat{g}_1$ are relevant.

Following the discussion in Ref. [82] two sets of parameters are used to describe the chiral partner of the nucleon. The first set covers a state with the mass about $m_{N^*} = 1535 \pm 15$ MeV and a rather small m_0 contribution $m_0 = 459 \pm 117$ MeV. The second set uses a mass $m_{N^*} = 1650 \pm 15$ MeV with a larger m_0 contribution $m_0 = 659 \pm 146$ MeV. In the former case the lower limit of the compressibility K can only be achieved for the upper limit of m_0; in addition, nuclear matter is not necessarily homogeneous. Using the second parameter set these problems are resolved: the compressibility K is correct and a homogeneous nuclear matter ground state is always obtained.

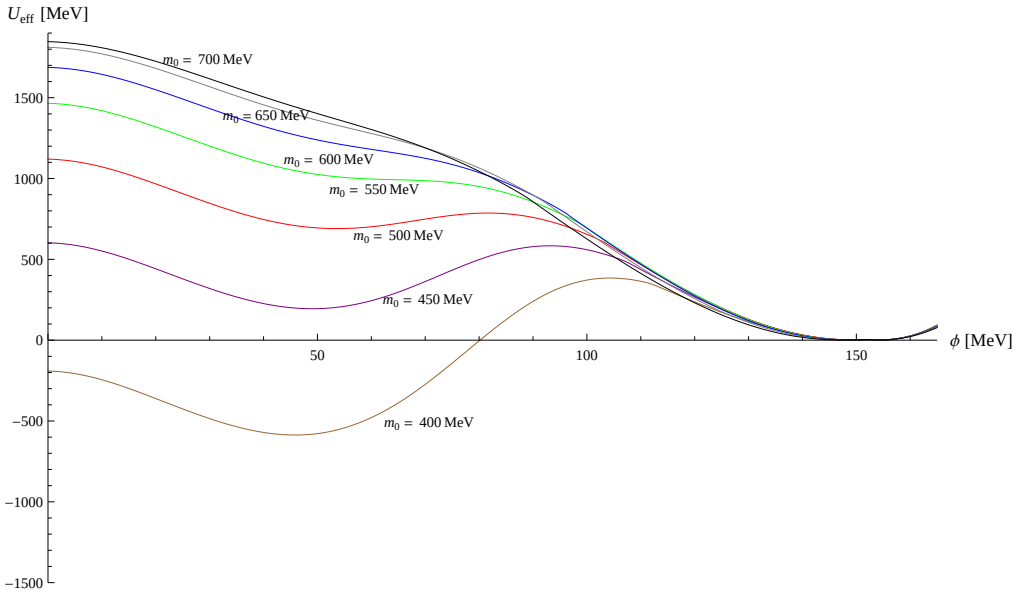

Figure 3.9: The effective potential as a function of ϕ at $\mu = 923$ MeV for $m_{N^*} = 1200$ MeV at the extrema of $\bar{\chi}$, $\bar{\omega}_0$, and f. The parameter m_0 is varied in the range $400 - 700$ MeV (brown, purple, red, green, blue, gray, black). For all cases the CDW modifies the potential at $\phi \sim 50$ MeV.

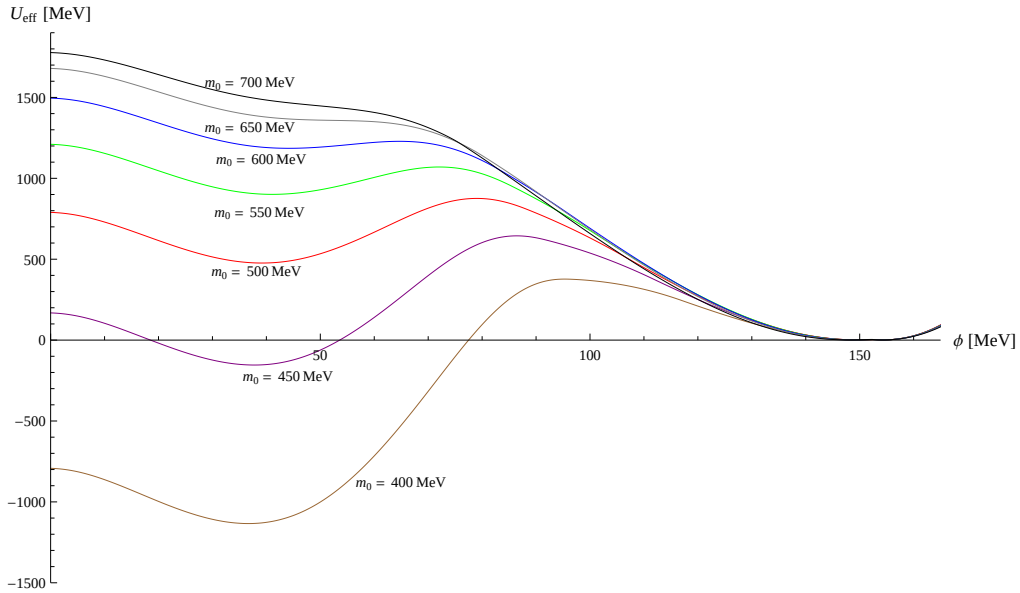

Figure 3.10: The effective potential as a function of ϕ at $\mu = 923$ MeV for $m_{N^*} = 1500$ MeV at the extrema of $\bar{\chi}$, $\bar{\omega}_0$, and f. The parameter m_0 is varied in the range $400 - 700$ MeV (brown, purple, red, green, blue, gray, black).

The behavior at nonzero μ is shown in Fig. 3.12. As already mentioned for $m_{N^*} = 1500$ MeV and small $m_0 = 450$ MeV no homogeneous ground state is present. However, for $m_0 = 500$ MeV we have the already discussed case with a transition at $\mu = 975$ MeV and the corresponding mixed phase from $\rho = 2.49\rho_0$ to $\rho = 10.75\rho_0$. For $m_{N^*} = 1650$ MeV and $m_0 = 600$ MeV a homogeneous ground state is realized up to $\mu = 1103$ MeV. This translates into a homogeneous phase up to $\rho = 4.19\rho_0$ and a mixed phase up to $\rho = 9.50\rho_0$. For a slightly higher $m_0 = 650$ MeV the homogeneous phase ends at $\mu = 1184$ MeV which corresponds to a mixed phase between $\rho = 5.04\rho_0$ and $\rho = 9.46\rho_0$. The three cases that lead to a homogeneous nuclear matter ground state differ only in the appearance of the second phase transition: the larger m_0 and m_{N^*} are, the higher μ. In the homogeneous phase as well as in the CDW phase the curves overlap. These results are summarized in Table 3.4.

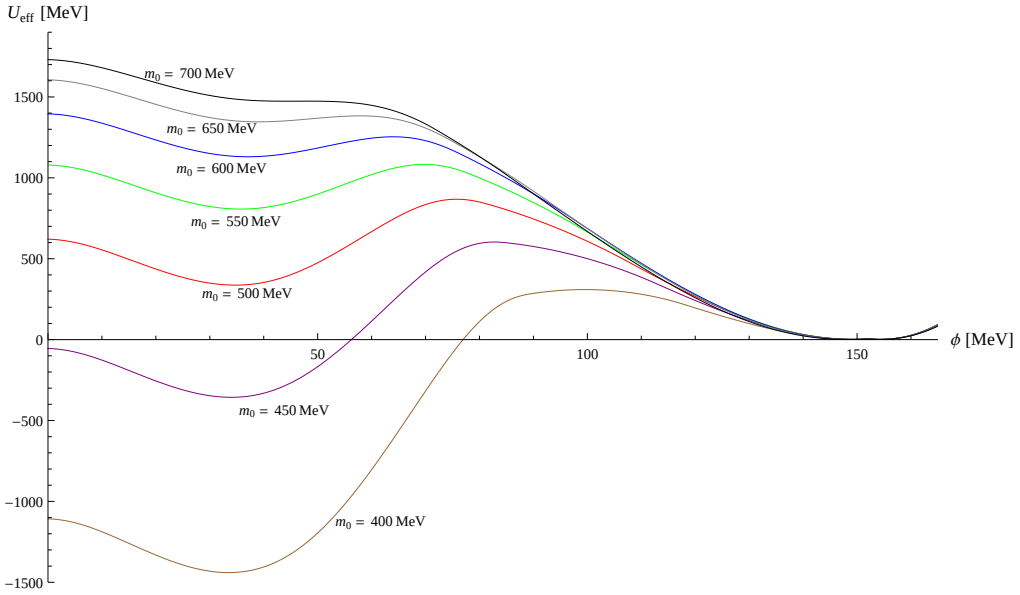

Figure 3.11: The effective potential as a function of ϕ at $\mu = 923$ MeV for $m_{N^*} = 1650$ MeV at the extrema of $\bar{\chi}$, $\bar{\omega}_0$, and f. The parameter m_0 is varied in the range $400 - 700$ MeV (brown, purple, red, green, blue, gray, black).

m_{N^*}	m_0	h.g.	μ_{CDW}	ρ_l	ρ_u	color
1500	450	no	< 923	–	–	brown
1500	500	yes	975	2.49	10.75	green
1650	600	yes	1103	4.19	9.50	red
1650	650	yes	1184	5.04	9.46	blue

Table 3.4: The presence of a homogeneous nuclear matter ground state (h.g.) as a function of m_{N^*} and m_0. The entries for m_{N^*}, m_0, and μ_{CDW} are measured in MeV, ρ_l and ρ_u in units of ρ_0. μ_{CDW} gives the value for the onset of the CDW. ρ_l and ρ_u are the lower and upper bound of the mixed regime. The color corresponds to Fig. 3.12.

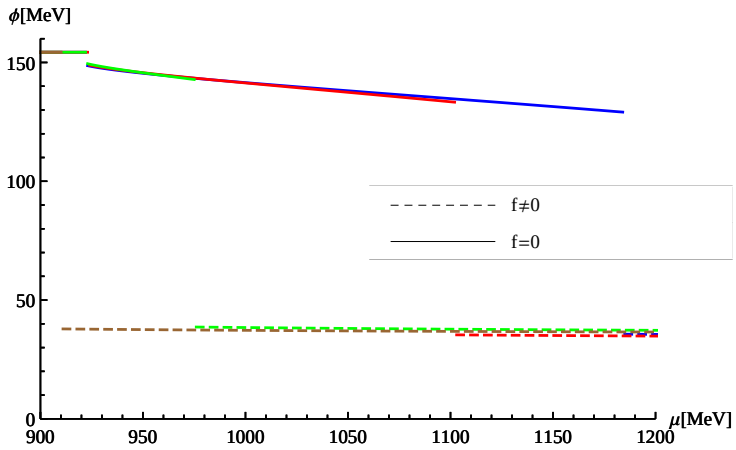

Figure 3.12: The absolute minimum ϕ of the effective potential as a function of μ for different combinations of m_{N^*} and m_0. The straight lines correspond to the case where the minimum is homogeneous and the dashed line to the case where the minimum is the CDW state. Brown line: $m_{N^*} = 1500$ MeV and $m_0 = 450$ MeV, green line: $m_{N^*} = 1500$ MeV and $m_0 = 500$ MeV (compare with ϕ in Fig. 3.7), red line: $m_{N^*} = 1650$ MeV and $m_0 = 600$ MeV, blue line: $m_{N^*} = 1650$ MeV and $m_0 = 650$ MeV. The different values for the transitions are found in Table 3.4.

Chapter 4

Arbitrary inhomogeneous modulations in $1+1$ and $3+1$ dimensions

4.1 Introductory remarks

The appearance of inhomogeneous condensation at high densities is an important phenomenon in effective models. However, the computation is in most cases not straightforward: only for very few examples the full solution is known. In this chapter we introduce the so-called finite-mode approach which was discussed for the Gross-Neveu (GN) model in Ref. [66]. We improve the finite-mode approach and apply it to a broad range of effective models in order to calculate inhomogeneous condensation. As a first step it is necessary to test the method by reproducing well-known results. The GN model and several variations of it will serve as a benchmark.

The finite-mode approach is formulated in the framework of nonzero-temperature field theory, but instead of calculating quantities in the thermodynamical limit, the spatial and temperature dimensions retain a finite size. In addition, the energy eigenstates are determined numerically: this allows to calculate thermodynamical quantities without the knowledge of the analytic expression of the energy. In principle the method allows to calculate the behavior of fermions in a magnetic field and for inhomogeneous modulation of the order parameter. The only limitation arises from computational time and the working precision of the operating system.

There are both advantages and disadvantages: The advantages are that in contrast to common lattice computations there is no sign problem at nonzero densities [18], namely it is possible to reproduce known analytic results valid

in the high-density regime. The finite-mode approach has no statistical errors, therefore quantities behave as smooth functions. This allows to optimize parameters beyond the parameter choice in lattice simulations. The determination of the optimal parameters is numerically involved, but the gained precision justifies the effort. Also, it is possible to test the convergence of physical quantities and analyze different error sources. The disadvantages are that, in order to find physically relevant results, all results have to be extrapolated to the continuum limit or alternatively one has to show that the extracted values are already close to the continuum limit. At the present stage it is not possible to describe zero-temperature physics since this would need an infinite number of temporal modes. The method is also limited in the high-temperature regime. However, a way around this problem will be introduced at the end of the following section.

In order to introduce the method, known results for the inhomogeneous condensation are verified. In a first step the already known results for the GN model and NJL_2 model in $1+1$ dimensions are reproduced and studied in detail. Afterwards the knowledge gained is applied to the $3+1$ dimensional NJL model. The peculiarities of the NJL model induced us to use a slightly different version of the method used in $1+1$ dimensions.

4.2 Inhomogeneous phases in $1+1$ dimensions

4.2.1 The Gross-Neveu model and extensions

The GN model is rather simple, but it shares features of QCD, such as asymptotic freedom, dynamical chiral symmetry breaking and its restoration, dimensional transmutation, as well as meson and baryon bound states [146]. The Lagrangian of the GN model and the NJL model, both introduced in chapter I, have a similar structure. At nonzero density it reads:

$$\mathscr{L}_{\mathrm{GN}} = \sum_{i=1}^{N} \bar{\psi}_i \left(\imath\gamma_\mu \partial^\mu + \gamma_0 \mu - m_0\right) \psi_i + \frac{1}{2} g^2 \left(\sum_{i=1}^{N} \bar{\psi}_i \psi_i\right)^2 , \tag{4.1}$$

with $\gamma_0 = -\sigma^1$ and $\gamma_1 = \imath\sigma^3$ leading to $\{\gamma_\mu, \gamma_\nu\} = 2\delta_{\mu\nu}$. Notice that chiral symmetry is realized in a discrete way, $\psi \to \gamma_5 \psi$, and the term proportional to m_0 breaks chiral symmetry explicitly (analogous to a bare quark mass). The 't Hooft limit $N \to \infty$ with $g^2 \propto 1/N$ is of interest since in this case fluctuations are suppressed and chiral symmetry is spontaneously broken [36]. However, spontaneous symmetry breaking is only realized in the limit $N \to \infty$ [147], for any finite number N there is no spontaneous symmetry breaking.

Moreover, in the 't Hooft limit an analytic solution for the thermodynamical pressure including inhomogeneous condensation can be found [146].

There are several extensions of the GN model that concern chiral symmetry. Adding the configuration $\eta = \bar{\psi}_i \imath\gamma_5 \psi_i$, the Lagrangian which is invariant under a continuous chiral symmetry (a.k.a. χGN model), reads:

$$\mathscr{L}_{\chi\mathrm{GN}} = \sum_{i=1}^{N} \bar{\psi}_i \left(\imath\gamma_\mu \partial^\mu + \gamma_0 \mu\right) \psi_i + \frac{1}{2} g^2 \left[\left(\sum_{i=1}^{N} \bar{\psi}_i \psi_i \right)^2 + \left(\sum_{i=1}^{N} \bar{\psi}_i \imath\gamma_5 \psi_i \right)^2 \right] . \tag{4.2}$$

The invariance under chiral transformations can be easily shown when one considers the fermion bilinear terms in the left-right decomposition $\psi = \psi_L + \psi_R$,

$$\begin{aligned} \bar{\psi}\psi &= \bar{\psi}_R \psi_L + \bar{\psi}_L \psi_R \ , \\ \bar{\psi}\gamma_5\psi &= -\left(\bar{\psi}_R \psi_L - \bar{\psi}_L \psi_R\right) \ , \\ \bar{\psi}\gamma_\mu\psi &= \bar{\psi}_R \gamma_\mu \psi_R + \bar{\psi}_L \gamma_\mu \psi_L \ . \end{aligned} \tag{4.3}$$

The chiral transformations of the left-handed and right-handed fermion fields are:

$$\begin{aligned} \psi_L &\to \exp(\imath\theta_L)\psi_L \ , \qquad & \bar{\psi}_L &\to \bar{\psi}_L \exp(-\imath\theta_L) \ , \\ \psi_R &\to \exp(\imath\theta_R)\psi_R \ , \qquad & \bar{\psi}_R &\to \bar{\psi}_R \exp(-\imath\theta_R) \ . \end{aligned} \tag{4.4}$$

The bosonized version of the Lagrangian reads:

$$\mathscr{L}_{\chi\mathrm{GN}} = \sum_{i=1}^{N} \bar{\psi}_i \left(\imath\gamma_\mu \partial^\mu + \gamma_0 \mu + \sigma + \imath\gamma_5 \eta\right) \psi_i + \frac{1}{2} \lambda \left(\sigma^2 + \eta^2\right) \ . \tag{4.5}$$

This version of the GN model is interesting since it favors the CDW as a ground state. The phase diagram at nonzero μ and T only shows two phases that are distinct at $T_c = e^C/\pi$ (with the Euler constant C) for all μ [148, 149].

The $O(4)$ version of the GN model (a.k.a NJL$_2$ which includes the σ-like and pion-like configurations) reads:

$$\begin{aligned} \mathscr{L}_{\mathrm{NJL}_2} = &\sum_{i=1}^{N} \bar{\psi}_i \left(\imath\gamma_\mu \partial^\mu + \gamma_0 \mu\right) \psi_i \\ &+ \frac{1}{2} g^2 \left[\left(\sum_{i=1}^{N} \bar{\psi}_i \psi_i \right)^2 + \imath \left(\sum_{i=1}^{N} \bar{\psi}_i \vec{\tau} \gamma_5 \psi_i \right)^2 \right] \ , \end{aligned} \tag{4.6}$$

with $\bar{\psi}_i = (\bar{u}, \bar{d})$. The NJL_2 model has two flavors, $f = 1, 2$. For simplicity both are assumed to be degenerate and massless. After bosonization it reduces to:

$$\mathscr{L}_{\mathrm{NJL}_2} = \sum_{i=1}^{N} \bar{\psi}_i \left(\imath \gamma_\mu \partial^\mu + \gamma_0 \mu + \sigma + \imath \gamma_5 \vec{\tau} \cdot \vec{\pi} \right) \psi_i + \frac{1}{2} \lambda \left(\sigma^2 + \vec{\pi}^2 \right) \ . \tag{4.7}$$

In contrast to the χGN model, the ground state is not a CDW. The phase diagram coincides with the GN model.

4.2.2 $1+1$ dimensional models in a box

The method of choice is the numerical Ansatz introduced in Ref. [66] to which we also refer for a detailed presentation. For simplicity we consider the chiral limit $m_0 = 0$. Since the discretization is the same for the GN, χGN, and NJL_2 model we will only discuss it for the GN model. The partition function of the GN model reads:

$$Z = \int \left(\prod_{i=1}^{N} D\bar{\psi}_i \psi_i \right) e^{-S} \ , \tag{4.8}$$

where S is the action of the GN model:

$$S = \int d^2x \left[\sum_{i=1}^{N} \bar{\psi}_i \left(\imath \gamma_\mu \partial^\mu + \gamma_0 \mu \right) \psi_i + \frac{1}{2} g^2 \left(\sum_{i=1}^{N} \bar{\psi}_i \psi_i \right)^2 \right] \ . \tag{4.9}$$

Using the standard procedure we replace the four fermion-interaction with a scalar field σ and perform a Wick rotation to Euclidean space time:

$$\begin{aligned} S_E &= \int d^2x_E \ \left[\frac{1}{2g^2} \sigma^2 + \sum_{i=1}^{N} \bar{\psi}_i \left(\gamma_\mu \partial^\mu + \gamma_0 \mu + \sigma \right) \psi_i \right] \\ &= \int d^2x_E \left(\frac{1}{2g^2} \sigma^2 + \sum_{i=1}^{N} \bar{\psi}_i Q \psi_i \right) \ , \end{aligned} \tag{4.10}$$

with the implicit definition of the Dirac operator Q. At this point the fermions can be integrated out, leading to the effective action:

$$S_E = N \int d^2x_E \ \left[\frac{1}{2\lambda} \sigma^2 - \ln \left(\det Q \right) \right] \ , \tag{4.11}$$

with the rescaled coupling $\lambda = N g^2$. The nonzero-temperature and -density behavior is found by minimizing the action S_E with respect to σ. Due to

technical problems discussed in detail in [66], it is advantageous[1] to use the operator product $Q^\dagger Q$ instead of Q:

$$\frac{S_E}{N} = \int d^2x_E \ \left[\frac{1}{2\lambda}\sigma^2 - \frac{1}{2}\ln\left(\det Q^\dagger Q\right)\right] \ . \tag{4.14}$$

Up to this point no assumption regarding σ has been made: σ and, as a consequence Q are functions of the space variable x.

In order to fix the free parameters we consider homogeneous condensation $\sigma(x) = \sigma$. The product $Q^\dagger Q$ is calculated analytically:

$$\begin{aligned}
\sum_{k_0,k_1} \ln\det\left(Q^\dagger Q\right) &= \sum_{k_0,k_1} \ln\det\left(Q^\dagger\right) + \sum_{k_0,k_1} \ln\det\left(Q\right) \\
&= \sum_{k_0,k_1} \ln\left(-\imath\gamma_0(k_0 - \imath\mu) - \gamma_1 k_1 - \sigma\right) \\
&\qquad + \sum_{k_0,k_1} \ln\left(\imath\gamma_0(k_0 + \imath\mu) + \gamma_1 k_1 - \sigma\right) \\
&= \sum_{k_0,k_1} \ln\left(k_0^2 + k_1^2 + \sigma^2 - \mu^2 + \imath 2\mu k_0\right) \\
&\qquad + \sum_{k_0,k_1} \ln\left(k_0^2 + k_1^2 + \sigma^2 - \mu^2 - \imath 2\mu k_0\right) \\
&= \sum_{k_0,k_1} \ln\left[\left(k_0^2 + k_1^2 + \sigma^2 - \mu^2\right)^2 + \left(2\mu k_0\right)^2\right] \ .
\end{aligned} \tag{4.15}$$

The effective action is evaluated in a finite box of size $V = L_0 L_1$. Within our approximation this leads to a finite number of modes N_0 and N_1; the discrete momenta k_1 and energies k_0 read:

$$k_0 = \frac{2\pi}{L_0}\left(\frac{1}{2} + n_0\right) \ , \text{ and } \quad k_1 = \frac{2\pi}{L_1} n_1 \ . \tag{4.16}$$

[1] It is possible to use the product $Q^\dagger Q$ since:

$$\sum_{k_0,k_1} \ln\det Q = \sum_{k_0,k_1} \ln\lambda_{k_0,k1} = \sum_{k_0,k_1} \ln|\lambda_{k_0,k1}| + \imath \sum_{k_0,k1} \theta_{k_0,k1} + 2m\pi \ , \tag{4.12}$$

where $\lambda_{k_0,k1}$ are the complex eigenvalues of Q and $\theta_{k_0,k1}$ is a complex phase. The parameter m is an arbitrary integer constant that can be neglected. For the operator Q the phase $\theta_{k_0,k1}$ is antisymmetric in the index k_0: $\theta_{k_0,k1} = -\theta_{-k_0,k1}$. Therefore, it follows that:

$$\sum_{k_0,k_1} \ln\det Q = \sum_{k_0,k_1} \ln|\lambda_{k_0,k1}| = \frac{1}{2}\sum_{k_0,k_1} \ln\det Q^\dagger Q \ . \tag{4.13}$$

The effective action in the box changes to:

$$\begin{aligned}\frac{S_B}{N} =& \frac{1}{2\lambda} L_1 L_0 \sigma^2 \\ & - \frac{1}{2} \sum_{n_0=1-N_0}^{N_0-1} \sum_{n_1=-N_1}^{N_1} \ln \left\{ \left[\left(\frac{2\pi}{L_0} \left(\frac{1}{2} + n_0 \right) \right)^2 + \left(\frac{2\pi}{L_1} n_1 \right)^2 + \sigma^2 - \mu^2 \right]^2 \right. \\ & \left. + \left[2\mu \frac{2\pi}{L_0} \left(\frac{1}{2} + n_0 \right) \right]^2 \right\} \ . \end{aligned} \tag{4.17}$$

The length L_0 and L_1 correspond to different cutoffs, the inverse temperature cutoff Δ and momentum cutoff Λ:

$$L_0 = \frac{1}{T} = N_0 \Delta \ , \text{ and } \quad L_1 = 2\pi \frac{N_1}{\Lambda} \ . \tag{4.18}$$

The thermodynamic limit requires that L_1 approaches infinity (continuum limit). Also the cutoff Λ has to approach infinity. Hereafter it is shown that both requirements are met for increasing N_1. In addition, increasing N_0 has to lead to $\Delta \to 0$.

It is convenient to express all variables in terms of a physical scale. To this end we rewrite them as multiples of σ_0:

$$\Lambda = \hat{f} \sigma_0 \ , \quad \Delta = \hat{s} \frac{1}{\sigma_0} \ , \quad T = \hat{t} \sigma_0 = \frac{\sigma_0}{\hat{s} N_0} \ , \quad \hat{\mu} = \frac{\mu}{\sigma_0} \ , \text{ and } \quad \hat{\sigma} = \frac{\sigma}{\sigma_0} \ , \tag{4.19}$$

where σ_0 is the vacuum expectation value of the field σ. Namely the quantity σ_0 has dimension energy and sets the energy scale of the system. The effective

action reads:

$$\begin{aligned}\frac{S_B}{N} =& \frac{1}{2\lambda} 2\pi \frac{N_1}{\hat{f}\sigma_0} \frac{\hat{s}}{\sigma_0} N_0 (\sigma_0 \hat{\sigma})^2 \\ & - \sum_{n_0=0}^{N_0-1} \sum_{n_1=-N_1}^{N_1} \ln \Bigg\{ \Bigg[\left(\frac{2\pi}{\frac{\hat{s}}{\sigma_0} N_0} \left(\frac{1}{2} + n_0 \right) \right)^2 + \left(\frac{2\pi}{2\pi \frac{N_1}{\hat{f}\sigma_0}} n_1 \right)^2 \\ & \qquad + (\sigma_0 \hat{\sigma})^2 - (\sigma_0 \hat{\mu})^2 \Bigg]^2 + \left[2\sigma_0 \hat{\mu} \frac{2\pi}{\frac{\hat{s}}{\sigma_0} N_0} \left(\frac{1}{2} + n_0 \right) \right]^2 \Bigg\} \\ =& \frac{\pi}{\lambda} N_1 N_0 \frac{\hat{s}}{\hat{f}} \hat{\sigma}^2 \\ & - \sum_{n_0=0}^{N_0-1} \sum_{n_1=-N_1}^{N_1} \ln \Bigg\{ \left[\left(\frac{2\pi}{\hat{s} N_0} \left(\frac{1}{2} + n_0 \right) \right)^2 + \left(\hat{f} \frac{n_1}{N_1} \right)^2 + \hat{\sigma}^2 - \hat{\mu}^2 \right]^2 \\ & \qquad + \left[2\hat{\mu} \frac{2\pi}{\hat{s} N_0} \left(\frac{1}{2} + n_0 \right) \right]^2 \Bigg\} \ . \end{aligned} \tag{4.20}$$

By minimizing the effective action S_B/N w.r.t. the dynamical variable $\hat{\sigma}$, the homogeneous phase diagram can be analyzed. The only missing link is the determination of the parameters $\hat{f}$, $\hat{s}$, and σ_0, which will be shown in the following section.

4.2.3 Fitting the parameters

The optimal fitting procedure ensures a small error and the best use of computational resources. At this stage the model has many parameters that have to be fixed, the number of modes N_1 and N_0 as well as the two cutoffs $\hat{s}$ and $\hat{f}$. In order to fix them one has to make use of already known results and/or has to "guess" the correct behavior. In case of the GN model this is rather simple. For low temperatures chiral symmetry is spontaneously broken. Therefore at low temperatures the condensate σ shows only a small temperature dependence and remains almost constant:

$$\sigma(T \to 0) \simeq \text{const.} \to \sigma_0 \ . \tag{4.21}$$

For the following calculation this sets the energy scale of the model. A further specific quantity is the critical temperature T_c at which chiral symmetry gets restored and the condensate vanishes:

$$\sigma(T_c) = 0 \ . \tag{4.22}$$

These two conditions are already enough to fix the parameters, as we will see in the following.

First, we consider the effective action at $\hat{\mu} = 0$. The gap equation in units of the scale σ_0 reads:

$$\begin{aligned} 0 &\stackrel{!}{=} \frac{\partial(S_B/N)}{\partial\hat{\sigma}} \\ &= 2\hat{\sigma}\left\{\frac{\pi}{2\lambda}N_1N_0\frac{\hat{s}}{\hat{f}} - \sum_{n_0=0}^{N_0-1}\sum_{n_1=-N_1}^{N_1}\frac{1}{\left[\frac{2\pi}{\hat{s}N_0}\left(\frac{1}{2}+n_0\right)\right]^2 + \left(\hat{f}\frac{n_1}{N_1}\right)^2 + \hat{\sigma}^2}\right\} . \end{aligned} \tag{4.23}$$

The gap equation has three solutions: the trivial one at $\hat{\sigma} = 0$ and two further ones which satisfy the equation:

$$\frac{\pi}{2\lambda}N_1\frac{\hat{s}}{\hat{f}} = \frac{1}{N_0}\sum_{n_0=0}^{N_0-1}\sum_{n_1=-N_1}^{N_1}\frac{1}{\left[\frac{2\pi}{\hat{s}N_0}\left(\frac{1}{2}+n_0\right)\right]^2 + \left(\hat{f}\frac{n_1}{N_1}\right)^2 + \hat{\sigma}^2} . \tag{4.24}$$

The left-hand side is independent of temperature and $\hat{\sigma}$. Therefore the equation can be used to connect the behavior of $\hat{\sigma}$ at different temperatures. Especially at the two temperatures $\hat{t} \to 0$ and $\hat{t} = \hat{t}_c$ the gap equation has to be satisfied. In order to achieve a low temperature $\hat{t}_0$ and as a consequence $\hat{\sigma}(\hat{t} \approx 0) = \hat{\sigma}_0$, the number of temperature modes N_0 has to be large. The value of N_0 that corresponds to the lowest temperature is denoted as N_{00}, with $N_{00} > 0$. This leads to the equation (in the following the effective coupling $\lambda' = \frac{\pi}{2\lambda}N_1\frac{\hat{s}}{\hat{f}}$ is used):

$$\lambda' = \frac{1}{N_{00}}\sum_{n_0=0}^{N_{00}-1}\sum_{n_1=-N_1}^{N_1}\frac{1}{\left[\frac{2\pi}{\hat{s}N_{00}}\left(\frac{1}{2}+n_0\right)\right]^2 + \left(\hat{f}\frac{n_1}{N_1}\right)^2 + {\hat{\sigma}_0}^2} . \tag{4.25}$$

A second temperature of interest is the critical temperature $\hat{t}_c$, since at this point $\hat{\sigma}(\hat{t}_c) = 0$. The temperature $\hat{t}_c$ corresponds to a certain number of temperature modes N_0 denoted as N_{0c}, with $N_{00} > N_{0c} > 0$. The gap equation follows as:

$$\lambda' = \frac{1}{N_{0c}}\sum_{n_0=0}^{N_{0c}-1}\sum_{n_1=-N_1}^{N_1}\frac{1}{\left[\frac{2\pi}{\hat{s}N_{0c}}\left(\frac{1}{2}+n_0\right)\right]^2 + \left(\hat{f}\frac{n_1}{N_1}\right)^2} . \tag{4.26}$$

These two eqs. (4.25) and (4.26) can be subtracted from each other:

$$\begin{aligned}&\frac{1}{N_{00}}\sum_{n_0=0}^{N_{00}-1}\sum_{n_1=-N_1}^{N_1}\frac{1}{\left[\frac{2\pi}{\hat{s}N_{00}}\left(\frac{1}{2}+n_0\right)\right]^2+\left(\hat{f}\frac{n_1}{N_1}\right)^2+\hat{\sigma}^2}\\ =&\frac{1}{N_{0c}}\sum_{n_0=0}^{N_{0c}-1}\sum_{n_1=-N_1}^{N_1}\frac{1}{\left[\frac{2\pi}{\hat{s}N_{0c}}\left(\frac{1}{2}+n_0\right)\right]^2+\left(\hat{f}\frac{n_1}{N_1}\right)^2}\,.\end{aligned}\tag{4.27}$$

This equation (4.27) will be referred to as the balanced gap equation (BGE). Among the parameter $\hat{s}$, $\hat{f}$, and $\hat{\sigma}_0$ only two are independent, so it is possible to absorb one. The common lattice choice is to set $1/\hat{s}=\hat{f}$ and calculate the lattice spacing $\hat{\sigma}_0$. However, in our case it is more convenient to rescale $\hat{s}$ and $\hat{f}$ with $\hat{\sigma}_0$ and set, with out loss of generality, $\hat{\sigma}_0=1$. The cutoffs $\hat{s}$ and $\hat{f}$ are treated independently (due to comparisons with $3+1$ dimensional models this choice is more intuitive, since for $3+1$ dimensional models it allows to connect the cutoff $\hat{f}$ directly to the physical cutoff of the model). Nevertheless, all the results are independent of this choice. Notice, however, that in the case of an explicit energy scale, e.g. the bare quark mass, the lattice measure $\hat{\sigma}_0$ is no longer a free parameter. The BGE (in our case without additional scales) reads:

$$\begin{aligned}0=\sum_{n_1=-N_1}^{N_1}\Bigg\{&\frac{1}{N_{00}}\sum_{n_0=0}^{N_{00}-1}\frac{1}{\left[\frac{2\pi}{\hat{s}N_{00}}\left(\frac{1}{2}+n_0\right)\right]^2+\left(\hat{f}\frac{n_1}{N_1}\right)^2+1}\\ &-\frac{1}{N_{0c}}\sum_{n_0=0}^{N_{0c}-1}\frac{1}{\left[\frac{2\pi}{\hat{s}N_{0c}}\left(\frac{1}{2}+n_0\right)\right]^2+\left(\hat{f}\frac{n_1}{N_1}\right)^2}\Bigg\}\,.\end{aligned}\tag{4.28}$$

At a first sight the BGE does not determine all different parameters. In order to constrain them further it is necessary to take a close look at their interpretation.

The parameters can be divided in to three types:

- The first type accounts for the maximum number of temperature modes N_{00} and the number of spatial modes N_1. They are limited by the available computational power. Thus they are responsible for the overall precision that can be achieved. The computational effort to calculate the effective potential is of order $O(N_0N_1)$ (with N_0 smaller or equal to N_{00}). It is crucial to achieve the maximum precision by the given

number of modes, since computational time exceeds very fast the given resources with increasing number of modes.

- There is a second type of parameter that relate the numerical quantities to physical meaningful observables. This is the temperature cutoff $\hat{s}$ which us related to the temperature $\hat{t}$ by:

$$\hat{t} = \frac{1}{N_0 \hat{s}} \ . \tag{4.29}$$

The BGE allows to connect the critical temperature $\hat{t}_c$ and the temperature $\hat{t}_0$ and therefore allows for the determination of $\hat{s}$.

- The third and last type of parameter which contains $\hat{f}$ and N_{0c} defines the actual precision. In detail these are the momentum cutoff of the box $\hat{f}$ and the number of modes N_{0c} related to the critical temperature $\hat{t}_c$. In order to fix these remaining parameters, we choose them in such a way that the physical quantity $\hat{t}_c$ which follows from the BGE is independent of $\hat{f}$ and N_{0c}:

$$\frac{\partial \hat{t}_c}{\partial \hat{f}} = 0 \ , \text{ and } \quad \frac{\partial \hat{t}_c}{\partial N_{0c}} = 0 \ . \tag{4.30}$$

These conditions guarantee the best convergence and also ensure small cutoff effects. Studying the second derivative allows to judge the quality of the approximation, since for the optimal choice the curvature approaches zero. For the BGE the derivative $\frac{\partial \hat{t}_c}{\partial \hat{f}}$ can be calculated analytically. It reads:

$$0 = \sum_{n_1=-N_1}^{N_1} n_1^2 \left\{ \frac{1}{N_{0c}} \sum_{n_0=0}^{N_{0c}-1} \frac{1}{\left\{ \left[\frac{2\pi}{N_{0c}\hat{s}} \left(\frac{1}{2} + n_0 \right) \right]^2 + \left(\hat{f} \frac{n_1}{N_1} \right)^2 \right\}^2} \right.$$
$$\left. - \frac{1}{N_{00}} \sum_{n_0=0}^{N_{00}-1} \frac{1}{\left\{ \left[\frac{2\pi}{N_{00}\hat{s}} \left(\frac{1}{2} + n_0 \right) \right]^2 + \left(\hat{f} \frac{n_1}{N_1} \right)^2 + 1 \right\}^2} \right\} . \tag{4.31}$$

Remember that $\hat{t}_c = 1/(N_{0c}\hat{s})$ and $\hat{t}_0 = 1/(N_{00}\hat{s}) = N_{0c}/N_{00}\ \hat{t}_c$. Since N_{0c} is discrete, $\frac{\partial \hat{t}_c}{\partial N_{0c}}$ has to be calculated numerically.

With these considerations the parameters can be fixed and the phase diagram can be calculated. The parameter $\hat{\sigma}_0$ is excluded in the aforementioned characterization since it is a free parameter and has therefore no influence on the precision or convergence.

Further manipulations of the BGE allow to pin down the error sources. Let us assume we have an infinite number of modes N_1. In this limit the sum over N_1 is replaced by an integral and can be solved immediately:

$$\begin{aligned} 0 =& \frac{1}{\hat{f} N_{00}} \sum_{n_0=0}^{N_{00}-1} \frac{\arctan\left[\frac{\hat{f}}{\sqrt{\left[\frac{2\pi}{\hat{s}N_{00}}\left(\frac{1}{2}+n_0\right)\right]^2+1}}\right]}{\sqrt{\left[\frac{2\pi}{\hat{s}N_{00}}\left(\frac{1}{2}+n_0\right)\right]^2+1}} \\ & - \frac{1}{\hat{f} N_{0c}} \sum_{n_0=0}^{N_{0c}-1} \frac{\arctan\left[\frac{\hat{f}}{\frac{2\pi}{\hat{s}N_{0c}}\left(\frac{1}{2}+n_0\right)}\right]}{\frac{2\pi}{\hat{s}N_{0c}}\left(\frac{1}{2}+n_0\right)} \,. \end{aligned} \tag{4.32}$$

Then, taking the limit $\hat{f} \to \infty$, the BGE reads:

$$0 = \frac{1}{N_{00}} \sum_{n_0=0}^{N_{00}-1} \frac{1}{\sqrt{\left[\frac{2\pi}{\hat{s}N_{00}}\left(\frac{1}{2}+n_0\right)\right]^2+1}} - \sum_{n_0=0}^{N_{0c}-1} \frac{1}{\frac{2\pi}{\hat{s}}\left(\frac{1}{2}+n_0\right)} \,. \tag{4.33}$$

Since the dependence of $\hat{f}$ and N_1 drops out, it is a fruitful Ansatz to pin down the error arising from N_{00} and to choose the optimal value of N_{0c}. Doing so, we find $\hat{t}_c$ as a function of N_{0c} and N_{00}. For a sufficiently large number of modes N_{00} the critical temperature $\hat{t}(N_{0c})$ has to converge to the analytically known value [37]:

$$\hat{t}_c = \lim_{N_{00}\to\infty} \hat{t}(N_{0c}) = \frac{e^C}{\pi} \,. \tag{4.34}$$

The solution for the integrated BGE for different values for N_{00} is displayed in Fig. 4.1. Suboptimal choices of N_{00} and N_{0c} lead to different error contributions. A too small number of modes N_{00} should be avoided, since it limits the achievable precision in the determination of $\hat{t}_c$. Also the number N_{0c} is connected to the accuracy. A too small number of N_{0c} cannot reproduce the behavior in the high-temperature regime. For a number close to N_{00} one has not enough modes to calculate the low-temperature regime and $\hat{\sigma}_0$ is likely not a constant. After all the resulting critical temperature is too large. The

graphical representation of the BGE in Fig. 4.1 fulfills the requirement:

$$\frac{\partial \hat{t}_c}{\partial N_{0c}} = 0 \ , \tag{4.35}$$

for best convergence, as far as a discrete quantity allows to fulfill such a condition. For a large number of modes N_{00} the critical temperature $\hat{t}_c$ only depends slightly on the number N_{0c}. Therefore, it is possible to consider temperatures above $\hat{t}_c$ and below $\hat{t}_0$, at least for a small range. The numerical studies showed that the exact value for the critical temperatures is approached from higher values. Therefore the temperature cutoff leads always to a slightly too high critical temperature.

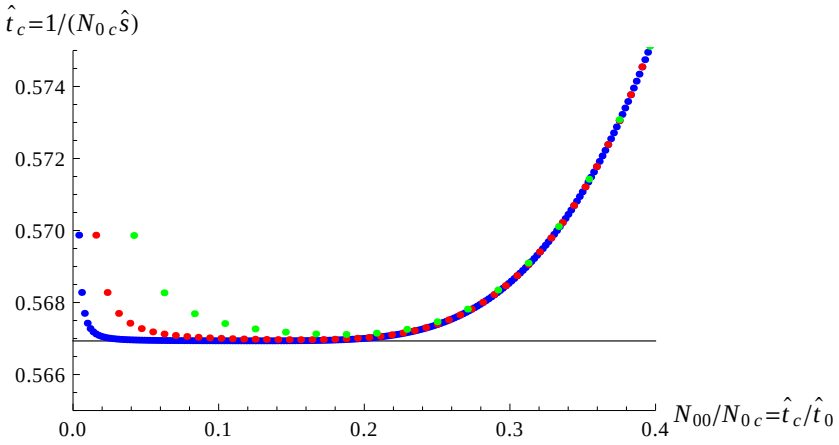

Figure 4.1: The plot shows $\hat{t}_c$ as the solution to the integrated BGE (4.33) for different choices of N_{00} as a function of N_{0c}: green dots: $N_{00} = 32$, red dots: $N_{00} = 128$, blue dots: $N_{00} = 512$, black line: analytic result $\hat{t}_c = e^C/\pi$. We distinguish three different sources for an error in the calculation of $\hat{t}_c$. It also shows how for a larger number of N_{00} the minimum moves to a smaller ratio N_{00}/N_{0c}.

Table 4.1 shows how the continuum limit for the temperature modes is realized. Already a very small number of modes is enough to have a precise determination of the critical temperature $\hat{t}_c$. However, in order to study the very low-temperature behavior the required number of modes quickly exceeds achievable sizes. For increasing box sizes the temperature cutoff $\hat{s}$ slowly converges to zero.

With the knowledge of the behavior of the temperature cutoff $\hat{s}$ as a function of N_{00} and N_{0c}, the influence of the momentum cutoff $\hat{f}$ can be analyzed. Therefore we turn our attention back to the BGE (4.27). For

N_{00}	N_{0c}	$N_{00}/N_{0c} = \hat{t}_c/\hat{t}_0$	$\hat{s}$	$1 - \hat{t}_c/\frac{e^C}{\pi}$	L_0
32	6	5.33	$2.94 \cdot 10^{-1}$	$-6.316 \cdot 10^{-4}$	9.408
48	9	5.33	$1.96 \cdot 10^{-1}$	$-3.187 \cdot 10^{-4}$	9.408
64	11	5.82	$1.60 \cdot 10^{-1}$	$-1.980 \cdot 10^{-4}$	10.24
96	16	6.00	$1.10 \cdot 10^{-1}$	$-1.005 \cdot 10^{-4}$	10.56
128	20	6.40	$8.82 \cdot 10^{-2}$	$-6.157 \cdot 10^{-5}$	11.29
256	36	7.11	$4.90 \cdot 10^{-2}$	$-1.881 \cdot 10^{-5}$	12.54
512	66	7.76	$2.67 \cdot 10^{-2}$	$-5.650 \cdot 10^{-6}$	13.67
1024	120	8.53	$1.47 \cdot 10^{-2}$	$-1.672 \cdot 10^{-6}$	15.05
2048	222	9.23	$7.95 \cdot 10^{-3}$	$-4.886 \cdot 10^{-7}$	16.28
4096	412	9.94	$4.28 \cdot 10^{-3}$	$-1.413 \cdot 10^{-7}$	17.53

Table 4.1: The table clearly shows the convergence towards the exact analytic result. Even for a small number of modes the result has only a minor error. In order to express a low temperature $\hat{t}_0$, compared to the critical $\hat{t}_c$, a significantly large number of modes N_{00} is required.

simplicity we chose the number of modes N_{00} and N_{0c} to be constant, e.g. $N_{00} = 512$ and $N_{0c} = 66$. From the previous study one knows that these values already lead to a very precise $\hat{t}_c$. Deviations from this value have to arise from the finite number of modes N_1 and a finite cutoff $\hat{f}$.

Fig. 4.2 shows the different error sources for the determination of $\hat{f}$. For a too small number of N_1 the exact value cannot be achieved. However, a high number of modes does also not guarantee a precise determination of $\hat{t}_c$. For a too small cutoff $\hat{f}$ a high number of modes does not improve the convergence, since the cutoff is just too small do describe the relevant physics. To choose a too large cutoff is also ineffective since the given number of modes is not enough to describe the desired physics. The comparison with the exact value of $\hat{t}_c$ shows that for an optimal choice for the cutoff $\hat{f}$ the distribution is flat and almost independent of $\hat{f}$, thus verifying the requirement:

$$\frac{\partial \hat{t}_c}{\partial \hat{f}} = 0 \ . \tag{4.36}$$

Table 4.2 gives an overview on how to approach the continuum limit by solving the BGE and $\frac{\partial \hat{t}_c}{\partial \hat{f}} = 0$ simultaneously. The sign change in the deviation from the exact critical temperature $\hat{t}_c = e^C/\pi$ results from the two distinct error sources. In the given example, for $N_1 = 512$ the two errors almost cancel exactly, however for other quantities this is not necessarily the case. It is remarkable that for $N_{00} = N_1$ the sizes L_0 and L are approximately

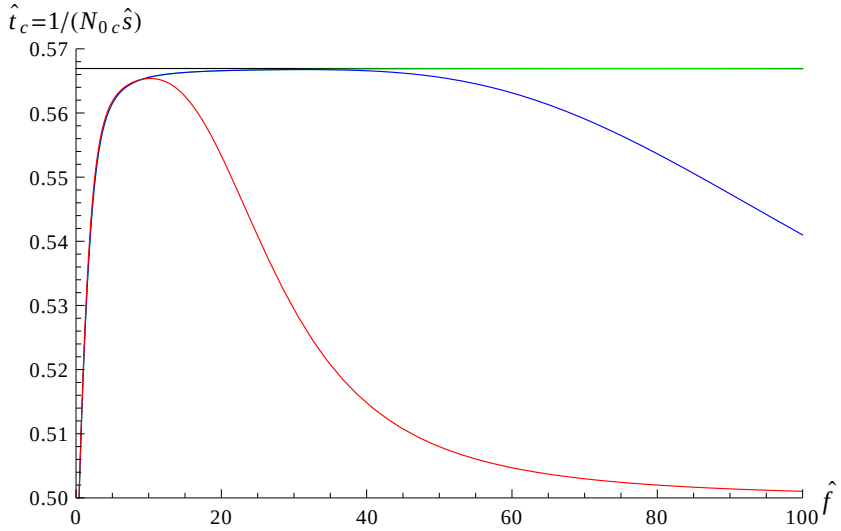

Figure 4.2: The critical temperature $\hat{t}_c$ that follows from the BGE (4.24) is plotted as a function of $\hat{f}$ for different numbers N_1: red line: $N_1 = 12$, blue line: $N_1 = 48$, green line: $N_1 = 144$, black line: analytic result. For a too small number of modes N_1 it is not possible to calculate the critical temperature. For small $\hat{f}$ the resulting critical temperature is independent of the number of modes and it is always too small. For large cutoffs and for a large number of modes the result converges towards the exact result. The low temperature is calculated with $N_{00} = 512$ and the high temperature with $N_{0c} = 66$.

equal. A detailed study shows that the errors cancel also for different sizes, namely for the pairs:

$$\begin{aligned}
&(N_{00} = 32, N_1 = 30)\ ,\\
&(N_{00} = 64, N_1 = 62)\ ,\\
&(N_{00} = 128, N_1 = 125)\ ,\\
&(N_{00} = 256, N_1 = 249)\ ,\\
&(N_{00} = 512, N_1 = 497)\ ,\\
&(N_{00} = 1024, N_1 = 993)\ ,\\
&(N_{00} = 2048, N_1 = 1984)\ ,\\
&(N_{00} = 4096, N_1 = 3956)\ .
\end{aligned} \tag{4.37}$$

These mode pairs give the smallest error of the quantity $\hat{t}_c$ compared to the exact result. With this setup it is now possible to calculate a precise homogeneous phase diagram. In order to ensure a small error, the system

size will always be chosen to symmetric, $N_{00} = N_1$. The fitting procedure is

N	$\hat{f}$	$\hat{s}$	$1 - \hat{t}_c/\frac{e^C}{\pi}$	L
12	$1.022 \cdot 10^1$	$2.680 \cdot 10^{-2}$	$2.750 \cdot 10^{-3}$	7.375
24	$1.773 \cdot 10^1$	$2.675 \cdot 10^{-2}$	$9.305 \cdot 10^{-4}$	8.507
48	$3.117 \cdot 10^1$	$2.673 \cdot 10^{-2}$	$2.998 \cdot 10^{-4}$	9.677
64	$3.954 \cdot 10^1$	$2.673 \cdot 10^{-2}$	$1.849 \cdot 10^{-5}$	10.17
128	$7.078 \cdot 10^1$	$2.673 \cdot 10^{-2}$	$5.497 \cdot 10^{-5}$	11.36
256	$1.283 \cdot 10^2$	$2.673 \cdot 10^{-2}$	$1.324 \cdot 10^{-5}$	12.54
288	$1.421 \cdot 10^2$	$2.673 \cdot 10^{-2}$	$9.747 \cdot 10^{-6}$	12.74
512	$2.345 \cdot 10^2$	$2.673 \cdot 10^{-2}$	$-3.099 \cdot 10^{-7}$	13.72
1024	$4.266 \cdot 10^2$	$2.673 \cdot 10^{-2}$	$-4.410 \cdot 10^{-6}$	15.08
2048	$7.715 \cdot 10^2$	$2.673 \cdot 10^{-2}$	$-5.409 \cdot 10^{-6}$	16.68
4096	$1.397 \cdot 10^3$	$2.673 \cdot 10^{-2}$	$-5.608 \cdot 10^{-6}$	18.42

Table 4.2: Already a reasonably small number of modes N_1 is enough to calculate the critical temperature to an acceptable precision. The low temperature is calculated with $N_{00} = 512$ and the high temperature with $N_{0c} = 66$.

the same for the GN, χGN, and NJL$_2$ models.

It is also possible to integrate over the temperature component instead of the momentum. Such a procedure allows to continuously change the temperature and even to investigate zero temperature. However, the convergence for $\hat{t}_c$ is very slow and a huge number of modes is necessary. The achievable precision can be found in Table 4.3.

4.2.4 Space-dependent operators in $1+1$ dimensions

With the aforementioned steps it is already possible to calculate the homogeneous phase diagram. In order to implement inhomogeneous condensation all the operators are in the matrix representation. At this point the explicit form of the operator Q is relevant. The nonzero-temperature studies are done in Euclidean space time. For the GN model the choice for the gamma matrices is $\gamma_0 = -\sigma_1, \gamma_1 = \imath\sigma_3$, and $\gamma_5 = -\sigma_2$. The explicit form of the operator Q is:

$$Q = \gamma_0(-\partial_0 + \mu) + \imath\gamma_1\partial_1 - \sigma(x) \ . \tag{4.38}$$

N_1	$\hat{f}$	$1-\hat{t}_c/\frac{e^C}{\pi}$
48	$3.542 \cdot 10^0$	$5.156 \cdot 10^{-2}$
125	$5.086 \cdot 10^0$	$2.750 \cdot 10^{-2}$
500	$8.210 \cdot 10^0$	$1.094 \cdot 10^{-2}$
1000	$1.377 \cdot 10^1$	$6.895 \cdot 10^{-3}$
9000	$2.167 \cdot 10^1$	$1.594 \cdot 10^{-3}$
18000	$2.626 \cdot 10^1$	$1.086 \cdot 10^{-3}$
36000	$3.442 \cdot 10^1$	$6.326 \cdot 10^{-4}$

Table 4.3: The number of modes grows rapidly with a small gain in precision. Only a huge number of modes allows for a precise determination of $\hat{t}_c$ in comparison to Table 4.1.

The space-dependent condensate is introduced as a Fourier decomposition, e.g. an x-dependent condensate:

$$\hat{\sigma}(x) = \sum_{n=-N}^{N} c_n e^{\imath n x} \ . \tag{4.39}$$

The operator Q_M reads:

$$\begin{aligned}
Q_M &= \langle k_0 \ k| \, Q \, |k_0' \ k'\rangle \\
&= \int_{x_0,x_0'} \int_{x,x'} e^{-\imath(k_0 x_0 + k x)} \\
&\qquad \times \left[-\gamma_0\partial_0 + \gamma_0\mu + \imath\gamma_1\partial_1 - \sigma(x)\right] e^{\imath(k_0' x_0' + k' x')} \delta_{x_0,x_0'}\delta_{x,x'} \\
&= \delta_{k_0,k_0'}\delta_{k,k'}\left(-\imath\gamma_0 k_0 + \gamma_0\mu - \gamma_1 k\right) - \delta_{k_0,k_0'} \sum_{n=-N}^{N} c_n \delta_{k,k'+n} \\
&= \delta_{k_0,k_0'}\delta_{k,k'}\left(-\imath\gamma_0 k_0 + \gamma_0\mu - \gamma_1 k - c_0\right) \\
&\qquad - \delta_{k_0,k_0'} \sum_{n=1}^{N} \left(c_n \delta_{k,k'+n} + c_n^* \delta_{k+n,k'}\right) \ .
\end{aligned} \tag{4.40}$$

In the matrix representation of the operator Q_M it is now possible to calculate the effective action in equation (4.11).

4.2.5 Phase diagram of the GN, χGN, and NJL$_2$ model

The different phase diagrams of the GN model, the χGN model, and the NJL$_2$ model will be presented in the following:

- **GN model:** The phase diagram of the GN model can be reproduced with high precision. In Fig. 4.3 the phase diagram is shown for a large volume. The number of modes is $N_1 = 192$ and $N_{00} = 192$. Three different phases are realized.

  For small $\hat{\mu}$ chiral symmetry is spontaneously broken and a homogeneous broken phase is present (I), for high temperature one obtains a chirally restored phase (II) and for low $\hat{t}$ and large $\hat{\mu}$ an inhomogeneous phase dominates the diagram (III). The three phases meet at a tricritial point M_3. In order to calculate the phase boundaries, different methods are used. The phase boundary I/II follows from the minimum of the effective action for a spatially independent condensate: $\hat{\sigma} = \text{const.}$ For the boundary I/III the effective action is minimized for a spatially dependent condensate: $\hat{\sigma} = \hat{\sigma}(x)$. In that case all Fourier coefficients of $\hat{\sigma}(x)$ are treated as dynamical variables. The resulting minimum is compared to the minimum that results from a homogeneous condensate. At last, the boundary II/III follows from the zero of the curvature of the potential at $\hat{\sigma} = 0$ because it is a 2^{nd} order transition (a detailed discussion is found in Appendix B).

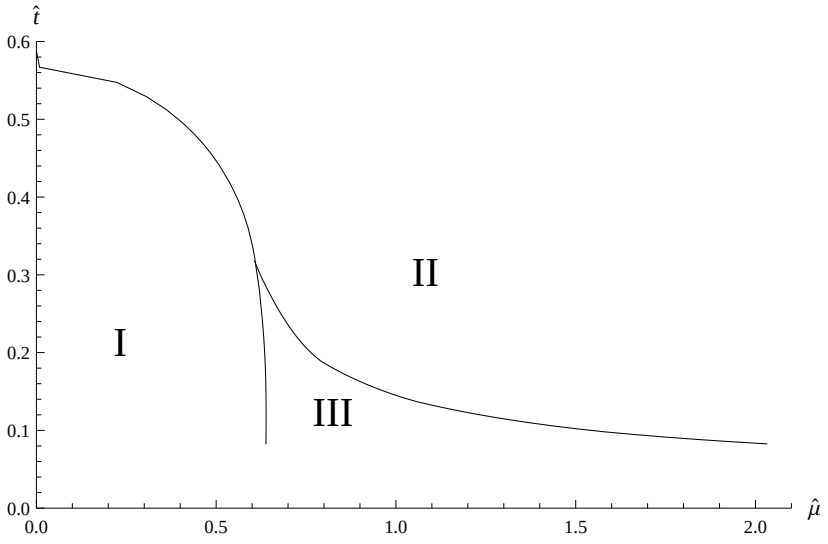

Figure 4.3: Phase diagram of the GN model for $N_{00} = N_1 = 192$ modes. Three distinguished phases are present: (I) homogeneous chirally broken phase, (II) chirally restored phase, and (III) inhomogeneous broken phase.

A case in which a different number of modes was used is presented in Fig. 4.4. On can see that only small finite-size effects close to the tri-

critical point are present. The value for the tricritical point is known

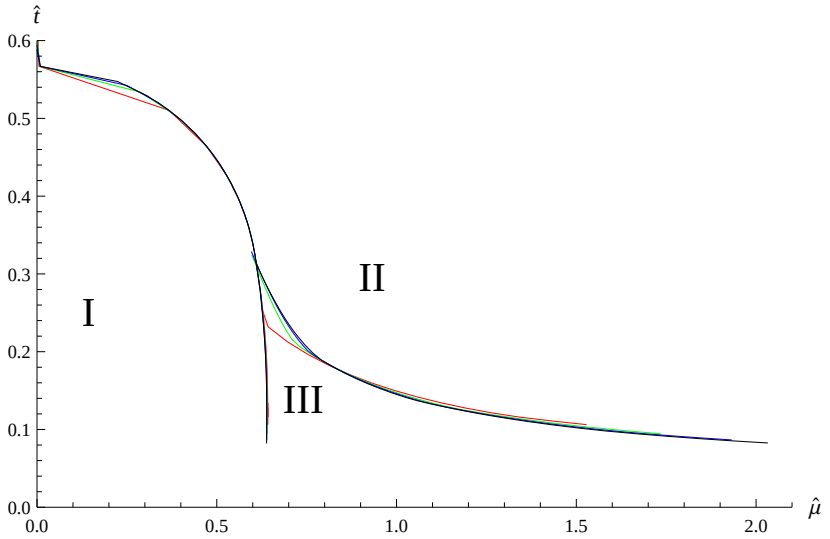

Figure 4.4: Same plot as in Fig. 4.3 but for different number of modes. Red: $N_{00} = N_1 = 48$, green: $N_{00} = N_1 = 96$, blue: $N_{00} = N_1 = 144$, and black $N_{00} = N_1 = 196$. Except close to the tricritical point the overall behavior agrees very well.

analytically as $M_3 = (\hat{\mu}_3, \hat{t}_3) = (0.608221, 0.318329)$ and the comparison with the finite-box calculations shows a good agreement:

$N_{00} = N$	$\hat{\mu}_{3,N}$	$1 - \hat{\mu}_{3,N}/\hat{\mu}_3$	$\hat{t}_{3,N}$	$1 - \hat{t}_{3,N}/\hat{t}_3$
48	0.62847	$-3.3292 \cdot 10^{-2}$	0.25051	$2.1306 \cdot 10^{-1}$
96	0.61144	$-5.2934 \cdot 10^{-3}$	0.30830	$3.1509 \cdot 10^{-2}$
144	0.60977	$-2.5458 \cdot 10^{-3}$	0.31353	$1.5078 \cdot 10^{-2}$
192	0.60938	$-1.9108 \cdot 10^{-3}$	0.31474	$1.1274 \cdot 10^{-2}$
	0.60822		0.31833	

The phase boundaries I/II, I/III and II/III at large $\hat{\mu}$ change very little. The extrapolation to the continuum limit is not necessary at this point since the changes are only marginal and the achieved precision is already remarkable. For a larger number of modes the phase diagram extends to lower temperatures. As a consequence, the inhomogeneous phase extends to higher $\hat{\mu}$. The boundary II/III shows small changes going from small to large sizes. The shape close to the phase boundary I/III is shown in Fig. 4.5. The plot justifies the description of the inhomogeneous phase with only few Fourier coefficients.

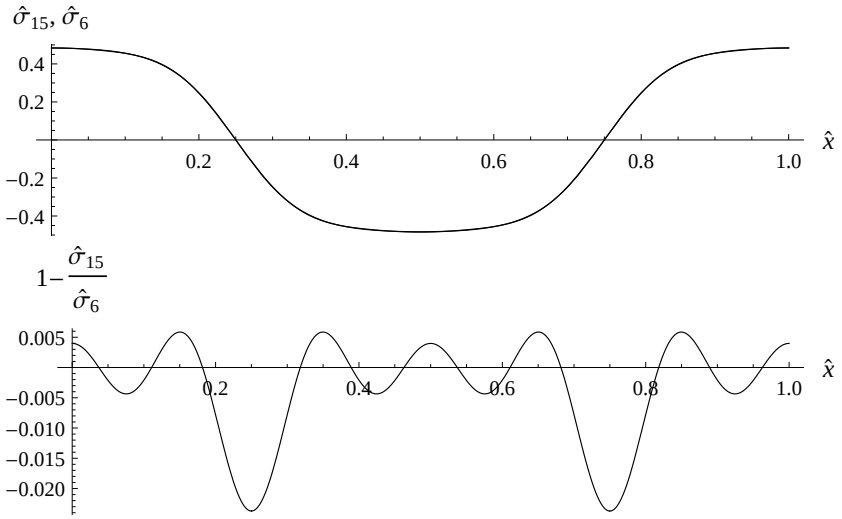

Figure 4.5: The explicit shape of the condensate close to the phase transition I to III at low temperatures. The upper panel shows the shape for a high number (15) and a small number (6) of Fourier coefficients, both coincide. However, from the lower plot where the ratio is displayed it follows that the higher-order contribution to the shape is < 1 %, and where $\hat{\sigma}$ goes through zero the contribution increases up to ~ 2.5 %.

- **χGN model:** For the χGN model the phase diagram changes completely when compared to the GN model. For temperatures above $\hat{t}_c = e^C/\pi$ and for any $\hat{\mu}$ chiral symmetry is restored. For lower temperatures there are two phases. For $\hat{\mu} = 0.0$ the homogeneous broken phase coexists with the CDW. For any $\hat{\mu} > 0.0$ the CDW is favored compared to the homogeneous phase as well as to soliton-like modulations. This can be seen in Fig. 4.6, where the effective potential is plotted for different $\hat{t}$. The system size is $N_{00} = N_1 = 96$. In this example $\hat{\sigma}$ and $\hat{\eta}$ are allowed to form an inhomogeneous condensate. The Fourier expansion for both is truncated after the first eleven complex coefficients:

$$\hat{\sigma}(x) = \sum_{n=0}^{10} c_n e^{inx} \ , \text{ and } \quad \hat{\eta}(x) = \sum_{n=0}^{10} d_n e^{inx} \ . \tag{4.41}$$

  The effective action is minimized for all 22 coefficients. As a result, for any $\hat{t}$ and $\hat{\mu}$ several local minima are obtained. The minima assigned to the CDW have only two nonzero coefficients: one for the $\hat{\sigma}$ and one for the $\hat{\eta}$, where the absolute value of both coefficient as well as the index of the Fourier coefficient coincide ($|c_n| = |d_n|$). In Fig. 4.7

the explicit shape for selected cases are shown. In a box only discrete wave vectors are realized and the index of the Fourier coefficient is proportional to the wave vector. This allows to distinguish the different local minima in Fig. 4.6 and to enumerate them according to the index of the corresponding Fourier coefficient (color coding in Fig. 4.6). The finite-size effects are corrected in the effective action with a straight line between the lowest values of the effective action at different μ (dotted line in Fig. 4.6). However, for low temperatures the minima that correspond to a CDW with an even coefficient index (c_0, c_2, $c_4 \dots$) are used. As expected, along the interpolation the wave vector grows linearly with $\hat{\mu}$. The resulting phase diagram is shown in Fig. 4.8 where only two phases are present: for low temperature the CDW is the ground state and for high temperature chiral symmetry is restored.

- **NJL_2 model:** The phase diagram of the NJL_2 model is exactly the same as the one of the GN model. However, there is a small difference. The absolute minimum is degenerate with respect to the $O(4)$ symmetry. This follows from the fact that the condensation is not necessarily aligned with the σ field. The general solution reads as:

$$\sqrt{\sigma^2 + \pi_1^2 + \pi_2^2 + \pi_3^2} \times \frac{M(x)}{A} \,, \tag{4.42}$$

where now σ and $\vec{\pi}$ are bare numbers. The function $M(x)$ is the general solution of the GN model for the inhomogeneous condensation, normalized by its amplitude A. Fig. 4.9 shows several examples and Fig. 4.10 shows how the degeneracy works. However, it is not possible to lower the energy further in the NJL_2 model.

4.3 One-dimensional modulations in $3+1$ dimensions

4.3.1 The NJL model in a box

The generalization of the finite-mode approach to higher dimensions is a nontrivial task. As outlined in chapter II the cutoff Λ of the NJL model has a physical meaning. Also the computational effort exceeds the GN model by several magnitudes.

Since the cutoff Λ has a physical meaning, the regularization scheme influences the results. As already mentioned in earlier chapters the regularization

schemes can be divided into covariance-conserving and covariance violating schemes. In any case, the physical cutoff Λ is introduced as a multiple $\hat{l}$ of the physical scale m_0^*, the constituent quark mass in the vacuum. In general m_0^* sets the energy scale of the system.

- **3d cutoff:** Considering that we study the system at nonzero density, there is a preferred frame: the one of the medium at rest. The 3d cutoff Λ_{3d} is introduced in this frame and therefore violates covariance. It is rather simple to implement since the $3d$ cutoff limits the three momenta to be $k_i < \Lambda_{3d}$. The physical cutoff $\hat{l}$ is equal to the cutoff $\hat{f}$. In the finite-mode approach each direction is treated separately:

$$|k_1| < \Lambda_{3d}\ , |k_2| < \Lambda_{3d}\ ,\ \text{and} \quad |k_3| < \Lambda_{3d}\ ,\ \text{with} \quad \Lambda_{3d} = \hat{l}\sigma_0 = \hat{f}\sigma_0\ . \tag{4.43}$$

  It follows that in this case the procedure to find the optimal $\hat{f}$ is not necessary. Still, $\hat{s}$ has to be optimized, but increasing the modes N_i simply increases the precision. The cutoff can be modified by a smearing function $g(k_i)$:

$$k_i \to k_i, \qquad g(k_i) = \left(1 - \frac{1}{1 + e^{-(|k_i| - \Lambda)/r}}\right) g(k_i)\ , \tag{4.44}$$

  where r parametrizes the smearing ($r \to 0 : g(k_i) \to \Theta(\Lambda_{3d}^2 - k_i^2)$). This leads to a cutoff $\hat{l} = \Lambda_{3d}/\sigma_0$ which is different from the cutoff $\hat{f}$. However, they fulfill the relation $\hat{f} \geq \hat{l}$ (with $r \to 0 : \hat{f} = \hat{l}$).

- **Pauli-Villars regularization:** This scheme, introduced in chapter II, leaves the covariance intact. Again, the cutoff Λ_{PV} is introduced as a multiple $\hat{l}$ of the scale m_0^*, but in contrast to the 3d scheme the cutoff $\hat{l}$ is never equal to $\hat{f}$ ($\hat{f} > \hat{l}$ must hold). The Pauli-Villars regularizations comes with one disadvantage: the computational time increases strongly with the number of regulators. For a homogeneous condensate the grand canonical potential with an arbitrary number of regulators has the form:

$$\begin{aligned} S_B =& g' N_0 \hat{m}^{*2} \\ & - \sum_a C_a \sum_{n_0, \vec{n}} \ \ln\left[\left(\hat{k}_0^2 + \hat{\vec{k}}^2 + \hat{m}^{*2} - \hat{\mu}^2 + \alpha_a \hat{l}^2\right)^2 + 4\hat{\mu}^2 k_0^2\right]\ , \end{aligned} \tag{4.45}$$

with

$$\hat{k}_0 = \frac{2\pi}{\hat{s}N_0}\left(\frac{1}{2} + n_0\right) \ , \quad \frac{1}{\hat{s}N_0} = \hat{t} \ , \text{ and } \quad \hat{k}_i = \hat{f}\frac{n_i}{N_i} \ . \tag{4.46}$$

The sum over n_0 runs from 0 to $N_0 - 1$ and for $\vec{n}$ from $-N_i$ to N_i for $i = 1 \ldots 3$. The coupling g' already takes into account the different scales and multiple factors of π. In order to compare the phase diagram for different number of regulators, the parameters are fixed to the constituent quark mass m^* and the pion decay constant f_π [22]:

$$f_\pi^2 = -\frac{3}{4\pi^2}\hat{m}^{*2}\sum_a C_a \ln\left(1 + \alpha_a \frac{\Lambda_{PV}^2}{m^{*2}}\right) \ . \tag{4.47}$$

For the NJL model in the chiral limit the pion decay constant is: $f_\pi = 88$ MeV [73].

4.3.2 Fitting the parameters

The fitting procedure requires the balanced gap equation (BGE) for the NJL model. The derivation of the BGE for the NJL model is equivalent to the GN model in chapter 4.2.3. Minimizing S_B from eq. (4.45) with respect to $\hat{m}^*$ at a low temperature $\hat{t}_0$ and the critical temperature $\hat{t}_c$, one finds the BGE that allows for fixing the parameters. Also in this case, without loss of generality one parameter is set to one: $\hat{m}_0^* = 1$. For low temperature $\hat{t}_0$ the constituent quark mass is constant: $\hat{m}^*(\hat{t}_0) \simeq \text{ const. } = \hat{m}_0^* = 1$. At the critical temperature $\hat{t}_c$ the constituent quark mass vanishes: $\hat{m}^*(\hat{t}_c) = 0$. The resulting BGE reads:

$$0 = \sum_a C_a \left[\frac{1}{N_{0c}} \sum_{n_0=0}^{N_{0c}-1} \sum_{\vec{n}} \left(\frac{1}{\hat{k}_0^2 + \hat{\vec{k}}^2 + \alpha_a \hat{l}^2}\right) - \frac{1}{N_{00}} \sum_{n_0=0}^{N_{00}-1} \sum_{\vec{n}} \left(\frac{1}{\hat{k}_0^2 + \hat{\vec{k}}^2 + 1 + \alpha_a \hat{l}^2}\right)\right] . \tag{4.48}$$

The notation is the same as in chapter 4.3.1, but for illustrative purpose we set $\hat{\mu} = 0$.

In order to test the finite-mode approach, the convergence of the critical temperature $\hat{t}_c$ as function of N_{00} and N_i will be studied in detail (the derivation follows the steps outlined in chapter 4.2.3). The knowledge about the convergence is crucial due to limited resources. The computational effort to

calculate the effective potential is of order $O(N_0 \prod_i^d N_i)$ (d is the number of spatial dimensions, N_0 is smaller or equal to N_{00}). Therefore it results that increasing the number of spatial modes by a factor of two gives an additional factor 2^d of computational time. The computational time for the effective action using Pauli-Villars regularization exceeds the time needed for the 3d cutoff regularization. The Pauli-Villars regularization, for the case of three regulators ($C_0 = 1$, $C_1 = 1$, and $C_2 = -2$ with $\alpha_0 = 0$, $\alpha_1 = 2$, and $\alpha_2 = 1$) with a mass $m^* = 300$ MeV and a cutoff $\Lambda = 647.41$ MeV, will serve as a benchmark for the achievable precision.

In Fig. 4.11 the convergence of $\hat{t}_c$ is shown. The whole fitting procedure is analog to the GN model in chapter 4.2.3. Again, two distinguished error sources can be identified. Similar to the GN model, a too small N_{00} gives rise to a too large $\hat{t}_c$, and a too small N_i leads to a too small $\hat{t}_c$. As in the GN model both error contributions almost cancel for the choice $N_{00} = N_i$ (indicated by the markers in the plot in Fig. 4.11), therefore for further considerations a symmetric system is chosen. The precision is very high, however this does not imply that other quantities have the same precision. Still, the phase diagram at high densities reaches faster the continuum limit with the symmetric choice of parameters N_i and N_{00}.

4.3.3 Space dependent operators in $3+1$ dimensions

The operator Q_M of chapter 4.2.4 can easily be generalized to $3+1$ dimensions, with an inhomogeneous condensation in $z \equiv x_3$-direction:

$$\begin{aligned} Q_{3d,M} =& \delta_{k_0,k_0'}\delta_{\vec{k},\vec{k}'}\left(-\imath\gamma_0 k_0 + \gamma_0\mu - \vec{\gamma}\vec{k} - c_0\right) \\ & - \delta_{k_0,k_0'}\sum_{n=1}^{N}\left(c_n\delta_{k_3,k_3'+n} - c_n^*\delta_{k_3,k_3'-n}\right) \ . \end{aligned} \tag{4.49}$$

However, the computational time increases a lot for the $3+1$ dimensional case. Although the operator is diagonal in k_0, k_1, and k_2, one has to calculate the determinant for each combination of these three variables. A faster way with almost the same precision follows a sightly different Ansatz. For certain operators Q_M it is possible to separate them into different orthogonal parts. Each contribution to the energy needs only to be calculated once and is independent of the other components. The single fermion energy is:

$$\gamma_0(\imath\vec{\gamma}\vec{\partial} - \sigma(x_3))\psi(\vec{x}) = E\psi(\vec{x}) \ . \tag{4.50}$$

Applying the energy operator again results in:

$$\begin{aligned} \gamma_0(\imath\vec{\gamma}\vec{\partial} - \sigma(x_3))\gamma_0(\imath\vec{\gamma}\vec{\partial} - \sigma(x_3))\psi(\vec{x}) &= E^2\psi(\vec{x}) \\ \Leftrightarrow \left[\partial_1\partial^1 + \partial_2\partial^2 + (-\imath\gamma_3\partial^3 - \sigma(x_3))(\imath\gamma_3\partial^3 - \sigma(x_3))\right]\psi(\vec{x}) &= E^2\psi(\vec{x}) \ . \end{aligned} \tag{4.51}$$

It is now possible to make a separation Ansatz and add up the eigenvalues to the total energy. For the first two this is rather simple and straightforward but the third part needs some attention. The matrix representation reads:

$$\begin{aligned} Q_{3,M} &= \langle k_3 | \, \imath\gamma_3\partial^3 - \sigma(x_3) \, | k_3' \rangle \\ &= \int_{x_3} e^{-\imath x_3 k_3} \left(\imath\gamma_3\partial^3 - \sigma(x_3)\right) e^{\imath x_3 k_3'} \\ &= -\delta_{k_3,k_3'}\gamma_3 k^3 - \sum_{n=-N}^{N} c_n \delta_{k_3,k_3'+n} \\ &= -\delta_{k_3,k_3'}(\gamma_3 k^3 - c_0) - \sum_{n=1}^{N} (c_n \delta_{k_3,k_3'+n} + c_n^* \delta_{k_3+n,k_3'}) \ . \end{aligned} \tag{4.52}$$

After calculating the eigenvalues of $Q_{3,M}$ and labeling them λ_3, the energy follows as:

$$E_{k_2,k_2,\lambda_3} = \sqrt{k_1^2 + k_2^2 + |\lambda_3|^2} \ . \tag{4.53}$$

This method has proved to be faster than calculating the determinant; it is also possible to apply it to the 3d momentum cutoff and to the Pauli-Villars regularization.

Both methods have a different scaling of the computational time with the number of modes. In the case of a one-dimensional modulation the time for a brute-force calculation of the determinant is $O(N^3)$. For $d+1$ dimensions with a one-dimensional modulation, this leads to a computational time for the effective action of:

$$t_b \sim N_0 N^{d-1} N^3 \ . \tag{4.54}$$

Using the energy eigenvalues reduces the computational time. The calculation of the eigenvalues of a matrix is an $O(N^3)$ problem as well, but it has to be done only once and therefore the computational time for the effective action reads:

$$t_e = \#N_0 N^d + \#N^3 \ . \tag{4.55}$$

The first term measures the time to sum over all energy eigenstates while the second is the time that is needed to calculate the eigenvalues. In the end the computational time t_e scales with N^3 for a number of dimensions $d \leq 3$.

4.3.4 Phase diagram of the NJL model in $3+1$ dimensions

The phase diagram of the NJL model in $3+1$ dimensions has a rich structure depending on the regularization scheme. With the 3d cutoff scheme no inhomogeneous phases are present. However, the picture changes completely when using the Pauli-Villars regularization. The resulting phase diagram for an inhomogeneous condensation in one direction $\sigma(x_3)$, see Fig. 4.12, is similar to the one found in the GN model, see Fig. 4.3. However, they differ at moderate $\hat{\mu}$ and, for certain choices of the input parameters for the NJL model, two separate inhomogeneous phases are present.

In order to have a general understanding different sets of parameters as well as different number of regulators will be considered. At first the overall phase diagram will be compared for different lattice sizes for the case $m_0 = 300$ MeV with three regulators. Hereafter three different masses m_0 are considered. Finally, the phase diagram for two different sets of regulators will be compared. The parameters for these studies can be found in Table 4.4 and Table 4.5.

m^*[MeV]	Λ[MeV]
250	736.79
300	647.41
350	608.68

Table 4.4: Parameter set for three regulators: $C_0 = 1$, $C_1 = 1$, and $C_2 = -2$ with $\alpha_0 = 0$, $\alpha_1 = 2$, and $\alpha_2 = 1$.

m^*[MeV]	Λ[MeV]
250	856.71
300	757.05
350	716.20

Table 4.5: Parameter set for four regulators: $C_0 = 1$, $C_1 = -3$, $C_2 = 3$, and $C_3 = -1$ with $\alpha_0 = 0$, $\alpha_1 = 1$, $\alpha_2 = 2$, and $\alpha_3 = 3$.

The resulting phase diagram for the benchmark case ($m_0 = 300$ MeV) shows only minor dependence on the number of modes: already small system sizes display the same structure. In Fig. 4.12 it is shown for different values of $N_{00} = N_i$. The phase diagram has two distinguished inhomogeneous phases IIIa and IIIb which are referred to as the inhomogeneous island

(IIIa) and inhomogeneous continent (IIIb) [117]. However, in contrast to previous findings [117], the continent remains finite and shares the shape of the GN model at high $\hat{\mu}$. The right boundary of the inhomogeneous island shows that an interpolation scheme which is similar to the one of the GN model (Appendix B) cannot compensate all the finite-size effects. However, for a large number N_i the shape of the phases coincide.s As a future task the interpolation scheme for small sizes has to be improved. Nevertheless, for the continent the finite-size effects are small, the deviations that can be found are moderate. The differences at $\hat{\mu} \sim 1$ GeV can be explained by the discrete temperature steps.

The comparison between different constituent quark masses m_0^* in Fig. 4.13 reveals different phase structures depending on m_0^*. The number of regulators is three and the parameters are found in Table 4.4. For $m_0^* = 250$ MeV and 300 MeV the island and the continent are separated, still the gap between them decreases with a larger m_0^*. The inhomogeneous island almost disappears for $m_0^* = 250$ MeV. In contrast, for a large $m_0^* = 350$ MeV the island reaches the continent and both merge. The results in the region below $\mu < 0.4$ GeV are in systematic agreement with the findings of Ref. [73]. The shape at high μ is very similar for different m_0^* and it follows the GN behavior in $1+1$ dimensions.

The number of regulators only affects the shape of the phase diagram in a minor way, see Fig. 4.14. The differences are marginal for the homogeneous regime and the inhomogeneous island as well as the inhomogeneous continent for low temperature. However, at moderate μ and T the inhomogeneous continent becomes larger when a larger number of regulators is considered. In principle one should consider an infinite number of regulators [150]. This is numerically not achievable, nevertheless already a finite number of regulators results in a stable phase diagram. The influence of a larger number of regulators is regarded to be small.

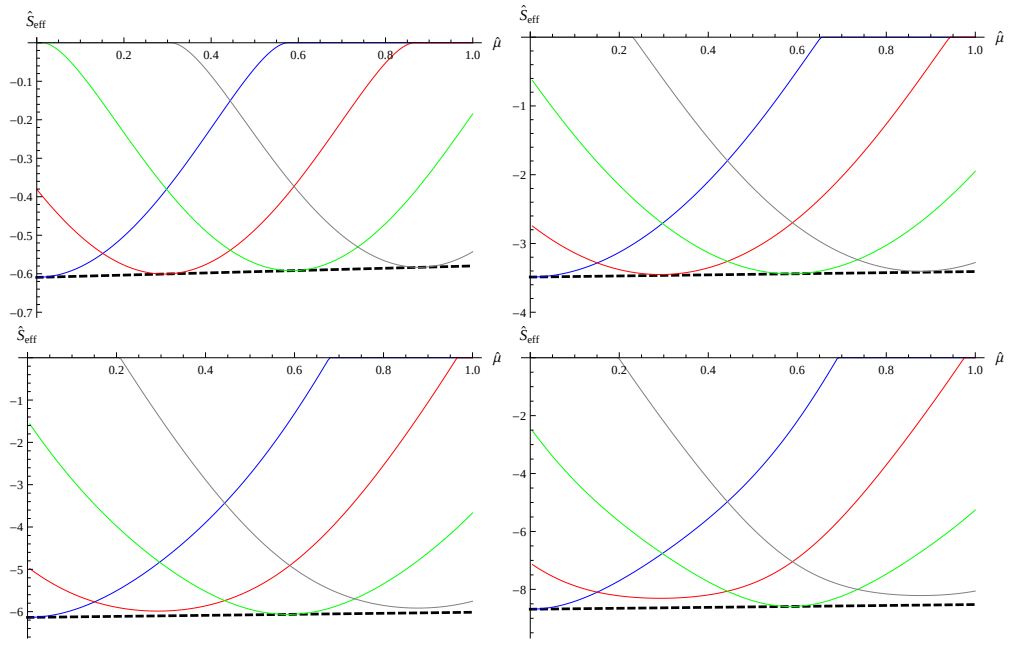

Figure 4.6: The effective action of the χGN model in the presence of the CDW. From the upper left to the lower right corner the temperature changes: $\hat{t} = 0.378$ ($N_0 = 24$), $\hat{t} = 0.189$ ($N_0 = 48$), $\hat{t} = 0.126$ ($N_0 = 72$), and $\hat{t} = 0.0945$ ($N_0 = N_{00} = 96$); for a symmetric box $N_{00} = N_1 = 96$. The colored lines are different local minima and the absolute minima as a function of $\hat{\mu}$. For the CDW only two Fourier coefficients are nonzero, one for $\hat{\sigma}$ and one for $\hat{\eta}$. Since the index for both is the same it is possible to assign the minima to a corresponding nonzero coefficient: c_0/d_0 (blue), c_1/d_1 (red), c_2/d_2 (green), c_3/d_3 (gray). The dotted line is the interpolation between the different absolute minima. The wave vector of the CDW is directly proportional to the index of the Fourier coefficient. As expected, at the absolute minimum the wave vector grows linearly with $\hat{\mu}$.

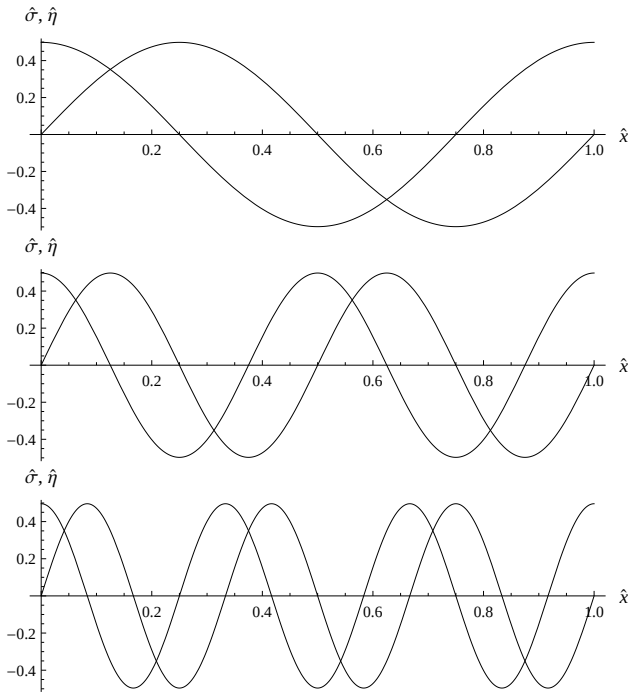

Figure 4.7: The explicit form of the inhomogeneous condensation in the χGN model. The CDW is shown for different $\hat{\mu}$ (up: $\hat{\mu} = 0.295$, middle: $\hat{\mu} = 0.585$, down: $\hat{\mu} = 0.875$) at $\hat{t} = 0.0945$.

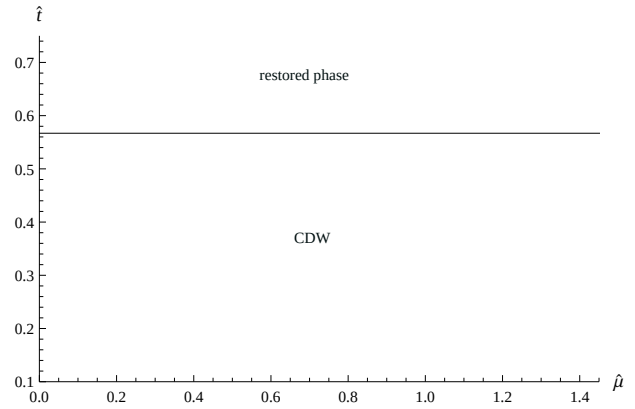

Figure 4.8: Phase diagram of the χGN model. The two phases are separated at the critical temperature $\hat{t}_c = 0.567$.

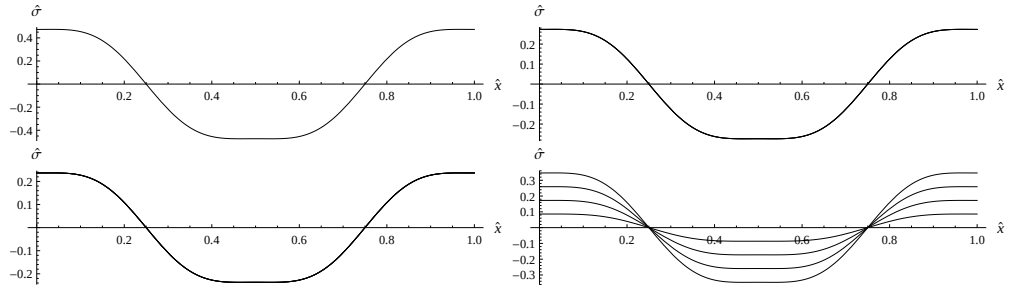

Figure 4.9: The explicit condensation in the NJL_2 model for a specific $\hat{\mu}$ close to the homogeneous/ inhomogeneous phase boundary at a low temperature. All four cases describe the same degenerate inhomogeneous absolute minimum. In the upper left corner only one field condenses, the upper right corner shows the case where three fields condense with the same amplitude, in the lower left corner four fields condense with the same amplitude and in the lower right four fields with different amplitude condense.

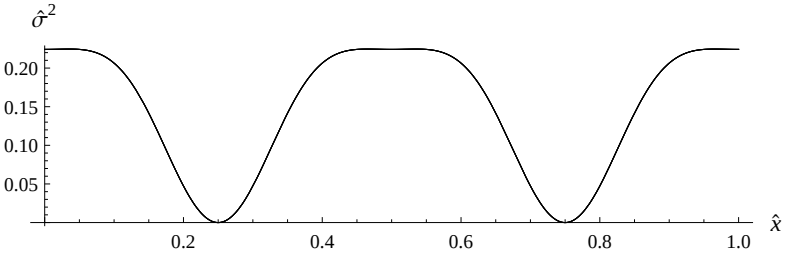

Figure 4.10: The numerical verification of eq. (4.42). All four aforementioned cases from Fig. 4.9 are plotted at once. The squares of all four curves coincides.

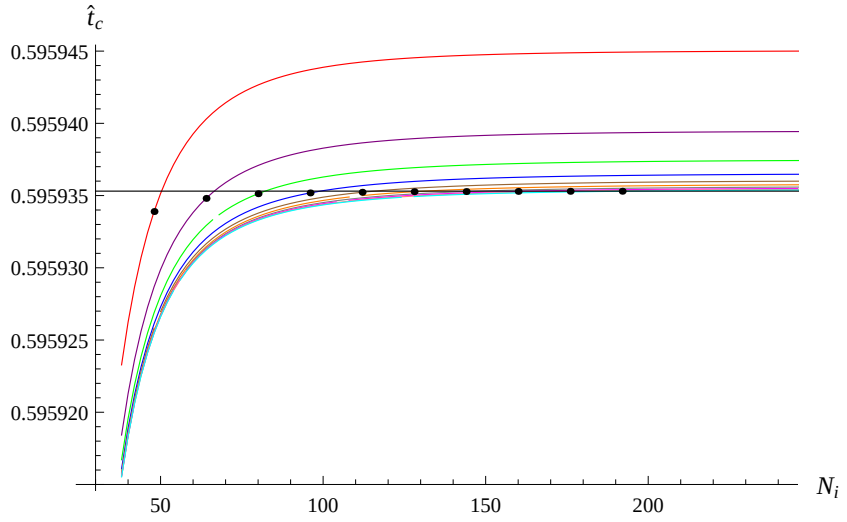

Figure 4.11: The critical temperature $\hat{t}_c$ as a function of N_i. The different colored curves represent different numbers $N_{00} = 48, \ldots, 192$, increasing in steps of $\Delta N_{00} = 16$ from red to magenta. The black markers indicate q symmetric number of modes and the black line is the result from a computation in the continuum limit $\hat{t}_c = 0.595935071$.

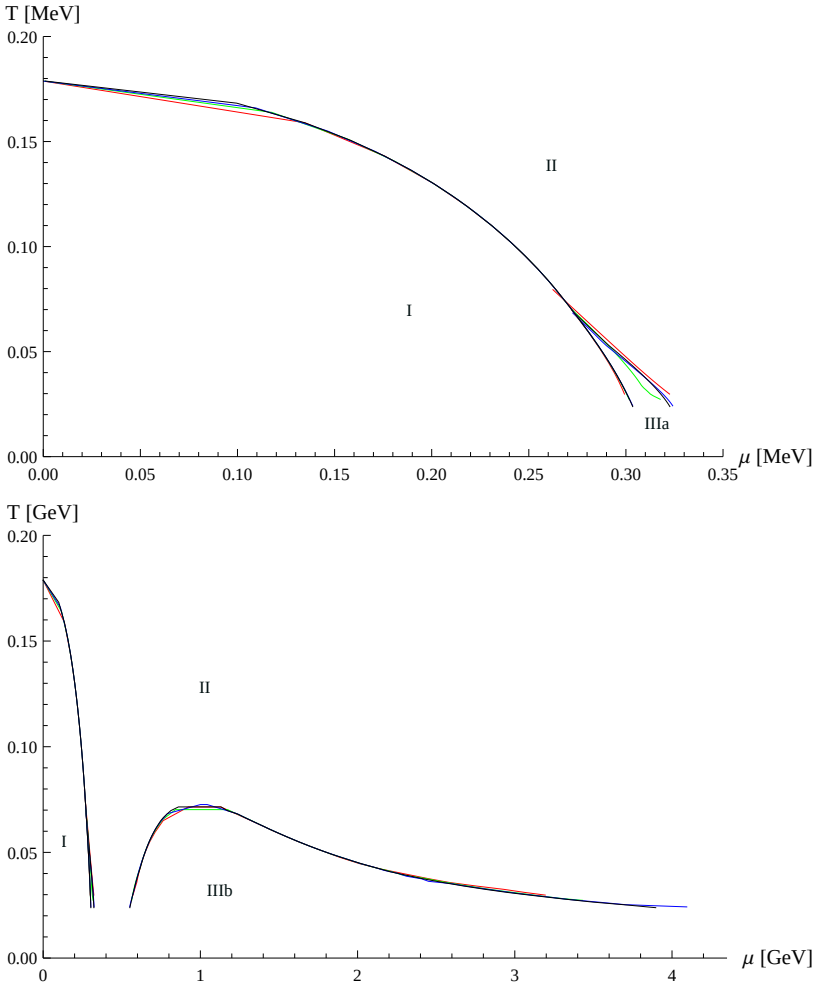

Figure 4.12: Phase diagram of the NJL model for different sizes: $N_{00} = N_i = 48, 72, 96, 120$ (red, green, blue, and black). Four distinguished phases are present: (I) homogeneous chirally broken phase, (II) chirally restored phase and (IIIa/b) inhomogeneous broken phase. The upper panel shows a zoom of the low energy regime. The lower panel shows the phase diagram including the whole (IIIb) phase.

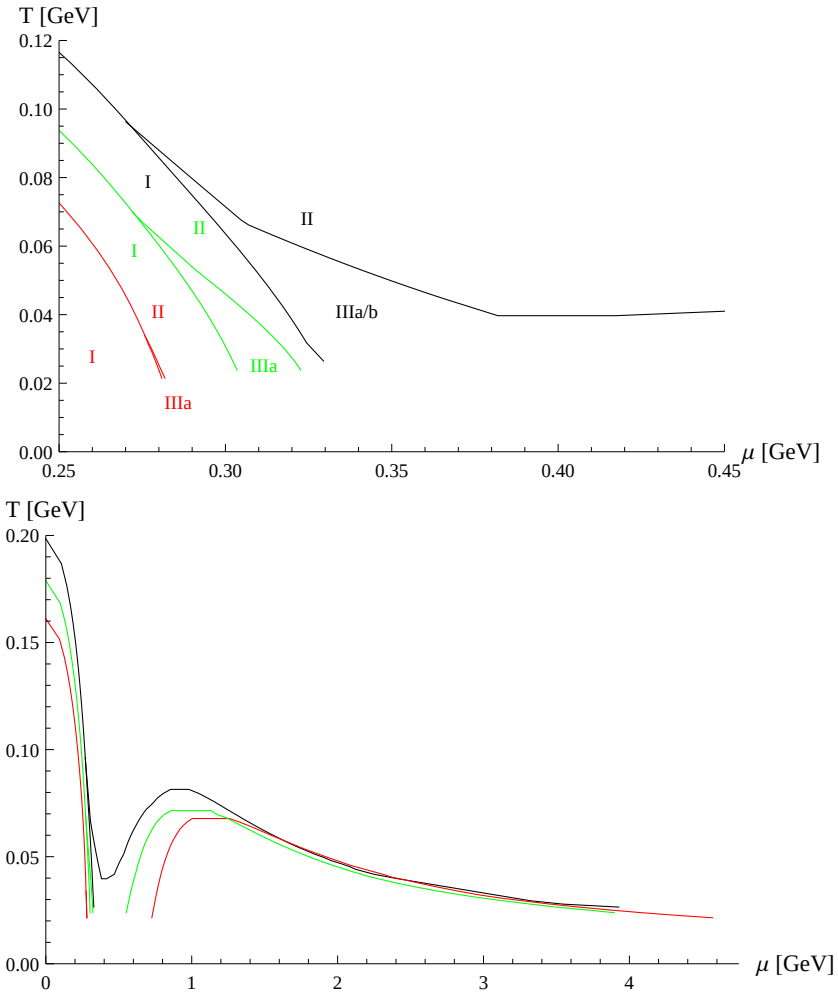

Figure 4.13: Phase diagram of the NJL model for $N_{00} = N_i = 120$, but for three different constituent quark masses $m_0^* = 250, 300, 350$ MeV (red, green, and black). Three to four distinguished phases are present: (I) homogeneous chirally broken phase, (II) chirally restored phase and (IIIa/b) inhomogeneous broken phase. In the case of $m_0^* = 350$ MeV the phases (IIIa) and (IIIb) merge. The upper panel shows the phase (IIIa) and how it changes with m_0^*. In the lower panel the whole inhomogeneous region is shown.

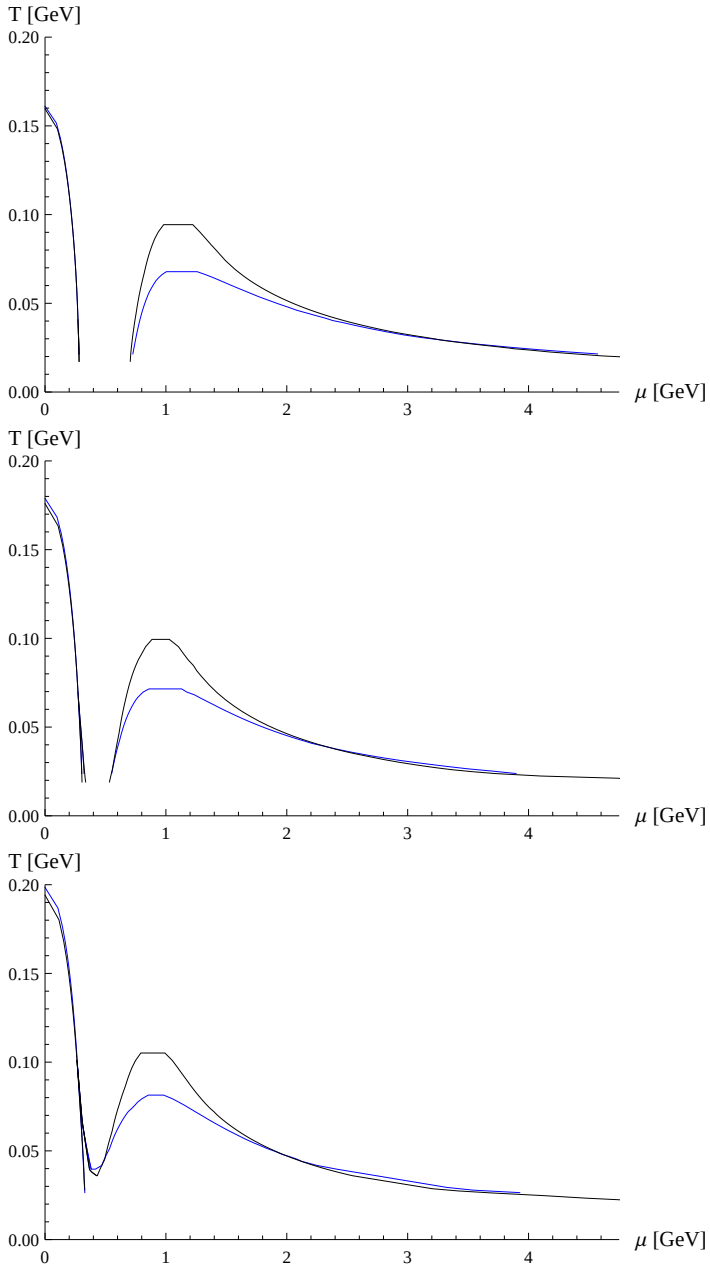

Figure 4.14: Phase diagram of the NJL model for: $N_{00} = N_i = 120$. The structure changes for different constituent quark masses $m_0^* = 250, 300, 350$ MeV (top, middle, and bottom). The number of regulators is changed from three (blue) to four (black) regulators.

Chapter 5

Outlook and Summary

5.1 Summary

The QCD phase diagram is still far from being completely understood. In this thesis we discussed several facets of it. The realization of spontaneous chiral symmetry breaking in the vacuum as well as its restoration at nonzero temperature and density were topics of detailed discussions in a broad range of models. In chapter II it could be shown that various aspects of QCD require different effective models. In chapter III a model, called the extended linear extended model (eLSM) that covers a broad range of QCD physics, was introduced. It could be shown that at high densities inhomogeneous phases in the form of a CDW are realized. In order to study inhomogeneous condensation beyond the CDW Ansatz the finite-mode approach was introduced in chapter IV. In this chapter we summarize and review the main results that we have found.

5.2 Concluding remarks about the scaling of T_c in the large-N_c limit

The NJL model and the linear σ-model predict a different scaling of the critical temperature as a function of N_c. The mismatch between the two models has been studied. The critical temperature T_c is independent of N_c in the NJL model which is based on quark degrees of freedom. The critical temperature T_c scales in the same way as the deconfinement phase transition and is $T_c \propto N_c^0$. In contrast to the NJL model, in the linear σ-model the scaling is $T_c \propto \sqrt{N_c}$.

The different scaling behavior can be explained by the distinct mecha-

nisms that trigger the phase transition. For the NJL model, quark loops are responsible for chiral symmetry restoration. Since quarks carry a color degree of freedom these loops survive in the large-N_c limit. Conversely, in the linear σ-model meson loops induce the chiral phase transition. Mesons are color neutral states and the interaction among themselves vanishes in the large-N_c limit. Therefore the critical temperature rises and approaches infinity for large N_c.

The two models are closely related and the linear σ-model can be derived from the NJL model through a hadronization procedure. However, the hadronization is only performed once at zero temperature. In order to obtain the same scaling behavior the hadronization should be performed at each T. This would actually lead to temperature-dependent parameters in the linear σ-model.

Motivated by these arguments we have chosen one parameter of the σ-model to be temperature dependent. Such a temperature-dependent parameter introduces an additional temperature scale. This modification leads to a large-N_c limit which is in agreement with the expected behavior. By tuning the additional temperature scale it is possible to lower the critical temperature to $T_c \approx 200$ MeV, a value which is in line with recent models and lattice results on the chiral phase transition. Furthermore it is clear that meson loops give a substantial reduction of the critical temperature for small N_c, they also smoothen the transition and can influence the order of the transition. However, meson loops alone are not the driving contribution behind the QCD chiral phase transition.

The aforementioned phenomenological modification of the σ-model is primitive, but there are other possibilities. Following Ref. [135] we have coupled the linear σ-model to the Polyakov loop. In the large-N_c limit the Polyakov loop dominates the properties at nonzero temperature. The chiral phase transition is triggered by the deconfinement phase transition and, as a consequence, T_c scales as N_c^0.

In conclusion, studies of the chiral phase transition within purely hadronic models are possible, but it is important to modify them to be in agreement with the large-N_c limit.

5.3 Basis for upcoming studies of inhomogeneous condensation in the eLSM

The eLSM includes (pseudo)scalar as well as (axial-)vector mesons and is capable of describing vacuum phenomenology such as the masses and decay

rates. In addition dilatation invariance can be preserved when including the dilaton field. In the baryon sector the nucleons are introduced as parity doublets. The so-called mirror assignment allows for a chirally invariant mass contribution to the nucleons, which does not originate directly from the chiral condensate. In order to ensure dilatation invariance in the baryon sector an additional scalar resonance is included: a light tetraquark/molecular state.

With the outlined model it is possible to reproduce, besides vacuum phenomenology, also nuclear matter ground-state properties, such as the binding energy and the compressibility. These achievements are in contrast to other models, e.g. the Walecka model or the Bonn potential which is not invariant under chiral transformations. The NJL model is invariant under chiral transformations, but nuclear-matter cannot be reproduced. Even in the eLSM, the reproduction of nuclear-matter properties remains a fine tuning problem. Therefore, the nuclear matter ground state serves as input parameter (except compressibility). The compressibility is calculated after all parameters were fixed and turns out to be in agreement with the experiment.

A question that arises at this point is about the nature of the nuclear matter ground state. In the eLSM the nuclear matter ground state remains homogeneous for a broad range of parameters. Still, inhomogeneous condensation in the form of a chiral density wave (CDW) at high densities is a relevant phenomenon. It is possible to change the transition from homogeneous to inhomogeneous matter by changing the mass of the chirally partner of the nucleon and the chiral invariant mass contribution.

In order to obtain these results, first a simplified version of the model was used. The explorative study showed that for $m_\pi = 139$ MeV homogeneous nuclear matter is obtained. However, the picture changes when sending the pion mass to zero (chiral limit). It is no longer possible to find a homogeneous nuclear matter ground state. At any non-zero baryon density the CDW is the favored state of matter. Therefore, the homogeneous ground state follows from the explicit symmetry breaking. Furthermore, chiral symmetry does not get restored at high baryon chemical potential and the chiral condensate even increases for increasing density.

In the next step, we showed that inhomogeneous condensation, when using the eLSM with a physical pion mass, is relevant as well. At high densities the favored ground state is always a CDW. The mechanism that ensures the formation of a homogeneous nuclear matter ground state depends on general aspects of the parity-doublet model. In the simplified version of the model, the homogeneous ground state followed from the explicit symmetry breaking. This is in contrast to the full version of the eLSM where the explicit symmetry breaking is suppressed due to the pion-wave renormalization. However, the wave-function renormalization also enables the formation of nuclear matter,

since it separates the minimum assigned to the nuclear matter ground state and the one for the CDW. The absolute location of the CDW minimum as a function of ϕ does not change much when exchanging the σ-model with the eLSM, but the location assigned to the nuclear matter ground state moves towards larger values of ϕ.

In the regime of the CDW the structure of the model changes. The link between the nucleon and its chiral partner disappears, since the tetraquark condensate approaches almost zero (the small remnant prevents a level crossing, the overall results do not change when assuming the tetraquark condensate to be zero). This allows to simplify the model in the CDW regime by considering only the nucleon. Moreover, it is believed that at high densities the transition to quark matter occurs between $\rho_0 - 10\rho_0$.

The eLSM was tested for CDW formation for three different possible chiral partners of the nucleon: $N^*(1535)$, $N^*(1650)$, and a hypothetical $N^*(1200)$. It follows that all three allow to form a homogeneous nuclear matter ground state and at high densities they lead to a CDW. However, the onset of the CDW is sensitive to m_0 and the demand for homogeneous nuclear matter sets a lower bound $m_0 \gtrsim 450$ MeV.

Using a set of parameters which allows for a correct description of the nuclear matter ground-state properties, we find that the onset of the inhomogeneous phase occurs at $2.49\rho_0$ for $m_{N^*} = 1.50$ GeV and at $4.19\rho_0$ for $m_{N^*} = 1.65$ GeV. This transition is followed by a mixed phase, where homogeneous and inhomogeneous matter coexist until $10.75\rho_0$ for $m_{N^*} = 1.50$ GeV and $9.50\rho_0$ for $m_{N^*} = 1.65$ GeV. For higher densities forms the CDW.

Upcoming studies in the framework of the parity-doublet model at nonzero densities should be performed in the $N_f = 3$ version of the model in the baryon sector. Also further parity-doublets have to be included. This leads to an enlarged mixing scenario in which the two positive-parity states $N(940)$ and $N(1440)$ together with the two-negative states $N(1535)$ and $N(1650)$ are described at the same time. Furthermore, the delta resonances are important to describe vacuum phenomenology and have to be taken adequately into account, which in the framework of the mirror assignment implies the presence of positive and negative parity $J^P = \frac{3}{2}^{\pm}$ multiplets [151]. Also, in future studies one should go beyond the CDW Ansatz. The finite-mode approach, introduced in chapter IV, allows to perform a more detailed numerical analysis of the phases that are realized.

5.4 Remarks and promising applications of the finite-mode approach

Inhomogeneous condensation is an important phenomenon at high density. A broad range of effective models show the existence of inhomogeneous phases. However, in most cases a straightforward analytic calculation is not possible. The finite-mode approach is a solid method for future studies of inhomogeneous condensation. The connection to lattice calculations allow to rely on existing results and strategies. However, since the introduced method has no statistical error, it is feasible to go beyond the limitation that arises in common lattice calculations. Also no sign problem is present. Thus, it is possible to determine different error sources and ensure the optimal criteria for convergence. The convergence is stable and for most quantities a continuum extrapolation is not necessary. Also a method to correct for finite-size effects is introduced. However, for certain cases the interpolation method needs improvement.

The parameters are optimized to show best convergence. As a result we find that the extension of the box with an almost symmetric number of modes in space and temperature directions is favored. The optimization procedure leads to a very high precision at certain points of the phase diagram. One future task will be to translate this high precision to all points of the phase diagram.

Besides the extension to higher dimensions, multiple field minimization is an achievement and an interesting application for the future. Namely, we showed that the finite-mode approach has no limitation concerning the number of inhomogeneous fields. Analytic results for up to four inhomogeneous fields are reproduced. The only limiting factor is the computational time that increases quadratically when doubling the number of Fourier coefficients describing the condensing fields.

The phase diagram of the Gross-Neveu (GN) model and of several variations of it were reproduced in great detail. It was shown that the method is capable of dealing with different box sizes and a huge number of dynamical variables. Close to the homogeneous/ inhomogeneous phase boundary soliton-like solutions minimize the potential. However, these can be approximated with a small number of Fourier coefficients. Close to the inhomogeneous/ restored phase transition sinusoidal shapes are the realized configurations.

As a first extension the so-called χGN model was introduced. The χGN model has only one flavor, but besides the σ also the η is present. The phase diagram of the χGN features a low-temperature phase where the CDW in

realized, and a high-temperature phase where chiral symmetry is restored. For low temperature the ground state is a CDW with a wave vector $\propto \mu$. Within the finite-mode approach this result can be reproduced through a dynamical minimization of two arbitrary functions, where the CDW was not an input.

Another extension is the NJL_2 model. It contains two flavors which correspond to the σ and the pion triplet degrees of freedom. The NJL_2 shows the same phase diagram as the GN model, but –in addition– the ground state is degenerate. However, no lower minimum of the potential, compared to the GN model solution, is found.

As a next step the method was extended to $3+1$ dimensions in the framework of the NJL model. Existing results could be reproduced: for the 3d momentum cutoff no inhomogeneous phases where obtained. However, with the Pauli-Villars regularization it is possible to obtain inhomogeneous phases. In addition the Pauli-Villars regularization allowed to describe the inhomogeneous continent. The continent was reported to be infinite [117] but in our analyses it remains finite and shares the shape of the GN model at high μ. This effect is stable against changes in the constituent quark mass as well as the number of regulators. In addition, for a large constituent quark mass the inhomogeneous island and continent merge. However, the physical interpretation of the inhomogeneous continent is not yet clear, further studies are needed.

At this point the method has proven to reproduce all test scenarios. These are only simple examples of what is possible. Two future applications are outlined here: the implementation of magnetic fields and higher-dimensional modulations.

The effect of magnetic fields in quark matter is an important aspect of recent discussions [152, 153, 154]. The implementation of magnetic fields is challenging and in many cases the effects are approximated by the lowest Landau level. The description of magnetic fields and inhomogeneous condensation at the same time was rarely studied in literature. However, with the finite-mode approach it is possible to answer this interesting question. Guided by the idea behind the lowest Landau-level approximation, we assume a magnetic field parallel to a possible inhomogeneous phase. The lowest Landau-level approximation results in an effective dimensional reduction. Strong magnetic fields will only allow for dynamics parallel to the magnetic field. Therefore a $3+1$ dimensional model reduces to a $1+1$ dimensional one. The finite-mode approach allows for a straightforward implementation of magnetic fields. The covariant derivative ∂_μ is replaced by $D_\mu = \partial_\mu + \imath e A_\mu$, with the external magnetic field B ($A_\mu = (0, 0, -Bx, 0)$). Calculating the en-

ergy squared one finds that a separation Ansatz can be applied:

$$\begin{aligned} &\gamma_0(\imath\vec{\gamma}\vec{D} - \sigma(x_3))\gamma_0(\imath\vec{\gamma}\vec{D} - \sigma(x_3))\psi(\vec{x}) = E^2\psi(\vec{x}) \\ \Leftrightarrow &\left[D_1D^1 + D_2D^2 + (-\imath\gamma_3\partial^3 - \sigma(x_3))(\imath\gamma_3\partial^3 - \sigma(x_3))\right]\psi(\vec{x}) = E^2\psi(\vec{x}) \ . \end{aligned} \tag{5.1}$$

Therefore the finite-mode approach allows for a study of the effect of magnetic fields on inhomogeneous condensation. Following the outlined argument for both regularizations, the 3d cutoff as well as the Pauli-Villars, should lead to a GN-like phase diagram at high magnetic fields. This is even more interesting since for the 3d cutoff no inhomogeneous condensation is present and using Pauli-Villars regularization the inhomogeneous phases in the NJL model already share, up to some extent, the structure of the GN model.

Another topic of major interest are higher-dimensional modulations. It is possible to calculate any higher-dimensional inhomogeneous structure in the finite-mode approach. However, computational resources limit such an endeavour. The calculation of a full phase diagram at a large volume and for a large variety of multidimensional inhomogeneous modulations of several fields are not yet numerically feasible. It is, however, possible to access a special class of higher-dimensional modulations. For instance in an $O(4)$ symmetric model three fields condense in different spatial directions:

$$\begin{aligned} \pi_1 &\to \pi_1(x) \\ \pi_2 &\to \pi_2(y) \\ \pi_3 &\to \pi_3(z) \ . \end{aligned} \tag{5.2}$$

Since all fields are orthogonal the energy separates in three distinguished parts:

$$\begin{aligned} E^2\psi(\vec{x}) = \big\{ &\left[-\imath\gamma_1\partial^1 - \imath\gamma_5\tau_1\pi_1(x)\right]\left[\imath\gamma_1\partial^1 - \imath\gamma_5\tau_1\pi_1(x)\right] \\ &+ \left[-\imath\gamma_2\partial^2 - \imath\gamma_5\tau_2\pi_2(y)\right]\left[\imath\gamma_2\partial^2 - \imath\gamma_5\tau_2\pi_2(y)\right] \\ &+ \left[-\imath\gamma_3\partial^3 - \imath\gamma_5\tau_3\pi_3(z)\right]\left[\imath\gamma_3\partial^3 - \imath\gamma_5\tau_3\pi_3(z)\right]\big\}\psi(\vec{x}) \ . \end{aligned} \tag{5.3}$$

This Ansatz leads to a self-consistent solution of the NJL model in $3+1$ dimensions with Jacobi elliptic functions as the general solution for each field [39]. Unfortunately, knowing these solutions does not provide us with an answer to the question, if higher-dimensional modulations are relevant or not. However, guided by these solutions it is possible to answer the question partially.

These are only two examples of many possible applications. Other promising applications are the eLSM or other hadronic models, which show that

inhomogeneous condensation is relevant at high densities. The finite-mode approach provides a strong tool to investigate them in a general framework.

On a long-term scale the finite-mode approach should contain gluon degrees of freedom (a least in an effective way). With this setup it will be possible to study inhomogeneous phases, magnetic fields, and a confining potential at the same time.

Appendix A

Characteristic polynomial

The characteristic polynomial:

$$0 = \det\left(Q_{\text{parity doublet}} - \lambda \mathbf{1}_8\right) \ , \tag{A.1}$$

where $Q_{\text{parity doublet}}$ contains all prefactors of the bilinear terms found in eq. (3.38). Since $Q_{\text{parity doublet}}$ is diagonal in $p_0 - \mu + g_\omega \bar{\omega_0}$, a shift is performed:

$$p_0 - \mu + g_\omega \bar{\omega_0} - \lambda \to p_0 \ . \tag{A.2}$$

This manipulation leads to the determinant:

$$\begin{aligned}
0 =& \det \begin{pmatrix} \not{p} + \gamma_3\gamma_5\tau_3 f - \frac{1}{2}\hat{g}_1\varphi & m_0 \\ m_0 & \not{p} - \gamma_3\gamma_5\tau_3 f + \frac{1}{2}\hat{g}_2\varphi \end{pmatrix} \\
=& \det\left[\left(\not{p} + \gamma_3\gamma_5\tau_3 f - \frac{1}{2}\hat{g}_1\varphi\right)\left(\not{p} - \gamma_3\gamma_5\tau_3 f + \frac{1}{2}\hat{g}_2\varphi\right) - m_0^2\right] \\
=& \left\{\left[p_0^2 - \vec{p}^2 - f^2 - m_0^2 - \frac{1}{4}\hat{g}_1\hat{g}_2\phi^2\right]^2 - (p_0^2 - \vec{p}^2)\left(\frac{1}{2}\hat{g}_1 - \frac{1}{2}\hat{g}_2\right)\phi^2 \right. \\
& \left. - f^2\left[4p_z^2 + \left(\frac{1}{2}\hat{g}_1 + \frac{1}{2}\hat{g}_2\right)^2\phi^2\right]\right\}^2 \\
& - (p_0^2 - \vec{p}^2 + p_z^2)\left[\left(\frac{1}{2}\hat{g}_1\right)^2 - \left(\frac{1}{2}\hat{g}_2\right)^2\right]^2 4f^2\phi^4 \\
=& \prod_{e=\pm 1,\ k=1\ldots 4}\left[p_0 + e\ \sqrt{\vec{p}^2 + m_k(p_z)^2}\right] \ .
\end{aligned} \tag{A.3}$$

Eight different energy eigenstates emerge, four positive and four negative ones, enumerated with $k = 1, \ldots, 4$. Sending the wave vector f to zero the energy levels of the parity-doublet model for homogeneous condensation are obtained. This result does not change for $m_0 = a\bar{\chi}$.

Appendix B

Phase boundary II/III

The phase boundary can be calculated in different ways. The boundary between homogeneous condensation and inhomogeneous condensation can be found by comparing the effective action at the homogeneous minimum and the effective action minimized for all Fourier coefficients c_n. In order to find the second-order phase transition from an inhomogeneous phase to a restored phase, it is advantageous to use the curvature of the effective action S_B from eq. (4.14). In general the curvature at the absolute minimum S_M of the effective action S_B vanishes for a second-order phase transition:

$$0 = \frac{\partial^2}{\partial \hat{\sigma}^2} S_M \Big|_{\hat{\sigma}=0} . \tag{B.1}$$

This is also true for a second-order phase transition from inhomogeneous condensation to restored chiral symmetry. However, for inhomogeneous condensation, $\hat{\sigma}$ is a function of x with a discrete spectrum. We define the curvature $\hat{k}$ as a function of the Fourier coefficients c_n:

$$\hat{k} = \min_{n>0} \left\{ \frac{\partial^2}{\partial c_n^2} S_B(\hat{\sigma}(x)) \Big|_{\hat{\sigma}(x)=0} \right\} . \tag{B.2}$$

The coefficient c_0 is not considered since it corresponds to a homogeneous condensate. For what concerns the phase transition from an inhomogeneous phase to a restored phase, one needs to calculate the curvature at $S_M = S_B(\hat{\sigma}(x) = 0)$. If $\hat{k} > 0$ the phase is restored and no nonzero c_n can lower the effective potential further. On the contrary, in the case $\hat{k} < 0$ it is possible to lower the effective potential with at least one nonzero c_n. The second-order phase transition takes place at $\hat{k} = 0$.

Figs. B.1, B.2 and B.3 show the curvature $\hat{k}$ at $\hat{\sigma} = 0$ as a function of $\hat{\mu}$. Each plot in the left panel shows a different temperature and different

colors stand for different N_1. The curvature $\hat{k}$ is a function of the discrete parameter n of the Fourier coefficients c_n and therefore of the discrete wave vector. This is visible in the plots as a kind of wave structure which is more pronounced for low temperatures. This structure is a finite-size effect for which $\hat{k}$ can be corrected. The interpolation is done with a parabola. The parabola is chosen in such a way that it intersects each one of the three curves $\hat{k}$ (red, black and green) in only three points. In addition, at each intersection point the derivative of $\hat{k}$ coincides with the derivative of the parabola. The three marker points are the intersection points of the parabola. The zero of the parabola that is between the lowest and highest of the three intersection points of $\hat{k}$ with the parabola is the transition point.

The right panels of Figs. B.1, B.2, and B.3 show the interpolation of the dots of the left plot. The parabolas for different sizes N_1 coincide in their transition point. We conclude that the interpolation procedure leads to a stable finite-size correction over all temperatures $\hat{t}$ and at high chemical potential $\hat{\mu}$. For low temperatures the structure is more complicated and the interpolation is done with the waves with smaller $\hat{k}$.

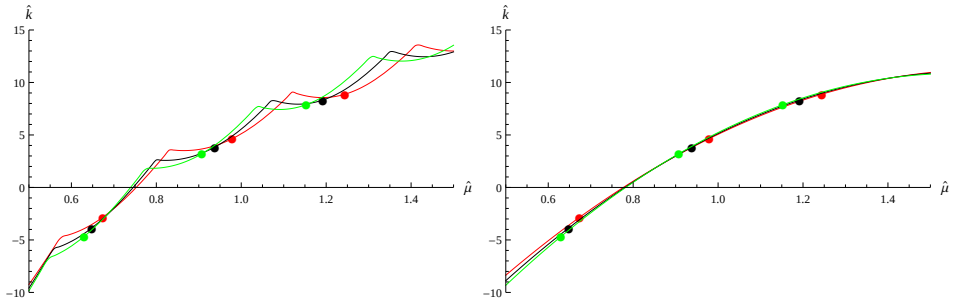

Figure B.1: $\hat{k}$ as function of μ at $\hat{t} = 0.189$ ($N_0 = 48$). The size is $N_{00} = 96$ with different $N_1 = 72,\ 96,\ 120$ (red, green, black). The left panel shows $\hat{k}$ as a function of $\hat{\mu}$ and the three intersection points of $\hat{k}$ with the parabola. The right panel shows the three intersection points of $\hat{k}$ with the parabola and the parabola itself. The interpolated transition point coincides nicely for different sizes N_1, the curves are very close to each other.

The NJL model follows the aforementioned pattern with the exception that only two points are used for the interpolation. This follows from the complicated structure of the phase diagram, which is also reflected in $\hat{k}$.

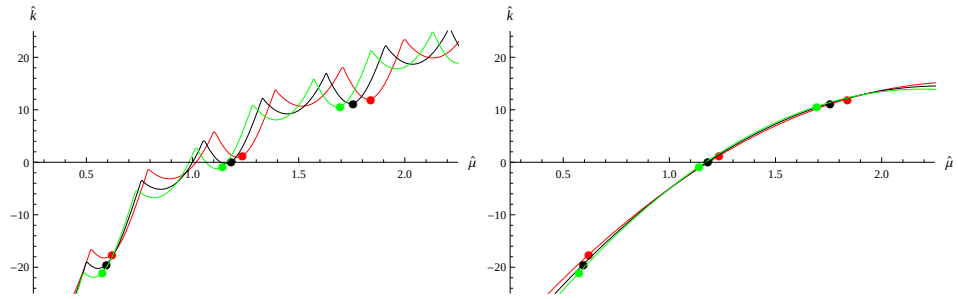

Figure B.2: $\hat{k}$ as function of μ at $\hat{t} = 0.126$ ($N_0 = 72$). The size is $N_{00} = 96$ with different $N_1 = 72,\ 96,\ 120$ (red, green, black). The left panel shows $\hat{k}$ as a function of $\hat{\mu}$ and the three intersection points of $\hat{k}$ with the parabola. The interpolation is done with every second wave, this procedure is supported by the comparison of different sizes N_1. The curves are very close to each other. The right panel shows the three intersection points of $\hat{k}$ with the parabola and the parabola itself. The interpolated transition point coincides nicely for different sizes N_1.

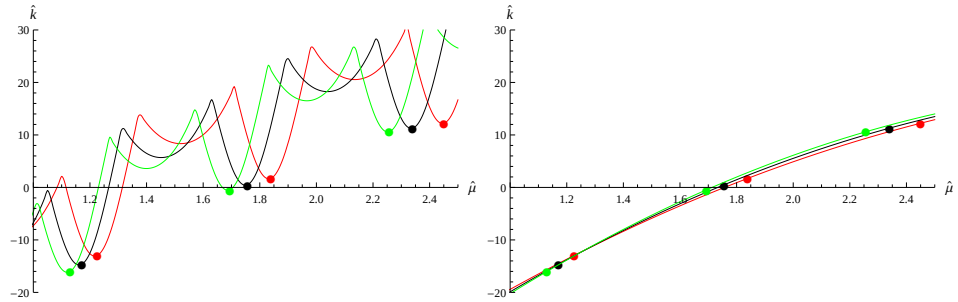

Figure B.3: $\hat{k}$ as function of μ at $\hat{t} = 0.0945$ ($N_0 = N_{00} = 96$). The size is $N_{00} = 96$ with different $N_1 = 72,\ 96,\ 120$ (red, green, black). The left panel shows $\hat{k}$ as a function of $\hat{\mu}$ and the three intersection points of $\hat{k}$ with the parabola. The interpolation is done with every second wave. This procedure is supported by the comparison of different sizes N_1. The curves are close to each other. The right panel shows the three intersection points of $\hat{k}$ with the parabola and the parabola itself. The interpolated transition point is in good agreement for different sizes N_1.

Deutschsprachige Zusammenfassung

Das QCD Phasendiagramm ist bei Weitem noch nicht vollständig verstanden und in dieser Arbeit werden verschiedene Aspekte beleuchtet. Das Auftreten der spontanen Symmetriebrechung der chiralen Symmetrie im Vakuum, sowie ihre Restauration bei endlicher Temperatur und Dichte, werden in mehreren Modellen im Detail besprochen.

Zusammenfassende Bemerkungen über das Skalieren von T_c im Large-N_c Limes

Das NJL Modell und das lineare σ-Modell sagen ein unterschiedliches skalieren der kritischen Temperatur T_c, als Funktion von N_c, voraus. Diese Diskrepanz der beiden Modelle wird in der vorliegenden Arbeit untersucht. Im NJL Modell, welches auf Quark Freiheitsgraden basiert, ist die kritische Temperatur T_c unabhängig von N_c. Die kritische Temperatur T_c skaliert somit in der gleichen Weise, wie die Temperatur des Deconfinement-Phasenübergangs. Im Gegensatz zum NJL Modell, skaliert im linearen σ-Modell die kritische Temperatur mit $T_c \propto \sqrt{N_c}$.

Das unterschiedliche Skalierungsverhalten kann auf die unterschiedlichen Mechanismen, die hinter dem Phasenübergang stehen, zurückgeführt werden. Im NJL Modell sind Quark Schleifen für die chirale Symmetrie-Wiederherstellung verantwortlich. Da Quarks einen Farbfreiheitsgrad tragen, bleiben sie im large-N_c Limit erhalten. Im Gegensatz hierzu steht das lineare σ-Modell, in welchem Mesonschleifen den chiralen Phasenübergang verantworten. Mesonen sind farbneutrale Zustände, deren Wechselwirkung untereinander im Large-N_c Limit unterdrückt wird. Aus diesem Grund steigt die kritische Temperatur und geht gegen Unendlich für großes N_c.

Die beiden Modelle stehen miteinander in enger Verbindung und das lineare σ-Modell kann über eine Hadronisierungsprozedur aus dem NJL Modell

abgeleitet werden. Grundsätzlich wird die Hadronisierung nur im Vakuum durchgeführt. Um das gleiche Skalierungsverhalten zu erhalten, muss die Hadronisierung zu jedem T durchgeführt werden, welches zu temperaturabhängigen Parameter im linearen σ-Modell führen würde.

Motiviert durch dieses Resultat, führen wir einen temperaturabhängigen Parameter im σ-Modell ein. Eine solcher temperaturabhängiger Parameter führt zu einer weiteren Energie-Skala. Diese Modifikation führt schließlich zu einem Large-N_c Limit, der mit dem erwarteten Verhalten übereinstimmt. Über diese weitere Energie-Skala ist es möglich die kritische Temperatur auf $T_c \approx 200$ MeV zu reduzieren, einen Wert, der mit aktuellen Modellen und Gitterrechnungen für den chiralen Phasenübergang übereinstimmt. Zusätzlich reduzieren die Mesonenschleifen die kritische Temperatur für $N_c = 3$ substantiell, glätten den Phasenübergang und können die Ordnung beeinflussen. Letztlich sind Mesonenschleifen also nicht die verantwortliche Kraft für den chiralen Phasenübergang.

Neben einer einfachen phänomenologischen Modifikation des linearen σ-Modells, ist es auch möglich, die Polyakov-Schleife an das lineare σ-Modell zu koppeln. Im Large-N_c Limit dominiert die Polyakov-Schleife das Verhalten bei endlicher Temperatur. Der chirale Phasenübergang wird durch den Deconfinement-Phasenübergang ausgelöst und als Konsequenz skaliert T_c wie N_c^0.

Studien des chiralen Phasenübergangs mit rein Hadronischen Modellen sind möglich, aber es ist notwendig diese Modelle zu modifizieren, um in Übereinstimmung mit dem Large-N_c Limit zu sein.

Grundlage für Studien von inhomogenen Phasen im eLSM

Das eLSM beinhaltet (Pseudo-)Skalare, sowie (Axial-)Vektor-Mesonen und ist in der Lage, Vakuum-Phänomenologie, wie Massen und Zerfallsraten, zu beschreiben. Zusätzlich kann durch Hinzunahme des Dilatonfeldes die Dilationsinvarianz sichergestellt werden. Der Baryonensektor beschreibt die Nukleonen als Paritätsdoublets und die sogenannte Spiegel Zuordnung erlaubt chiral invariante Massenbeiträge zur Nukleonenmasse, welche nicht direkt aus dem chiralen Kondensat folgen. Um schließlich die Dilationsinvarianz der Neukleonen aufrecht zu halten, wird eine weitere skalare Resonanz eingeführt: ein leichter Tetraquark/molekularer Zustand.

Mit dem eLSM ist es möglich, neben der Vakuum-Phänomenologie auch den Nuklearen Grundzustand zu beschreiben, also z.B. die Bindungsenergie,

oder die Kompressibilität. Dies steht im Gegensatz zu anderen effektiven Modellen, wie dem Walecka Modell oder dem Bonn-Potential.

Neben diesen Erfolgen stellt sich die Frage nach dem Aufbau des Nuklearen Grundzustandes. Als Resultat unserer Studie zeigt sich, dass für eine breite Wahl von Parametern der Grundzustand im eLSM homogen ist. Des Weiteren zeigt sich die Relevanz inhomogener Kondensation in Form einer CDW bei hohen Dichten. Es ist möglich den Übergang zu dieser Phase durch die Wahl des chiralen Partners des Nukleons, sowie des chiral-invarianten Massebeitrages zu beeinflussen.

Der Mechanismus, der einen homogenen Grundzustand sicherstellt, basiert auf grundlegenden Eigenschaften des eLSM. Die notwendige Wellenrenormierung der Pionen ermöglicht die Formation von homogener Materie. In einer einfacheren Variante des Modells, die keine Wellenrenormierung beinhaltet, folgt ein homogener Materie-Grundzustand aus der expliziten Brechung der chiralen Symmetrie.

Für einen CDW Grundzustand ändert sich die Struktur des Modells. Die direkte Verbindung zwischen Nukleonen und ihrem chiralen Partner ist stark unterdrückt. Dies erlaubt es für hohe Dichten Vereinfachungen vorzunehmen und das Modell auf das Nukleon zu reduzieren. Auch muss bei hohen Dichten der Übergang zur Quarkmaterie in Betracht gezogen werden.

Die Formation eines homogenen Nukleare-Materie-Grundzustandes wurde für drei verschiedene, mögliche chirale Partner des Nukleons getestet: ein hypothetischer $N^*(1200)$, $N^*(1535)$ und $N^*(1650)$. Alle drei Fälle erlauben einen homogenen Materie Grundzustand und führen zu einer CDW bei hohen Dichten. Das Einsetzen der CDW ist abhängig vom Massebeitrag m_0 zum Nukleon, der nicht aus dem chiralen Kondensat folgt. Die Notwendigkeit von homogener Materie setzt eine untere Grenze für $m_0 \gtrsim 450$ MeV.

Für die Parametersets, die eine Beschreibung des Grundzustandes zulassen, zeigt sich ein Einsetzen der inhomogenen Phase bei $2.49\rho_0$ für $m_{N^*} = 1.50$ GeV und bei $4.19\rho_0$ für $m_{N^*} = 1.65$ GeV. Diesem Übergang folgt eine gemischte Phase, in der homogene Materie und inhomogene Materie koexistieren und diese endet mit $10.75\rho_0$ für $m_{N^*} = 1.50$ GeV und $9.50\rho_0$ für $m_{N^*} = 1.65$ GeV. Höhere Dichten führen zu einer CDW.

Weiterführende Studien im Rahmen des eLSM sollten Erweiterungen auf $N_f = 3$ berücksichtigen. Auch könnten weitere Paritätsdoublets eingeführt werden, was zu einem erweiterten Mischungsszenario führen würde, welches die Paritäts-positiven Zustände $N(940)$ und $N(1440)$ zusammen mit den Paritäts-negativen Zuständen $N(1535)$ und $N(1650)$ in einem Modell beschriebe. Eine weitere wichtige Erweiterung betrifft die Delta Resonanz. Abschließend sollte eine, über den Ansatz einer CDW hinaus gehende, inhomogene Kondensation studiert werden.

Anmerkungen zum finite-mode approach

Inhomogene Kondensation ist ein wichtiges Phänomen bei hoher Dichte. Eine Vielzahl von effektiven Modellen zeigt die Existenz von inhomogenen Phasen, wobei in den meisten Fällen eine unkompliziert Berechnung nicht möglich ist. Es konnte gezeigt werde, dass der finite-mode approach eine solide Methode für zukünftige Studien im Bereich der inhomogenen Phasen bildet. Die Verbindung zu Gitterrechnungen erlaubt es, auf existierende Resultate und Strategien zurückzugreifen. Da der finite-mode approach keinen statistischen Fehler besitzt, ist es möglich, Limitierungen herkömmlicher Gitterrechnungen zu überwinden, so gibt es z.B. kein Vorzeichen Problem. Aus diesem Grund können verschiedene Fehlerquellen identifiziert und Ansätze diese zu minimieren, entwickelt werden. Dies führt zu soliden Kriterien, die zu schneller Konvergenz der Observablen führen und in bestimmten Fällen kann sogar von einer Kontinuumsextrapolation abgesehen werden. Zusätzlich werden Wege zur Volumenkorrektur aufgezeigt.

Die Parameter werden für eine bestmögliche Konvergenz optimiert, was wiederum zu einer symmetrischen Modenanzahl führt. Das Optimierungsverfahren sorgt für sehr hohe Präzision in bestimmten Punkten des Phasendiagramms. Eine Aufgabe für zukünftige Weiterentwicklungen ist es, diese Genauigkeit in alle Bereiche des Phasendiagramms zu übertragen.

Neben der Weiterentwicklung zu mehreren räumlichen Dimensionen, ist die Minimierung für mehrere Felder ein weiterer Erfolg und erlaubt für die Zukunft breit gefächerte Studien. Im Detail konnten im finite-mode approach bis zu vier inhomogene Felder simultan beschrieben werden. Der einzig limitierende Faktor ist der Rechenaufwand, welcher stark mit der Anzahl der Fourierkoeffizienten, die die zu minimierenden Felder beschreiben, ansteigt.

Das Phasendiagramm des Gross-Neveu (GN) Modells, sowie verschiedener Variationen, konnte im Detail reproduziert werden. Neben verschiedenen Modenanzahlen wurde auch eine große Anzahl dynamisch minimierter Fourierkoeffizienten getestet. Nahe der Phasengrenze zwischen homogener und inhomogener Kondensation wird das Potential durch Soliton-ähnliche Strukturen minimiert. Es folgt, dass diese schon mit einer geringen Anzahl von Fourierkoeffizienten beschrieben werden können. An der Phasengrenze zwischen inhomogener und restaurierter Phase sind sinusförmige Strukturen die bevorzugte Konfiguration.

Eine der ersten Erweiterungen des GN Modells ist das sogenannte chirale GN (χGN) Modell, welches neben dem σ, auch den η Zustand beschreibt. Das Phasendiagramm des χGN Modells unterteilt sich in eine Phase bei niedriger Temperatur, in der die CDW realisiert ist und eine Phase bei hoher

Temperatur, in der die chirale Symmetrie wiederhergestellt ist. Für niedrige Temperaturen ist der Wellenvektor der CDW $\propto \mu$. Mit dem finite-mode approach kann dieses Resultat durch eine dynamische Minimierung zweier beliebiger Funktionen reproduziert werden, wobei angemerkt sei, dass die CDW keine Eingabe der Lösung ist.

Eine andere Weiterentwicklung ist das NJL_2 Modell. Dieses Modell beinhaltet neben dem σ auch das Pionen-Triplett als Freiheitsgrade. Das NJL_2 Modell resultiert im selben Phasendiagramm, wie das GN Modell, aber zusätzlich ist der Grundzustand entartet. Trotz alledem kann im Vergleich zum GN Modell kein bevorzugtes Minimum gefunden werden.

In einem weiteren Schritt wurde der finite-mode approach für das NJL Modell in $3+1$ Dimensionen weiterentwickelt. Bereits existierende Resultate konnten reproduziert werden: für eine 3d Impuls-Regularisierung wurden keine inhomogenen Phasen gefunden. Demgegenüber war es möglich, mit der Pauli-Villars Regularisierung inhomogene Phasen zu erhalten. Des Weiteren erlaubte die Pauli-Villars Regularisierung eine detaillierte Untersuchung der inhomogenen Phase. Der inhomogene Kontinent wurde in der gängigen Literatur als unendlich groß beschrieben, wohingegen unsere Analyse auf einen kleineren Kontinent schließen lässt, der für hohes chemischen Potential eine Form, ähnlich der des GN Modells aufweist. Dieser Effekt ist stabil gegenüber verschiedenen Konstituentenquarkmassen, sowie einer unterschiedlichen Anzahl von Regulatoren. Zusätzlich zeigt sich für große Konstituentenquarkmassen ein Verschmelzen des inhomogenen Kontinents mit der inhomogenen Insel. Allerdings ist die physikalische Bedeutung des inhomogenen Kontinents mit dieser Studie nicht geklärt und weitere Untersuchungen sind notwendig.

Der finite-mode apporach konnte alle Testszenarien erfolgreich berechnen. Dies sind aber nur wenige einfache Beispiele. Zwei weitere, sehr vielversprechende Anwendungsbeispiele, sind mehrdimensionale Modulationen, sowie das Einbinden magnetischer Felder. In einem Langzeit-Ziel sollten auch gluonische Freiheitsgrade (zumindest in einer effektiven Beschreibung) eingebunden werden. Mit diesem Aufbau wäre es möglich, den Effekt von magnetischen Feldern, inhomogener Kondensation und eines konfinierenden Potentials zu untersuchen.

Curriculum vitae

Personal Information

Nationality	German
Date of birth	21. April 1983, Kaiserslautern

Education

2010–2014	**Ph.D.**
Title	*"QCD under extreme conditions: inhomogeneous condensation"*
Supervisor	Prof. Dr. Dirk H. Rischke
University	Goethe Universität, Frankfurt am Main
2003–2009	**Diplomstudiengang Physik**
Title	*"The effect of the tetraquark to the chiral phase transition"*
Supervisor	Prof. Dr. Dirk H. Rischke
University	Goethe Universität, Frankfurt am Main
2003–2009	**Abitur**
School	Burggymnasium, Kaiserslautern

Teaching experience

2007–2009	Tutor in theoretical physics

Scholarships and Memberships

since 2009	The Helmholtz Graduate School for Hadron and Ion Research "HGS-HIRe for FAIR"
since 2009	Helmholtz Research School for Quark Matter Studies in Heavy Ion Collisions
since 2003	Member of DPG

Computer skills

Languages and Libraries:

advanced	C++, Fortran, GNU Scientific Library
proficient	Numerical Algorithms Group, OpenMP

Scientific Softwares:

advanced	Mathematica
proficient	LaTeX

Operative systems:

advanced	UNIX, Microsoft Windows

Languages

German	Native
English	Fluent

Publications

Refereed Journal Articles:

2012	*"Restoration of chiral symmetry in the large-N_c limit"*, A. Heinz, F. Giacosa and D. H. Rischke, Phys. Rev. D **85**, 056005
2009	*"Role of the tetraquark in the chiral phase transition"*, A. Heinz, S. Struber, F. Giacosa and D. H. Rischke, Phys. Rev. D **79**, 037502

Submitted Articles:

2013	*"Chiral-density wave in nuclear matter"*, A. Heinz, F. Giacosa and D. H. Rischke, arXiv:1312.3244 [nucl-th], submitted to NPA

Conference Proceedings:

2012	*"Inhomogeneous condensates in the parity doublet model"*, A. Heinz, PoS ConfinementX, 250
2011	*"Phenomenological Improvement of the Linear-σ Model in the Large-N_c Limit"*, A. Heinz, Acta Phys. Polon. Supp. **4**, 561
2010	*"Light tetraquark state at nonzero temperature"*, A. Heinz, S. Struber, F. Giacosa and D. H. Rischke, Acta Phys. Polon. Supp. **3**, 925

Manuscript in Preparation:

2014	*"Inhomogeneous phases in effective quark models"*, A. Heinz, F. Giacosa, M. Wagner and D. H. Rischke

Conferences and Workshops

2014, Poster	Quark Matter, Darmstadt *"Inhomogeneous phases in 1+1 and 1+3 dimensional effective quark models"*
2014, Talk	DPG-Frühjahrstagung, Frankfurt am Main *"Inhomogeneous phases in effective models"*
2014, Talk	Hadrons from Quarks and Gluons, Hirschegg *"Inhomogeneous phases in effective models"*
2012, Talk	ConfinementX, Munich *"Inhomogeneous condensates in the parity doublet model"*
2012, Talk	ExtreMe Matter Institute Emmi: Quark-Gluon Plasma meets cold Atoms - Episode III, Hirschegg *"Inhomogeneous condensates in the parity doublet model"*
2012, Talk	APCTP-WCU Focus program: "From dense matter to compact stars in QCD and in hQCD", Pohang *"Restoration of chiral symmetry in the large-Nc limit"*

2011, Poster	Quark Matter, Annecy *"Large-N_c behavior of hadronic models at nonzero temperature"*
2011, Talk	Excited QCD, Les Houches *"Large N_c behavior of hadronic models at nonzero T"*
2010, Talk	Excited QCD,Tatranska Lomnica *"Role of the tetraquark in the chiral phase transition"*
2009, Talk	DPG-Frühjahrstagung, Bochum *"Role of the tetraquark in the chiral phase transition"*

Schools and further education

Schools on special topics:

2012	H-QM Lecture Week, *"Heavy Ion Collisions: The Big Picture II"*
2012	Helmholz-Rosatom School for young scientists at FAIR 2012
2011	H-QM Lecture Week, *"Hard Probes in Heavy Ion Collisions"*
2010	HGS-HIRe Power Week, *"Special Aspects of Quantum Field Theory"*
2010	H-QM Lecture Week, *"Heavy Probes in Heavy Ion Collisions"*
2010	H-QM Lecture Week, *"Heavy Ion Collisions: The Big Picture"*

Helmholtz Softskill courses in cooperation with Imperial College in London:

2012	Career Development and Leadership
2010	Presentation Skills and Scientific Writing
2009	Research Skills Development

Bibliography

[1] N. Cabibbo and G. Parisi, Phys. Lett. B **59**, 67 (1975).

[2] M. Cheng, N. H. Christ, S. Datta, J. van der Heide, C. Jung, F. Karsch, O. Kaczmarek and E. Laermann *et al.*, Phys. Rev. D **74**, 054507 (2006) [hep-lat/0608013].

[3] Y. Aoki, Z. Fodor, S. D. Katz and K. K. Szabo, Phys. Lett. B **643**, 46 (2006) [hep-lat/0609068].

[4] D. H. Rischke, Prog. Part. Nucl. Phys. **52**, 197 (2004) [nucl-th/0305030].

[5] S. B. Ruester, V. Werth, M. Buballa, I. A. Shovkovy and D. H. Rischke, Phys. Rev. D **72**, 034004 (2005) [hep-ph/0503184].

[6] K. Rajagopal and F. Wilczek, In *Shifman, M. (ed.): At the frontier of particle physics, vol. 3* 2061-2151 [hep-ph/0011333].

[7] U. G. Meissner, Phys. Rept. **161**, 213 (1988).

[8] S. Gasiorowicz and D. A. Geffen, Rev. Mod. Phys. **41**, 531 (1969).

[9] B. W. Lee, Phys. Rev. Lett. **20**, 617 (1968).

[10] J. Beringer *et al.* [Particle Data Group Collaboration], Phys. Rev. D **86**, 010001 (2012).

[11] A. Casher, Phys. Lett. B **83**, 395 (1979).

[12] K. G. Wilson, Phys. Rev. D **10**, 2445 (1974).

[13] A. M. Polyakov, Phys. Lett. B **72**, 477 (1978).

[14] F. R. Brown, F. P. Butler, H. Chen, N. H. Christ, Z. h. Dong, W. Schaffer, L. I. Unger and A. Vaccarino, Phys. Rev. Lett. **65**, 2491 (1990).

[15] C. DeTar and U. M. Heller, Eur. Phys. J. A **41**, 405 (2009) [arXiv:0905.2949 [hep-lat]].

[16] K. Fukushima, Phys. Lett. B **591**, 277 (2004) [hep-ph/0310121].

[17] B. -J. Schaefer, J. M. Pawlowski and J. Wambach, Phys. Rev. D **76**, 074023 (2007) [arXiv:0704.3234 [hep-ph]].

[18] S. Hands, Nucl. Phys. Proc. Suppl. **106**, 142 (2002) [hep-lat/0109034].

[19] P. de Forcrand and O. Philipsen, JHEP **0701**, 077 (2007) [hep-lat/0607017].

[20] Y. Nambu and G. Jona-Lasinio, Phys. Rev. **122**, 345 (1961).

[21] Y. Nambu and G. Jona-Lasinio, Phys. Rev. **124**, 246 (1961).

[22] S. P. Klevansky, Rev. Mod. Phys. **64**, 649 (1992).

[23] U. Vogl and W. Weise, Prog. Part. Nucl. Phys. **27**, 195 (1991).

[24] T. Hatsuda and T. Kunihiro, Phys. Rept. **247**, 221 (1994) [hep-ph/9401310].

[25] M. Buballa, Phys. Rept. **407**, 205 (2005) [hep-ph/0402234].

[26] M. Gell-Mann and MLevy, Nuovo Cim. **16**, 705 (1960).

[27] P. Ko and S. Rudaz, Phys. Rev. D **50**, 6877 (1994).

[28] M. Urban, M. Buballa and J. Wambach, Nucl. Phys. A **697**, 338 (2002) [hep-ph/0102260].

[29] D. Parganlija, F. Giacosa and D. H. Rischke, Phys. Rev. D **82**, 054024 (2010) [arXiv:1003.4934 [hep-ph]].

[30] D. Parganlija, P. Kovacs, G. Wolf, F. Giacosa and D. H. Rischke, Phys. Rev. D **87**, 014011 (2013) [arXiv:1208.0585 [hep-ph]].

[31] N. K. Glendenning, New York, USA: Springer 2nd ed. (2000) 492 p

[32] I. Mishustin, J. Bondorf and M. Rho, Nucl. Phys. A **555**, 215 (1993).

[33] P. Papazoglou, S. Schramm, J. Schaffner-Bielich, H. Stoecker and W. Greiner, Phys. Rev. C **57**, 2576 (1998) [nucl-th/9706024].

[34] P. Papazoglou, D. Zschiesche, S. Schramm, J. Schaffner-Bielich, H. Stoecker and W. Greiner, Phys. Rev. C **59**, 411 (1999) [nucl-th/9806087].

[35] L. Bonanno, A. Drago and A. Lavagno, Phys. Rev. Lett. **99**, 242301 (2007) [arXiv:0704.3707 [hep-ph]].

[36] D. J. Gross and A. Neveu, Phys. Rev. D **10**, 3235 (1974).

[37] U. Wolff, Phys. Lett. B **157**, 303 (1985).

[38] M. Thies and K. Urlichs, Phys. Rev. D **67**, 125015 (2003) [hep-th/0302092].

[39] G. Basar, G. V. Dunne and M. Thies, Phys. Rev. D **79**, 105012 (2009) [arXiv:0903.1868 [hep-th]].

[40] L. L. Salcedo, S. Levit and J. W. Negele, Nucl. Phys. B **361**, 585 (1991).

[41] R. F. Dashen, B. Hasslacher and A. Neveu, Phys. Rev. D **12**, 2443 (1975).

[42] D. Ebert and K. G. Klimenko, arXiv:0902.1861 [hep-ph].

[43] L. McLerran and R. D. Pisarski, Nucl. Phys. A **796**, 83 (2007) [arXiv:0706.2191 [hep-ph]].

[44] L. McLerran, K. Redlich and C. Sasaki, Nucl. Phys. A **824**, 86 (2009) [arXiv:0812.3585 [hep-ph]].

[45] T. Kojo, Y. Hidaka, L. McLerran and R. D. Pisarski, Nucl. Phys. A **843**, 37 (2010) [arXiv:0912.3800 [hep-ph]].

[46] G. 't Hooft, Nucl. Phys. B **72**, 461 (1974).

[47] E. Witten, Nucl. Phys. B **160**, 57 (1979).

[48] R. F. Lebed, Czech. J. Phys. **49**, 1273 (1999) [nucl-th/9810080].

[49] S. R. Coleman and E. Witten, Phys. Rev. Lett. **45**, 100 (1980).

[50] E. Witten, Annals Phys. **128**, 363 (1980).

[51] C. B. Thorn, Phys. Lett. B **99**, 458 (1981).

[52] B. Bringoltz and M. Teper, Phys. Lett. B **628**, 113 (2005) [hep-lat/0506034].

[53] M. Panero, Phys. Rev. Lett. **103**, 232001 (2009) [arXiv:0907.3719 [hep-lat]].

[54] G. Baym, Phys. Rev. Lett. **30**, 1340 (1973).

[55] R. F. Sawyer and D. J. Scalapino, Phys. Rev. D **7**, 953 (1973).

[56] D. K. Campbell, R. F. Dashen and J. T. Manassah, Phys. Rev. D **12**, 979 (1975).

[57] D. K. Campbell, R. F. Dashen and J. T. Manassah, Phys. Rev. D **12**, 1010 (1975).

[58] R. F. Dashen and J. T. Manassah, Phys. Lett. B **50**, 460 (1974).

[59] G. Baym, D. Campbell, R. F. Dashen and J. Manassah, Phys. Lett. B **58**, 304 (1975).

[60] A. B. Migdal, Rev. Mod. Phys. **50**, 107 (1978).

[61] G. Baym, Nucl. Phys. A **352**, 355 (1981).

[62] W. H. Dickhoff, A. Faessler, H. Muther and J. Meyer-Ter-Vehn, Nucl. Phys. A **368** (1981) 445.

[63] K. Kolehmainen and G. Baym, Nucl. Phys. A **382**, 528 (1982).

[64] G. Baym, B. L. Friman and G. Grinstein, Nucl. Phys. B **210**, 193 (1982).

[65] A. Akmal and V. R. Pandharipande, Phys. Rev. C **56**, 2261 (1997) [nucl-th/9705013].

[66] M. Wagner, Phys. Rev. D **76**, 076002 (2007) [arXiv:0704.3023 [hep-lat]].

[67] D. Ebert, T. G. Khunjua, K. G. Klimenko and V. C. .Zhukovsky, arXiv:1405.3789 [hep-th].

[68] T. Kojo, arXiv:1406.4630 [hep-ph].

[69] T. Kojo, Y. Hidaka, K. Fukushima, L. D. McLerran and R. D. Pisarski, Nucl. Phys. A **875**, 94 (2012) [arXiv:1107.2124 [hep-ph]].

[70] W. Broniowski and M. Kutschera, Phys. Lett. B **234**, 449 (1990).

[71] M. Sadzikowski and W. Broniowski, Phys. Lett. B **488**, 63 (2000) [hep-ph/0003282].

[72] R. Casalbuoni, R. Gatto, N. Ippolito, G. Nardulli and M. Ruggieri, Phys. Lett. B **627**, 89 (2005) [Erratum-ibid. B **634**, 565 (2006)] [hep-ph/0507247].

[73] D. Nickel, Phys. Rev. D **80**, 074025 (2009) [arXiv:0906.5295 [hep-ph]].

[74] T. L. Partyka, Mod. Phys. Lett. A **26**, 543 (2011) [arXiv:1005.2667 [hep-ph]].

[75] W. Broniowski, Acta Phys. Polon. Supp. **5**, 631 (2012) [arXiv:1110.4063 [nucl-th]].

[76] S. Carignano and M. Buballa, Phys. Rev. D **86**, 074018 (2012) [arXiv:1203.5343 [hep-ph]].

[77] Y. -L. Ma, M. Harada, H. K. Lee, Y. Oh and M. Rho, Int. J. Mod. Phys. Conf. Ser. **29**, 1460238 (2014) [arXiv:1312.2290 [hep-ph]].

[78] M. Buballa and S. Carignano, arXiv:1406.1367 [hep-ph].

[79] S. Janowski, D. Parganlija, F. Giacosa and D. H. Rischke, Phys. Rev. D **84**, 054007 (2011) [arXiv:1103.3238 [hep-ph]].

[80] S. Gallas, F. Giacosa and D. H. Rischke, Phys. Rev. D **82**, 014004 (2010) [arXiv:0907.5084 [hep-ph]].

[81] W. I. Eshraim, S. Janowski, F. Giacosa and D. H. Rischke, Phys. Rev. D **87**, no. 5, 054036 (2013) [arXiv:1208.6474 [hep-ph]].

[82] S. Gallas and F. Giacosa, Int. J. Mod. Phys. A **29**, no. 17, 1450098 (2014) [arXiv:1308.4817 [hep-ph]].

[83] C. E. Detar and T. Kunihiro, Phys. Rev. D **39**, 2805 (1989).

[84] D. Jido, Y. Nemoto, M. Oka and A. Hosaka, Nucl. Phys. A **671**, 471 (2000) [hep-ph/9805306].

[85] D. Jido, M. Oka and A. Hosaka, Prog. Theor. Phys. **106**, 873 (2001) [hep-ph/0110005].

[86] D. Zschiesche, L. Tolos, J. Schaffner-Bielich and R. D. Pisarski, Phys. Rev. C **75**, 055202 (2007) [nucl-th/0608044].

[87] C. Sasaki and I. Mishustin, Phys. Rev. C **82**, 035204 (2010) [arXiv:1005.4811 [hep-ph]].

[88] C. Sasaki, H. K. Lee, W. -G. Paeng and M. Rho, Phys. Rev. D **84**, 034011 (2011) [arXiv:1103.0184 [hep-ph]].

[89] W. -G. Paeng, H. K. Lee, M. Rho and C. Sasaki, Phys. Rev. D **85**, 054022 (2012) [arXiv:1109.5431 [hep-ph]].

[90] W. -G. Paeng, H. K. Lee, M. Rho and C. Sasaki, Phys. Rev. D **88**, no. 10, 105019 (2013) [arXiv:1303.2898 [nucl-th]].

[91] S. Gallas, F. Giacosa and G. Pagliara, Nucl. Phys. A **872**, 13 (2011) [arXiv:1105.5003 [hep-ph]].

[92] C. Amsler and F. E. Close, Phys. Lett. B **353**, 385 (1995) [hep-ph/9505219].

[93] W. -J. Lee and D. Weingarten, Phys. Rev. D **61**, 014015 (2000) [hep-lat/9910008].

[94] F. E. Close and A. Kirk, Eur. Phys. J. C **21**, 531 (2001) [hep-ph/0103173].

[95] F. E. Close and N. A. Tornqvist, J. Phys. G **28**, R249 (2002) [hep-ph/0204205].

[96] C. Amsler and N. A. Tornqvist, Phys. Rept. **389**, 61 (2004).

[97] F. Giacosa, T. .Gutsche, V. E. Lyubovitskij and A. Faessler, Phys. Rev. D **72**, 094006 (2005) [hep-ph/0509247].

[98] F. Giacosa, T. .Gutsche, V. E. Lyubovitskij and A. Faessler, Phys. Lett. B **622**, 277 (2005) [hep-ph/0504033].

[99] E. van Beveren, T. A. Rijken, K. Metzger, C. Dullemond, G. Rupp and J. E. Ribeiro, Z. Phys. C **30**, 615 (1986) [arXiv:0710.4067 [hep-ph]].

[100] N. A. Tornqvist, Z. Phys. C **68**, 647 (1995) [hep-ph/9504372].

[101] J. A. Oller and E. Oset, Nucl. Phys. A **620**, 438 (1997) [Erratum-ibid. A **652**, 407 (1999)] [hep-ph/9702314].

[102] J. R. Pelaez, Phys. Rev. Lett. **92**, 102001 (2004) [hep-ph/0309292].

[103] J. R. Pelaez, Mod. Phys. Lett. A **19**, 2879 (2004) [hep-ph/0411107].

[104] E. van Beveren, D. V. Bugg, F. Kleefeld and G. Rupp, Phys. Lett. B **641**, 265 (2006) [hep-ph/0606022].

[105] F. Giacosa, Phys. Rev. D **75**, 054007 (2007) [hep-ph/0611388].

[106] F. Giacosa, Phys. Rev. D **74**, 014028 (2006) [hep-ph/0605191].

[107] R. L. Jaffe, Phys. Rev. D **15**, 267 (1977).

[108] R. L. Jaffe, Phys. Rev. D **15**, 281 (1977).

[109] A. H. Fariborz, R. Jora and J. Schechter, Phys. Rev. D **72**, 034001 (2005) [hep-ph/0506170].

[110] A. H. Fariborz, Int. J. Mod. Phys. A **19**, 2095 (2004) [hep-ph/0302133].

[111] M. Napsuciale and S. Rodriguez, Phys. Rev. D **70**, 094043 (2004) [hep-ph/0407037].

[112] L. Maiani, F. Piccinini, A. D. Polosa and V. Riquer, Phys. Rev. Lett. **93**, 212002 (2004) [hep-ph/0407017].

[113] W. Heupel, G. Eichmann and C. S. Fischer, Phys. Lett. B **718**, 545 (2012) [arXiv:1206.5129 [hep-ph]].

[114] A. Heinz, S. Struber, F. Giacosa and D. H. Rischke, Phys. Rev. D **79**, 037502 (2009) [arXiv:0805.1134 [hep-ph]].

[115] R. Machleidt, Phys. Rev. C **63**, 024001 (2001) [nucl-th/0006014].

[116] H. Abuki, D. Ishibashi and K. Suzuki, approach," Phys. Rev. D **85**, 074002 (2012) [arXiv:1109.1615 [hep-ph]].

[117] S. Carignano and M. Buballa, Acta Phys. Polon. Supp. **5**, 641 (2012) [arXiv:1111.4400 [hep-ph]].

[118] S. Carignano, M. Buballa and B. -J. Schaefer, arXiv:1404.0057 [hep-ph].

[119] A. Heinz, Acta Phys. Polon. Supp. **4**, 561 (2011) [arXiv:1107.4001 [hep-ph]].

[120] A. Heinz, F. Giacosa and D. H. Rischke, Phys. Rev. D **85**, 056005 (2012) [arXiv:1110.1528 [hep-ph]].

[121] M. Gell-Mann, R. J. Oakes and B. Renner, Phys. Rev. **175**, 2195 (1968).

[122] M. L. Goldberger and S. B. Treiman, Phys. Rev. **110**, 1178 (1958).

[123] J. I. Kapusta, Cambridge University Press 2nd ed. (2006) 442 p

[124] M. L. Bellac, Cambridge University Press (2000) 272 p

[125] A. M. Tsvelik, Cambridge University Press 2nd ed. (2007) 380 p

[126] C. Itzykson and J.-B. Zuber, Dover Publications (2006) 752 p

[127] J. M. Cornwall, R. Jackiw and E. Tomboulis, Phys. Rev. D **10**, 2428 (1974).

[128] A. Bochkarev and J. I. Kapusta, Phys. Rev. D **54**, 4066 (1996) [hep-ph/9602405].

[129] J. T. Lenaghan and D. H. Rischke, J. Phys. G **26**, 431 (2000) [nucl-th/9901049].

[130] N. Petropoulos, hep-ph/0402136.

[131] E. Megias, E. Ruiz Arriola and L. L. Salcedo, Phys. Rev. D **74**, 065005 (2006) [hep-ph/0412308].

[132] J. Gasser and H. Leutwyler, Phys. Lett. B **184**, 83 (1987).

[133] S. Leupold and U. Mosel, AIP Conf. Proc. **1322**, 64 (2010).

[134] K. Fukushima and T. Hatsuda, Rept. Prog. Phys. **74**, 014001 (2011) [arXiv:1005.4814 [hep-ph]].

[135] A. Dumitru and R. D. Pisarski, Phys. Lett. B **504**, 282 (2001) [hep-ph/0010083].

[136] A. Mocsy, F. Sannino and K. Tuominen, Phys. Rev. Lett. **92**, 182302 (2004) [hep-ph/0308135].

[137] P. N. Meisinger and M. C. Ogilvie, Phys. Lett. B **379**, 163 (1996) [hep-lat/9512011].

[138] A. Heinz, PoS ConfinementX , 250 (2012) [arXiv:1301.3430].

[139] A. Heinz, F. Giacosa and D. H. Rischke, arXiv:1312.3244 [nucl-th].

[140] J. D. Walecka, Annals Phys. **83**, 491 (1974).

[141] B. D. Serot and J. D. Walecka, Int. J. Mod. Phys. E **6**, 515 (1997) [nucl-th/9701058].

[142] D. Ebert, N. V. Gubina, K. G. Klimenko, S. G. Kurbanov and V. C. .Zhukovsky, Phys. Rev. D **84**, 025004 (2011) [arXiv:1102.4079 [hep-ph]].

[143] D. H. Youngblood, H. L. Clark and Y. -W. Lui, Phys. Rev. Lett. **82**, 691 (1999).

[144] D. H. Youngblood, Y. W. Lui, H. L. Clark, B. John, Y. Tokimoto and X. Chen, Phys. Rev. C **69**, 034315 (2004).

[145] C. .Hartnack, J. Aichelin and H. Oeschler, Int. J. Mod. Phys. D **16**, 153 (2007).

[146] O. Schnetz, M. Thies and K. Urlichs, Annals Phys. **321**, 2604 (2006) [hep-th/0511206].

[147] N. D. Mermin and H. Wagner, Heisenberg models," Phys. Rev. Lett. **17**, 1133 (1966).

[148] V. Schon and M. Thies, Phys. Rev. D **62**, 096002 (2000) [hep-th/0003195].

[149] V. Schon and M. Thies, In *Shifman, M. (ed.): At the frontier of particle physics, vol. 3* 1945-2032 [hep-th/0008175].

[150] R. H. P. Kleiss and T. W. Janssen, arXiv:1405.1536 [hep-ph].

[151] D. Jido, T. Hatsuda and T. Kunihiro, Phys. Rev. Lett. **84**, 3252 (2000) [hep-ph/9910375].

[152] A. J. Mizher, M. N. Chernodub and E. S. Fraga, chiral transitions," Phys. Rev. D **82**, 105016 (2010) [arXiv:1004.2712 [hep-ph]].

[153] D. P. Menezes, M. Benghi Pinto, S. S. Avancini, A. Perez Martinez and C. Providencia, Phys. Rev. C **79**, 035807 (2009) [arXiv:0811.3361 [nucl-th]].

[154] G. N. Ferrari, A. F. Garcia and M. B. Pinto, Phys. Rev. D **86**, 096005 (2012) [arXiv:1207.3714 [hep-ph]].